CHARACTERIZING MIDDLE EAR REFLECTANCE VIA POLE-ZERO FITTING

BY

SARAH R. ROBINSON

THESIS

Submitted in partial fulfillment of the requirements
for the degree of Master of Science in Electrical and Computer Engineering
in the Graduate College of the
University of Illinois at Urbana-Champaign, 2013

Urbana, Illinois

Adviser:

Associate Professor Jont B. Allen

ABSTRACT

This thesis characterizes middle ear complex acoustic reflectance (CAR) and impedance by fitting poles and zeros to real-ear measurements. The goal of this work is to establish a quantitative connection between pole-zero locations and the underlying physical properties of CAR data. Most previous studies have analyzed CAR magnitude; while the magnitude accounts for reflected power, it does not encode latency information. Thus, an analysis that studies the real and imaginary parts of the data together could be more powerful. This is accomplished by fitting poles and zeros to the complex data. CAR data compiled from various studies are examined using this method, including data from Voss and Allen [1994], Rosowski et al. [2012], Nakajima et al. [2012] and a new study of bacterial biofilm [Nguyen et al., 2013]. Recent measurements were taken using a middle ear acoustic power analyzer (MEPA) system (HearID, Mimosa Acoustics), which makes complex acoustic impedance and reflectance measurements in the ear canal over the 0.2 to 6.0 kHz frequency range. Pole-zero fits to measurements over this range are achieved with an average RMS relative error of less than 3% using 12 poles. Factoring the reflectance fit into its all-pass and minimum-phase components approximates the effect of the ear canal, allowing for comparison across measurements. It was found that individual CAR magnitude variations for normal middle ears in the 1 to 4 kHz range can be characterized by closely-placed pole-zero pairs in that frequency region. Additionally, the characteristics of the pole-zero fit, such as the locations of the poles and zeros in the s-plane, differ between normal and pathological middle ears. This thesis establishes a methodology for examining the physical and mathematical properties of CAR using a parametric model. Pole-zero modeling shows promise for concise parameterization of CAR data and for identification of middle ear pathologies. Results of a novel study of CAR in the presence of bacterial biofilm are also presented.

To my parents, John and Jennifer, and to my brother, Josh, for their love and support.

ACKNOWLEDGMENTS

Many thanks to the Human Speech Recognition group at UIUC, and Dr. Cac Nguyen, who conducted the bacterial biofilm study. This material is based upon work supported by the National Science Foundation under Grant No. 0903622, and an STTR award from Office of Naval Research under the contract number N00014-11-C-0498. The biofilm study was supported by a Bioengineering Research Partnership grant from the National Institutes of Health (NIBIB R01 EB013723, PI: Stephen A. Boppart). Much of this material has been published in Robinson et al. [2013] (particularly Chapter 3, Chapter 4, Chapter 7, and Appendix A), and in Nguyen et al. [2013] (particularly Chapter 6).

TABLE OF CONTENTS

LIST OF ABBREVIATIONS

CAR	Complex Acoustic Reflectance
DP	Distortion Product
LHP	Left Half Plane
$MEPA$	Middle Ear Power Assessment
MSE	Mean Squared Error
OAE	Otoacoustic Emission
OM	Otitis Media
RHP	Right Half Plane
RMS	Root Mean Squared
$SSCD$	Superior Semicircular Canal Dehiscence
$SNHL$	Sensorineural Hearing Loss
TM	Tympanic Membrane

CHAPTER 1

INTRODUCTION

The middle ear is a critical part of the auditory pathway. Pressure waves along the ear canal, which acts as an acoustic waveguide, are incident on the *tympanic membrane* (TM) and cause it to vibrate. This vibration drives the ossicular chain (malleus, incus, and stapes) via the connection of the malleus to the TM at the umbo (Figure 1.1). The ossicles function as a mechanical lever system, delivering an amplified pressure wave to the cochlea via the stapes footplate at the oval window. For low frequencies (up to 2-4 [kHz]) the footplate of the stapes moves approximately like a piston [Voss et al., 2000], creating pressure waves in the cochlear fluid. This whole process may be modeled as a series of transmission lines. For the purposes of this document, the middle ear may be defined as beginning at the TM and ending at the oval window of the cochlea.

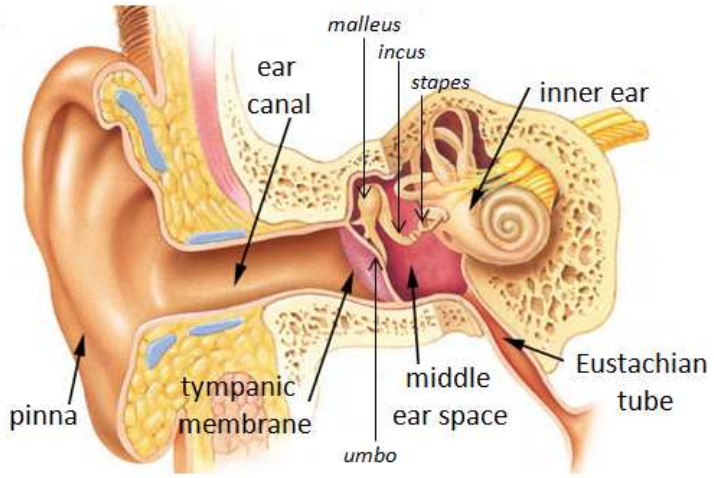

Figure 1.1: The human ear (including outer, middle, and inner ear), which may be modeled as a series of transmission lines.

Various malfunctions of the middle ear system can result in conductive hearing loss, such that the middle ear transfer function is abnormal. Some conditions associated with conductive hearing loss include *otitis media* (OM)

with effusion (fluid in the middle ear space), TM perforation (a hole in the eardrum), otosclerosis (abnormal bone growth in the middle ear), and ossicular discontinuity (separation of the ossicular joints). Otosclerosis and ossicular discontinuity most commonly occur at the stapes and incudo-stapedial joint, respectively. Some other pathologies include *superior semicircular canal dehiscence* (SSCD; thinning or absence of part of the temporal bone) and pressurization of the middle ear (e.g. positive or negative pressure in the middle ear space, frequently due to eustachian tube disfunction).

Middle ear pathologies can affect all age groups and have a variety of causes. For instance, noise trauma can cause both TM perforation and ossicular discontinuity. Middle ear fluid or OM is especially common in young children and infants due to Eustachian tube disfunction and, in the case of newborns, fluids associated with birth (i.e. amniotic fluid). Chronic OM causes conductive hearing loss and may result in speech perception difficulties. Patients with chronic OM may have 27 [dB] on average and up to 60 [dB] loss in hearing, depending on the effusion fluid level [Bluestone and Klein, 2007]. Not only can OM interfere with sound conduction, it can also lead to complications such as eardrum bursts (TM perforation) and serious bacterial infection. Biofilm, a bacterial plaque buildup on the TM, is one such complication. Biofilm interferes with the motion of the TM, causing a conductive hearing loss, and is resistant to antibiotic treatments [Nguyen et al., 2010].

Most audiometric measurements cannot bypass the middle ear, thus a correct diagnosis of middle ear function is crucial to a correct diagnosis of hearing loss. One important example of this arises in newborn hearing screening, which is intended to detect *sensorineural hearing loss* (SNHL) as early as possible in order to identify candidates for cochlear implants, because implant efficacy diminishes rapidly with age. As infants are unable to cooperate with traditional perceptual threshold testing, an objective measure of hearing function is required. Typically an acoustic measurement, the *distortion product* (DP), is taken, which detects evoked *otoacoustic emissions* (OAEs) from the cochlea. The absence of OAEs is indicative of SNHL. However, there is an extremely high DP fail rate in newborns without SNHL, due to middle ear fluid blocking sound transmission to and from the cochlea. Hunter et al. [2010] found that the DP pass rate increases drastically in the hours following birth, from about 50% within the first 20 hours to about 85% by 36

hours as transient cases of middle ear fluid are resolved. Thus, identification of transient fluid cases limits the need for more extensive audiometric tests, and frees necessary clinical resources for infants with SNHL, chronic OM, or both. To improve the infant hearing screening process, a way to reliably monitor middle ear status is necessary.

Traditional clinical diagnosis of conductive hearing loss relies on air/bone threshold measurements, tympanometry, and investigative surgery. Conductive hearing loss is defined by an 'air-bone gap,' which is a difference in the audiometric thresholds for sound conducted in air and sound conducted in bone (via a 'bone driver' oscillator placed on the mastoid bone). Tympanometry measures the compliance of the TM as the ear canal pressure is varied between the probe and the eardrum. Tympanometry is very unreliable in newborns because the ear canal wall is very compliant. For older children and adults, tympanometry can detect some middle ear conditions, but cannot always differentiate between them [Nakajima et al., 2012]. This can lead to surgical exploration of the middle ear which is expensive, and is unnecessary for some patients. For instance, SSCD, which presents similar audiometric results to other forms of conductive hearing loss, cannot be remedied by middle ear surgery. It is important to develop a standardized measurement that can reliably detect and distinguish many middle ear pathologies better than the existing clinical standards.

Wideband *complex acoustic reflectance* (CAR) demonstrates diagnostic promise for differentiating between various types of conductive hearing loss. Acoustic reflectance measurements and their clinical applications have been the subject of many recent studies. These studies have shown that power reflectance, the magnitude squared of the CAR, shows distinct and often systematic variations between pathological and normal middle ears (e.g. Keefe and Simmons, 2003, Feeney et al., 2003, Allen et al., 2005, Hunter et al., 2010). Studies by Voss et al. [2012] and Nakajima et al. [2012] have investigated the efficacy of reflectance measurements for differential diagnosis of middle ear pathology. Tympanometry and laser doppler vibrometry are the current standards for presurgical differentiation between ossicular fixation, ossicular discontinuity, and third window disorders [Rosowski et al., 2003, 2008]; Nakajima et al. concluded that power reflectance performs as well as laser doppler vibrometry, both in combination with audiometry (e.g. air-bone gap measurements), for differential diagnosis of these disorders. This

is a valuable result, because CAR measurements can be performed using the United States Food and Drug Adminstration (FDA) 510(K) cleared middle ear acoustic power assessment (MEPA) HearID system (Mimsosa Acoustics), which, as stated by Nakajima et al. [2012], costs an order of magnitude less than the laser Doppler vibrometer ($\approx 10,000$ vs. $100,000$ USD) and requires less training to operate. In another recent study, Voss et al. [2012] systematically manipulated cadaver ears to isolate the effects of various pathologies with differing degrees of severity, and examined the CAR responses. They also concluded that power reflectance may be a strong supplement to audiometry for the diagnosis of certain pathologies.

While uncertainty in the residual ear canal volume significantly confounds phase information associated with the eardrum and ossicles, taking the magnitude of the CAR eliminates relevant latency information entirely. It follows that a holistic analysis of the complex data could be more powerful and generalizable if the canal effect were accounted for in a rigorous manner, without eliminating all phase data. In this thesis, a method for concise parametric characterization of CAR measurements is developed, with the ultimate goal of improving differential diagnosis of middle ear pathology. This is accomplished by fitting poles and zeros to the complex data. It is important to note that this work is primarily intended to aid in middle ear modeling efforts and automated diagnosis of pathologies; a raw pole-zero diagnosis is not intended for the clinic.

CHAPTER 2

ACOUSTIC REFLECTANCE

For assessment of the middle ear, CAR and impedance are measured at ambient pressure by a probe containing a microphone and loudspeaker, sealed in the ear canal via a foam tip. These measurements are wideband, and are limited by the characteristics of the microphone used in the probe. The MEPA system (Mimosa Acoustics), for instance, measures CAR at 248 frequencies from 0.2 to 6 [kHz]. In the following sections, the calibration of such systems and the effect of the ear canal on CAR and impedance measurements are described. Finally, known reflectance properties of normal middle-ears are presented, and the effects of middle ear pathologies on the CAR and impedance are discussed.

2.1 Measuring Acoustic Reflectance

Clinical systems to measure the acoustic impedance of the ear canal have been in development since the 1980s, enabled by a simple, robust acoustic source calibration process [Allen, 1986]. The calibration is performed by measuring the impedances of known cylindrical cavities to find the frequency dependent Thévenin equivalent parameters $P_s(\omega)$ and $Z_s(\omega)$ of the sound source, which is housed in a foam or rubber tip (and accompanied by at least one microphone); a diagram of the Thévenin equivalent circuit is shown in Fig. 2.1. The number of cavities used in calibration varies for different measurement systems, but is typically around four. The measured pressure responses and the theoretical impedances of the known cavities, considering thermal and viscous losses [Keefe, 1984], are used to determine the source

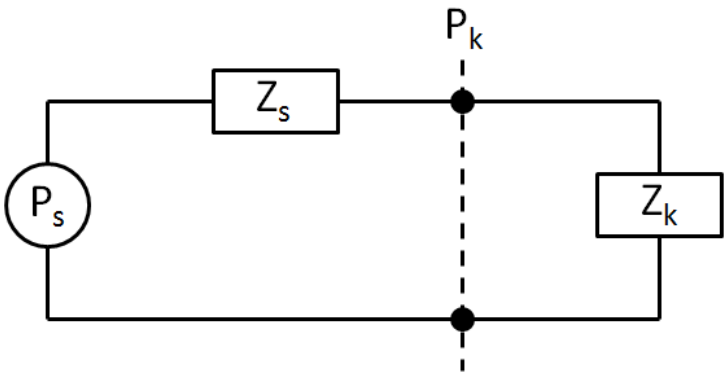

Figure 2.1: Thévenin equivalent circuit for calibration of the reflectance measurement probe. P_s and Z_s are the source pressure and impedance, while P_k and Z_k are the measured pressure and theoretical impedances of the cylindrical calibration cavities. If there are four tubes, then k =1, 2, 3, 4. All of these quantities will vary with frequency ω.

pressure and impedance by solving the overdetermined system of equations

$$\begin{bmatrix} Z_1(\omega) & -P_1(\omega) \\ Z_2(\omega) & -P_2(\omega) \\ Z_3(\omega) & -P_3(\omega) \\ Z_4(\omega) & -P_4(\omega) \end{bmatrix} \begin{bmatrix} P_s(\omega) \\ Z_s(\omega) \end{bmatrix} = \begin{bmatrix} Z_1(\omega)P_1(\omega) \\ Z_2(\omega)P_2(\omega) \\ Z_3(\omega)P_3(\omega) \\ Z_4(\omega)P_4(\omega) \end{bmatrix}. \tag{2.1}$$

As this system is of the form $A\mathbf{x} = \mathbf{b}$, the solution is $\mathbf{x_{opt}} = (\mathbf{A^t A})^{-1}\mathbf{A^t b}$. Once the Thévenin parameters of the source, $Z_s(\omega)$ and $P_s(\omega)$, have been calculated over the desired set of frequencies, the impedance measured at the ear canal is simply

$$Z(\omega) = Z_s(\omega)\frac{P(\omega)}{P_s(\omega) - P(\omega)}, \tag{2.2}$$

where $P(\omega)$ is the measured pressure. This method proved to be much faster and simpler than the previously existing calibration methods, making it much more suitable for clinical use [Allen et al., 2005]. Such systems were first used for measurement of ear canal CAR in humans in the early 1990s [Keefe et al., 1992, Voss and Allen, 1994].

This calibration procedure assumes that the area of the calibration cavity and the area of the cavity to be measured (the ear canal) are the same. The probe tip is typically selected to fit the ear canal of the subject, considering for

example that an adult's ear canal will be larger than a child's ear canal. The probe is calibrated in a set of cavities similar to the ear canal size for which it will be used, such that the area of the calibration cavity is approximately equal to the area of the ear canal. Small variations in the actual area of the ear canal relative to the cavity area, within ±20%, cause a negligible change in the magnitude reflectance measurement [Keefe et al., 1992, Voss and Allen, 1994]. In their 1994 paper, Voss and Allen used calibration cavities of the average adult ear canal diameter, 7.4 [mm].

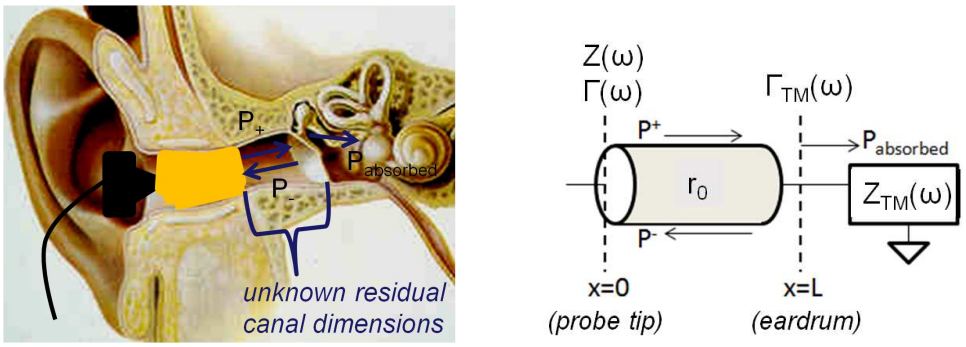

(a) (b)

Figure 2.2: Measuring CAR in the ear canal. (a) Probe placement in the ear canal, (b) a simple model of reflectance measurements in the ear canal.

After calibration, the probe is sealed in the ear canal as shown in Fig. 2.2a. Placement of the tip will vary across individuals, but on average it is about 5 to 10 [mm] from the TM since the probe is about 15 [mm] long and the typical adult ear canal is about 23.5 [mm] long [Fletcher, 1925]. It is worthwhile to note that for cadaver preparations, the tip of the probe is typically placed much closer to the TM, within 2-3 [mm]. Once the probe has been sealed (the foam tip has expanded) in the ear canal, a wideband stimulus is emitted by the probe, and the complex pressure response is measured. From the calibration pressure responses, the acoustic impedance, reflectance, and related quantities (admittance, power reflectance, etc.) may be calculated.

The CAR, denoted $\Gamma(\omega)$, is equal to the ratio of the reflected wave pressure, P^-, to the incident wave pressure, P^+, at the microphone location in the ear canal, as a function of radian frequency ($\omega = 2\pi f$). The magnitude squared of the reflectance, $|\Gamma(\omega)|^2$, represents the relative acoustic power reflected back to the ear canal from the middle and inner ears. The power reflectance is related to conductive hearing functionality and is therefore relevant to clinical

assessment of the middle ear [Allen et al., 2005]. The complex acoustic impedance $Z(\omega)$ and reflectance $\Gamma(\omega)$, as functions of frequency, are related by

$$\Gamma(\omega) = \frac{P^-(\omega)}{P^+(\omega)} = \frac{Z(\omega)/r_0 - 1}{Z(\omega)/r_0 + 1}, \tag{2.3}$$

where $r_0 = \rho c/A$ is the estimated *surge resistance*, ρ is the density of air, c is the speed of sound, and A is the area of the ear canal. The 'surge' impedance [Campbell, 1922] is defined as the amplitude of the $\delta(t)$ component of the time-domain impedance; because it is a real constant, it is denoted as the surge resistance. It follows that the reflectance is strictly causal [Claerbout, 1985]. The surge resistance and time domain reflectance are discussed further in Section 7.2.

It is important to note that for a passive system, such as the middle ear, the magnitude reflectance $|\Gamma(\omega)|$ will never be greater than 1. For a passive system, the real part of the impedance must always be non-negative [Brune, 1931, Van Valkenburg, 1964]. The corresponding constraint on the reflectance magnitude is proved as follows:

$$\begin{aligned}
0 \leq \mathrm{Re}\{Z(\omega)\} &= \frac{Z(\omega) + Z^*(\omega)}{2} \\
&\leq \frac{r_0}{2}\left[\frac{1+\Gamma(\omega)}{1-\Gamma(\omega)} + \frac{1+\Gamma^*(\omega)}{1-\Gamma^*(\omega)}\right] \\
&\leq \frac{r_0}{2}\left[\frac{(1+\Gamma(\omega))(1-\Gamma^*(\omega)) + (1+\Gamma^*(\omega))(1-\Gamma(\omega))}{(1-\Gamma(\omega))(1-\Gamma^*(\omega))}\right] \\
&\leq r_0\left[\frac{(1-|\Gamma(\omega)|^2)}{|1-\Gamma(\omega)|^2}\right].
\end{aligned}$$

For this inequality to hold, it is required that $|\Gamma(\omega)| \leq 1$. It follows that a purely imaginary impedance ($\mathrm{Re}\{Z(\omega)\} = 0$) must have a reflectance magnitude of 1.

2.2 Effects of the Residual Ear Canal

The clinical utility of CAR depends on its capacity to discern normal from pathological results, which requires a method for comparing measurements across ears. Direct comparison of CAR is complicated because the resid-

ual canal dimensions between the probe tip and TM vary across subjects. This uncertainty has a large effect on the reflectance phase and the complex acoustic impedance, making it difficult to compare measurements across ears. Consider now a simple measurement model, to aid intuition about the effects of the residual ear canal on the complex measurements.

In a simple model of CAR measurement, the ear canal may be modeled as a hard-walled tube terminated in a load $Z_{TM}(\omega)$ (the impedance of the middle ear including the TM) as shown in Fig. 2.2b. This model assumes plane wave propagation, which is valid up to about 27 [kHz] depending on the speed of sound and the exact area of the canal [Voss and Allen, 1994]. Above this frequency, higher order modes can become important. Note that the human hearing range is about 20 [Hz] to somewhat less than 20 [kHz]. The TM is approximated as perpendicular to the canal, even though it is actually at an angle (see Fig. 1.1). Nonplanar modes exist close to the TM due to its angle, but they are well attenuated within a few [mm] [Voss and Allen, 1994]. Thus, it is convenient that measurements are typically made at a canal location relatively far from the TM.

Take the distance along the ear canal between the probe tip and the TM to be L. Because L varies across subjects, it is important to consider how the measurements of $Z(\omega)$ and $\Gamma(\omega)$ are affected by the canal length, relative to their counterparts at the TM. The acoustic measurements of impedance $Z(0,\omega)$ and reflectance $\Gamma(0,\omega)$ are made at the probe. Acoustic impedance and reflectance at the probe are related to each other and to their counterparts measured at the TM, $Z_{TM}(\omega) = Z(L,\omega)$ and $\Gamma_{TM}(\omega) = \Gamma(L,\omega)$, by the acoustic transmission line relation

$$\begin{aligned} Z(x,\omega) = \frac{P(x,\omega)}{U(x,\omega)} &= \frac{P^+(x,\omega) + P^-(x,\omega)}{U^+(x,\omega) - U^-(x,\omega)} \\ &= \frac{P^+_{TM} e^{-jk(x-L)} + P^-_{TM} e^{jk(x-L)}}{U^+_{TM} e^{-jk(x-L)} - U^-_{TM} e^{jk(x-L)}}. \end{aligned} \tag{2.4}$$

An analogous equation for an electrical transmission line is derived by Staelin et al. [1998].

Pressure and velocity quantities marked with a '+' are forward-going, and those marked with a '-' are backward-going waves. U is the volume velocity, and $U(x,\omega)$ and $P(x,\omega)$ are frequency domain quantities. The wavenumber k, the characteristic impedance of the tube r_0, and the reflectance $\Gamma(x,\omega)$

are defined as follows:

$$k = \frac{\omega}{c} \tag{2.5}$$

$$r_0 = \frac{P^+(x,\omega)}{U^+(x,\omega)} = \frac{\rho c}{A} \tag{2.6}$$

$$\Gamma(x,\omega) = \frac{P^-(x,\omega)}{P^+(x,\omega)} = \frac{U^-(x,\omega)}{U^+(x,\omega)}. \tag{2.7}$$

Note that the relationship in Eq. 2.3 holds at any point along the ear canal in this model, because r_0 is constant when the tube has a uniform area $A(x)$.

In this model, the characteristic impedance of the ear canal tube and the surge resistance have the exact same value. A common failing of this simple model of reflectance is that is does not properly distinguish between a frequency dependent *reflection coefficient* and the *reflectance*. Because the tube is uniform and lossless, the surge impedance looking into the tube at any point along its length is equal to its characteristic impedance, r_0. However, for $\Gamma(\omega)$ to be a true reflectance, r_0 in Eq. 2.3 must always be the real-valued surge resistance (not the characteristic impedance of the ear canal, which may be complex). This is a necessary condition for $\gamma(t) = \mathcal{F}^{-1}\{\Gamma(\omega)\}$ to be strictly causal, meaning it has no $\delta(t)$ component. It is required that the time domain reflectance have no $\delta(t)$ singularity, because at $t = 0$ there can be no reflected wave [Claerbout, 1985].

Using the relations in Eqs. 2.4 through 2.7, it is possible to estimate the effect of probe insertion depth on the measurement of $Z(\omega)$ and $\Gamma(\omega)$. Starting from Eq. 2.4, the relationship between $Z(x,\omega)$ and $\Gamma(x,\omega)$ along the tube in Fig. 2.2b is further described by

$$\begin{aligned} Z(x,\omega) &= \frac{P^+(x,\omega)}{U^+(x,\omega)}\left[\frac{1+\frac{P^-(x,\omega)}{P^+(x,\omega)}}{1-\frac{U^-(x,\omega)}{U^+(x,\omega)}}\right] = \frac{P^+(x,\omega)}{U^+(x,\omega)}\left[\frac{1+\frac{P^-_{TM}}{P^+_{TM}}e^{2jk(x-L)}}{1-\frac{U^-_{TM}}{U^+_{TM}}e^{2jk(x-L)}}\right] \\ &= r_0\frac{1+\Gamma(x,\omega)}{1-\Gamma(x,\omega)} = r_0\frac{1+\Gamma_{TM}(\omega)e^{2jk(x-L)}}{1-\Gamma_{TM}(\omega)e^{2jk(x-L)}}. \end{aligned}$$

Examining this relationship at the probe tip ($x = 0$),

$$\begin{aligned} Z(0,\omega) &= r_0\left[\frac{1+\Gamma(0,\omega)}{1-\Gamma(0,\omega)}\right] = r_0\left[\frac{1+\Gamma_{TM}(\omega)e^{-2jkL}}{1-\Gamma_{TM}(\omega)e^{-2jkL}}\right] \\ &= r_0\left[\frac{1+\left[\frac{Z_{TM}(\omega)-r_0}{Z_{TM}(\omega)+r_0}\right]e^{-2jkL}}{1-\left[\frac{Z_{TM}(\omega)-r_0}{Z_{TM}(\omega)+r_0}\right]e^{-2jkL}}\right] \\ &= r_0\left[\frac{(Z_{TM}(\omega)+r_0)e^{jkL}+(Z_{TM}(\omega)-r_0)e^{-jkL}}{(Z_{TM}(\omega)+r_0)e^{jkL}-(Z_{TM}(\omega)-r_0)e^{-jkL}}\right] \\ &= r_0\left[\frac{Z_{TM}(\omega)\cos(kL)+jr_0\sin(kL)}{jZ_{TM}(\omega)\sin(kL)+r_0\cos(kL)}\right]. \end{aligned}$$

Thus, according to this model, the impedance and reflectance measured at the probe tip in the ear canal are related to the impedance and reflectance at the TM by

$$\Gamma(\omega) = \Gamma_{TM}(\omega)e^{-2jkL} \tag{2.8}$$

$$Z(\omega) = r_0\left[\frac{Z_{TM}(\omega)+jr_0 tan(kL)}{r_0+jZ_{TM}(\omega)tan(kL)}\right]. \tag{2.9}$$

It is easy to see that the variable canal length between subjects makes it difficult to compare impedance measurements. For the reflectance, however, it is propitious that $\Gamma(\omega)$ and $\Gamma_{TM}(\omega)$ only differ by a phase factor in this simple model, such that

$$|\Gamma(\omega)| = |\Gamma_{TM}(\omega)|. \tag{2.10}$$

It is clear that for this model of the ear canal, the magnitude of the reflectance is independent of the probe insertion depth. This makes it possible to compare the magnitude reflectance $|\Gamma|$ (and quantities derived from it) across subjects.

In many cases this simple tube model of the ear canal is not realistic, particularly because the residual ear canal area $A(x)$ varies with distance x along the ear canal [Farmer-Fedor and Rabbitt, 2002]. Equation 2.8 represents a special case of a uniform (constant $A(x)$), lossless canal; a nonuniform, lossless canal would have a more complicated phase dependence on frequency. However, consideration of the CAR magnitude (or the power re-

flectance $|\Gamma(\omega)|^2$) is highly effective because even when $A(x)$ is nonuniform, the ear canal may be reasonably approximated as lossless, and Eq. 2.10 holds. Eliminating the variation due to the residual ear canal by using the CAR magnitude or power reflectance allows for comparison across measurements with unknown residual canal dimensions. The relationship in Eq. 2.10 was experimentally verified by Voss et al. [2008], who showed that variations in measurement location along the canal result in minimal changes in the magnitude reflectance for an individual ear. Thus, the magnitude reflectance is the current diagnostic standard using CAR measurements. Often, the magnitude squared $|\Gamma|^2$ is considered, because it represents the fraction of acoustic power reflected by the middle ear.

2.3 Reflectance of the Human Middle Ear

Reflectance data were first reported for human ears by Stinson et al. [1982] and Hudde [1983]. Major early studies using the Thévenin calibration method include Keefe et al. [1993] and Voss and Allen [1994]. Many other normative and pathological studies have been conducted since then, as mentioned in Chapter 1. Perhaps the most controlled database of normative data was recently collected by Rosowski et al. [2012]. This data set is comprised of 58 'strictly normal' ears defined by stringent audiometric criteria, and will be used frequently throughout this thesis as a normative reference for examining changes of the CAR in the presence of middle ear pathologies.

2.3.1 Normal Ears

Figure 2.3 shows normative reflectance and impedance measurements measurements of normal ears from Rosowski et al. [2012]. The dotted black lines show the average normal ear from Rosowski et al. [2012], and the light gray regions show ± 1 standard deviation about the mean for these quantities. Six example normal ears from this study (S003L, S006L, S011L, S017L, S021L, and S022L) are shown as well. Considering Fig. 2.3a, the reflectance magnitude of normal ears approaches 1 at low frequencies, has a broad minimum in the mid-frequency region from about 1 to 4 [kHz], and increases again at high frequencies, possibly due to a high-frequency mass loading effect. The

mid-frequency region corresponds to the most sensitive hearing range for humans [Voss and Allen, 1994, Feeney et al., 2003, Allen et al., 2005], and is the region of most significant variation for normal ears [Rosowski et al., 2012]. Note that while the average ear may appear smooth in this region, there is actually a significant amount of individual variation across the six ears. The reflectance phase of the average ear and individual measurements (Fig. 2.3b) shows a significant amount of delay, due to the residual ear canal. This becomes especially apparent when considering the reflectance group delay, which has a large constant component across all frequencies.

The complex acoustic impedance is represented in two ways: the magnitude and phase (Figs. 2.3c and 2.3d), and the resistance and reactance (Figs. 2.3e and 2.3f), which are the real and imaginary parts of the impedance, respectively. The impedance has been normalized by the surge resistance r_0, to remove the effect of the ear canal area across subjects [Allen et al., 2005]. The residual ear canal causes a distinct 'standing wave' notch in the normalized impedance magnitude (Fig. 2.3c), due to reflections between the probe and TM [Scheperle et al., 2008, Withnell et al., 2009]. This notch is related to the mass-stiffness transition of the impedance across frequency for a given residual canal volume, corresponding to the transition from negative to positive impedance phase (Fig. 2.3d). A phase of $-\pi/2$ is a pure compliance ($Z_C = 1/j\omega C = e^{-j\pi/2}/\omega C$), while a phase of $\pi/2$ is related to a pure mass ($Z_M = j\omega M = e^{j\pi/2}\omega M$). Due to the relative magnitudes of the normalized resistance (Fig. 2.3e) and the normalized reactance (Fig. 2.3f), the normalized impedance magnitude is dominated by the reactance below 1 [kHz].

At low frequencies, it is clear that Z/r_0 is stiffness-dominated; because the normalized resistance is relatively small, the normalized reactance goes as $-\frac{1}{\omega}$, and the impedance phase approaches $-\pi/2$. The logarithmic plot of $|Z|$ has a distinct low frequency slope corresponding to the $-1/\omega$ behavior of the reactance. The compliance associated with this slope can be solved for assuming $Z/r_0 \approx 1/j\omega C$ at low frequencies, using a linear regression of the form

$$\log_{10}|Z(\omega)| = -A\log_{10}(\omega) + B, \tag{2.11}$$

where A should be approximately equal to -1 if the impedance is stiffness dominated, and $C \approx 10^{-B}$. The compliance C corresponds to an enclosed

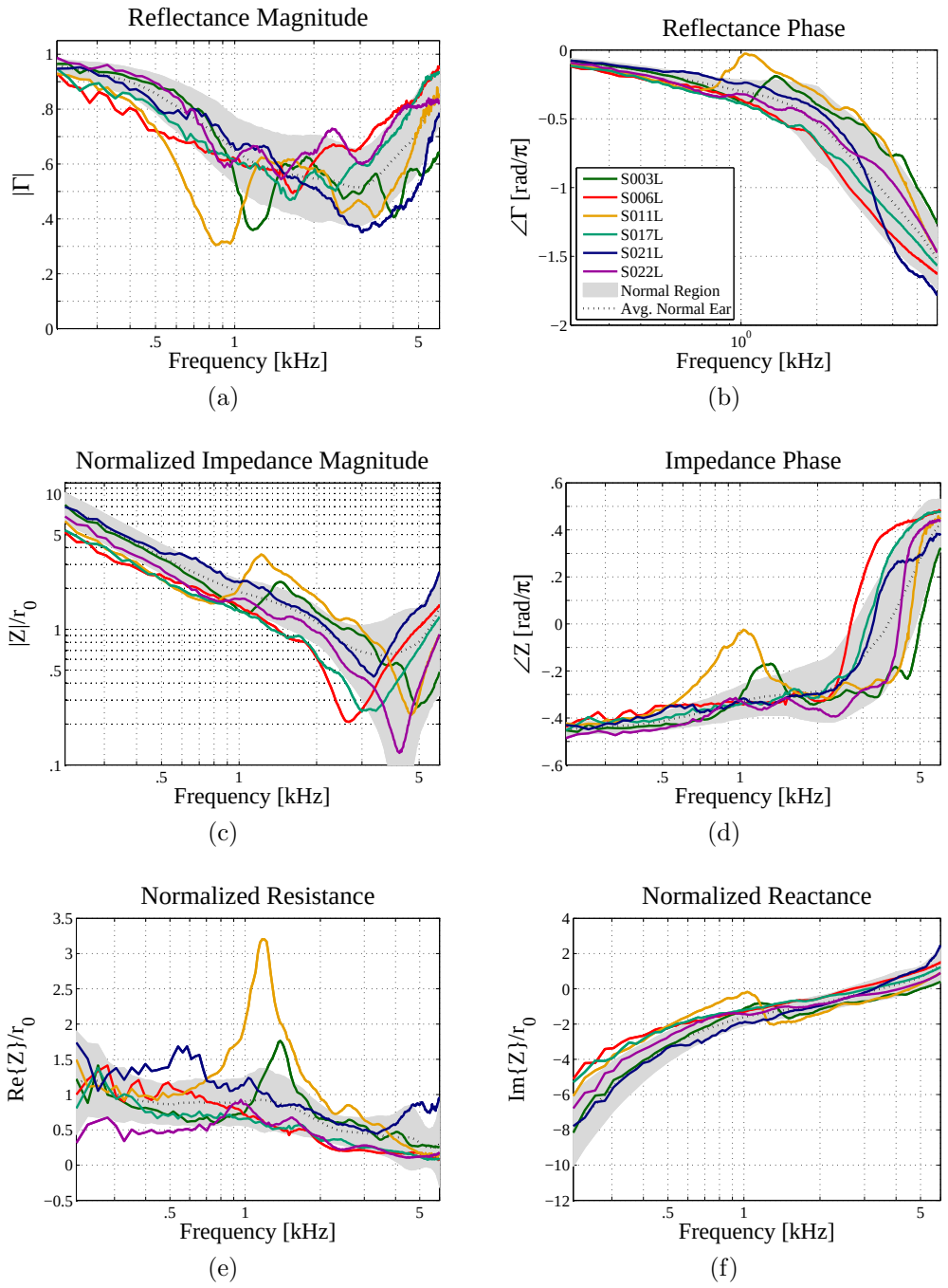

Figure 2.3: Reflectance properties of normal ears. (a) Reflectance magnitude, (b) reflectance phase, (c) normalized impedance magnitude, (d) impedance phase, (e) normalized resistance, (f) normalized reactance. Data are taken from Rosowski et al. [2012]; the dotted black lines show the average normal ear, and the light gray regions show ±1 standard deviation about the mean. Note that some individual ears, though defined as normal by audiometry, may have undetected middle ear conditions (e.g. S011L).

volume, which has some stiffness $1/C$ [Kinsler et al., 2000].

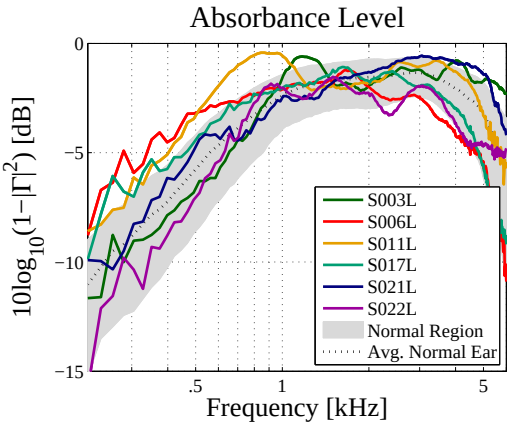

Figure 2.4: Absorbance level [dB]. Normative data and individual measurements are taken from Rosowski et al. [2012]; the dotted black lines show the average normal ear, and the light gray regions show ±1 standard deviation about the mean.

Figure 2.4 shows the *absorbance level* in [dB] [Allen et al., 2005, Rosowski et al., 2012], defined as

$$\text{Absorbance [dB]} \equiv 10\log_{10}(1 - |\Gamma(\omega)|^2), \tag{2.12}$$

where $1 - |\Gamma(\omega)|^2$ is the power absorbed by the middle ear. This representation of the CAR data was originated in Allen et al. [2005], where it was initially called the 'transmittance.' The mean and normative region of the absorbance level for normal middle ears have a very distinct shape. Rosowski et al. [2012] characterize the rising slope as 15 [dB] per decade and the falling slope as -23 [dB] per decade, with a flat region occurring between about 1 and 4 [kHz]. This is a useful way to characterize reflectance data, because deviations of the absorbance level from normal are more easily visually recognized. Assuming no significant leaks in the middle ear system (e.g. TM perforation), the absorbance is related to the middle ear transfer function and thus to hearing sensitivity [Allen et al., 2005, Rosowski et al., 2012]. Additionally, the absorbance level condenses in a rational way the region of individual variation in the magnitude reflectance for normal ears, to a range of a few decibels.

2.3.2 Pathological Ears

The amount of pathological CAR data is rapidly increasing. Early studies such as those by Feeney et al. [2003] and Allen et al. [2005] presented a few cases of known pathologies, showing that the middle ear pathologies appeared to have systematic effects on the wideband acoustic reflectance. Recent studies such as Hunter et al. [2010] (middle ear fluid in newborns), Nakajima et al. [2012] (stapes fixation due to otosclerosis, ossicular discontinuity, SSCD), Shahnaz et al. [2009] (otosclerosis) and Voss et al. [2012] (cadaver manipulations: positive/negative pressure, middle ear fluid, fixed stapes, ossicular discontinuity, perforations) have developed sizeable CAR databases for a number of pathologies, which may aid middle ear diagnosis based on CAR measurements. Some examples of pathological CAR data are given in Figure 2.5. These data are taken from Allen et al. [2005].

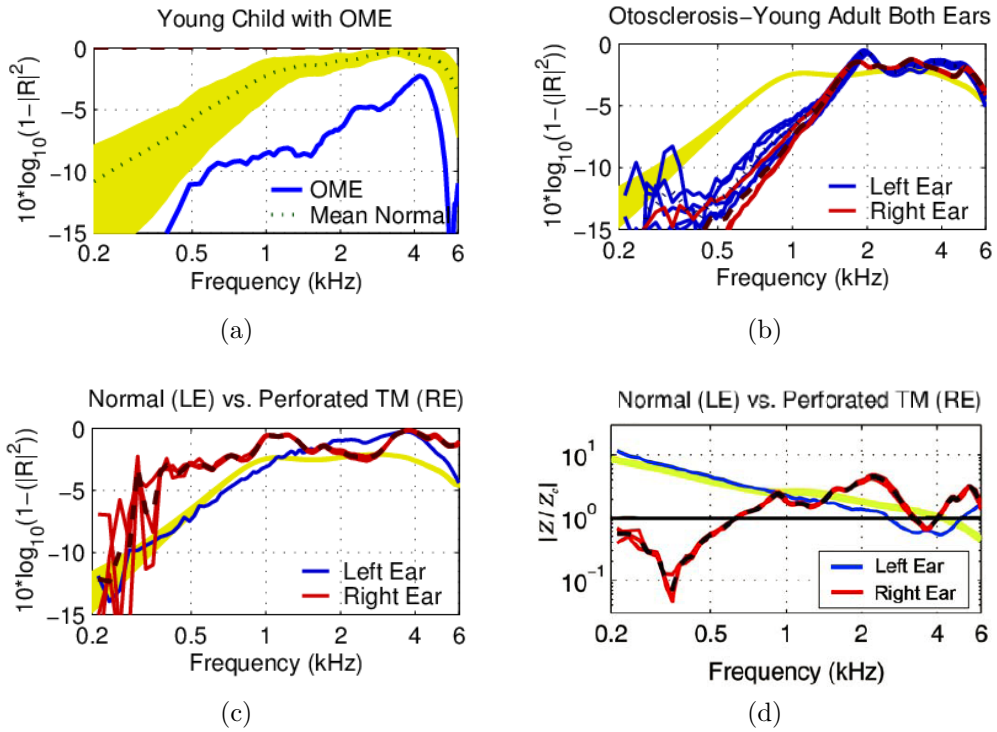

Figure 2.5: Pathological middle ears from Allen et al. [2005]. (a) Absorbance level [dB] of a child's ear with OM, (b) absorbance level [dB] of adult otosclerotic ears, (c) absorbance level [dB] of a normal adult ear compared to an ear with a perforated TM, (d) normalized impedance magnitude for the ears shown in (c).

Figure 2.5a shows a child's ear with OM with effusion, compared to nor-

mative data for 2.5 to 4 year old children. The power absorbance level is lower than normal for all frequencies due to the presence of fluid in the ear. According to Allen et al., the lower absorbance level was consistent with the measured elevation of hearing thresholds for the ear. Figure 2.5b shows an otosclerotic ear. The rising slope of the absorbance level has been shifted right (higher in frequency), corresponding to an increase in overall stiffness (a decrease in compliance). This is consistent with the notion that abnormal bone growth stiffens (limits the movement of) the ossicular chain.

Figures 2.5c and 2.5d, show the absorbance level and normalized impedance for an ear with a TM perforation. Allen et al. state that the perforation was about 3 to 4 [mm] in diameter, which is a significant size compared to the TM. Considering Fig. 2.5c, much more power is absorbed at low frequencies in the ear with a TM perforation, as compared to the normal ear. This does not necessarily mean that the power is conducted through the middle ear, as pressure waves may propagate through the TM hole but not actually drive the ossicular chain. The normalized impedance shows much less noise variation than the absorbance level, and a very distinct notch at about 350 [Hz]. This notch corresponds to a resonance, due to the hole in the TM. Voss et al. [2001] showed that for low frequencies and large perforations, the ear response can be simply modeled as a function of frequency, perforation diameter, and middle ear cavity volume. This is essentially a Helmholtz resonator, where the hole in the TM is the 'neck' and the middle ear space is the 'chamber.' Thus, the elevated absorbance level at low frequencies (Fig. 2.5c) corresponds to loss in the middle ear cavity.

It is clear from these examples that systematic changes of the CAR and impedance occur in the presence of middle ear pathologies. These changes may often be modeled based on physical intuition regarding the specific pathology. Figure 2.5 is intended as an example of this systematic behavior, but there are many more pathological studies, as referenced in Chapter 1. In this thesis, stapes fixation, ossicular discontinuity, and SSCD data are analyzed using pole-zero fitting; the systematic changes of the CAR due to these pathologies are described in tandem with the pole-zero results. Additionally, a novel study of bacterial biofilms is presented, detailing the systematic acoustic changes for five ears with confirmed biofilms and the corresponding pole-zero results.

CHAPTER 3

METHODS AND ANALYSIS

In this chapter, a pole-zero analysis for CAR measurements is presented. Pole-zero representation of CAR data is introduced, followed by a description of the fitting method. Some nuances of this method, such as the best domain for fitting (e.g. Γ, Z, or Y), are discussed. Finally, a method to compare complex fits across ears is introduced. This is a necessary consideration, because the unknown residual canal dimensions between the probe tip and TM cause undesired variation of the CAR across measurements.

The CAR data sets examined in this thesis were compiled from previous studies. A population of normal ears was drawn from Voss and Allen [1994] and Rosowski et al. [2012]. Fourteen CAR measurements of ten ears (four retest measurements) were collected in vivo up to 15 [kHz] by Voss and Allen using a measurement system described in their paper, along with measurements of two ear simulators, the B&K 4157 and the DB-100. Fifty-eight CAR measurements (and 58 retest measurements) were collected in vivo over a frequency range of 0.2 to 6 [kHz] by Rosowski et al., using the Mimosa Acoustics HearID system. These 58 "strictly normal" ears met specific audiometric criteria in order to be included in the study.

Pathological and cadaver measurements were drawn from Nakajima et al. [2012] and Voss et al. [2012]. The Nakajima et al. [2012] CAR measurements were collected in vivo from patients with confirmed stapes fixation due to otosclerosis, ossicular discontinuity, and superior semicircular canal dehiscence. The Voss et al. [2012] CAR measurements were collected from cadaver preparations, which were manipulated to simulate static pressure disorders in the middle ear cavity (positive and negative), middle ear fluid, fixed stapes, disarticulated incudo-stapedial joints, as well as TM perforations. Additionally, the cadaver ears were measured in their 'normal' (unmodified) state. These data were also collected using the Mimosa Acoustics HearID system.

3.1 Pole-Zero Representation of CAR Data

Poles and zeros may be expressed in terms of a rational polynomial fraction, as the roots of the denominator and numerator, respectively. Such a function will have the form

$$\begin{aligned}\hat{F}(s) &= \frac{b_{N_z}s^{N_z} + b_{N_z-1}s^{N_z-1} + ... + b_1 s + b_0}{s^{N_p} + a_{N_p-1}s^{N_p-1} + ... + a_1 s + a_0} \\ &= b_{N_z}\frac{\prod_{i=1}^{N_z}(s - z_i)}{\prod_{i=1}^{N_p}(s - p_i)},\end{aligned} \tag{3.1}$$

where s is the complex angular frequency variable ($s = \sigma + j\omega$), a_i and b_i are the polynomial coefficients, N_p is the number of poles, N_z is the number of zeros, p_i are the poles, and z_i are the zeros [Van Valkenburg, 1964]. For our application, the relative order is constrained to $|N_z - N_p| \leq 1$ by the fitting procedure (Appendix A). Poles and zeros are a familiar concept regarding impedance. Considering Eq. 2.3, the reflectance must also have poles and zeros via a simple algebraic transformation. Thus, $\hat{F}(s)$ may be a fit to the impedance Z, the reflectance Γ, or some other simple algebraic transformation of the data.

Some example CAR measurements (dots) and pole-zero fits (lines) are shown in Fig. 3.1 for two standard artificial ear simulators, the B&K 4157 (black) and the DB-100 (gray). These measurements are from Voss and Allen [1994]. Each fit is performed on reflectance domain data ($\Gamma(\omega)$) with $N_p = N_z = 6$; the B&K 4157 fit has a RMS relative error of 1.7%, and the DB-100 fit has a RMS relative error of 2.9%. Reflectance and impedance magnitude vs. frequency (Figs. 3.1a, 3.1b), and phase vs. frequency (Figs. 3.1c, 3.1d), are shown for both couplers. The impedance is normalized by the estimated surge resistance r_0. Effects of the residual simulator ear canals are particularly noticeable in the reflectance phase and normalized impedance magnitude graphs. Considering the reflectance phase (Fig. 3.1c), the DB-100 has a much flatter phase across frequency than the B&K 4157, indicating less delay and thus a shorter residual canal. The normalized impedance magnitude of the B&K 4157 shows a high 'standing wave' frequency notch, while the normalized impedance magnitude of the DB-100 does not. The absence of such a notch in the DB-100 impedance magnitude indicates a shorter distance

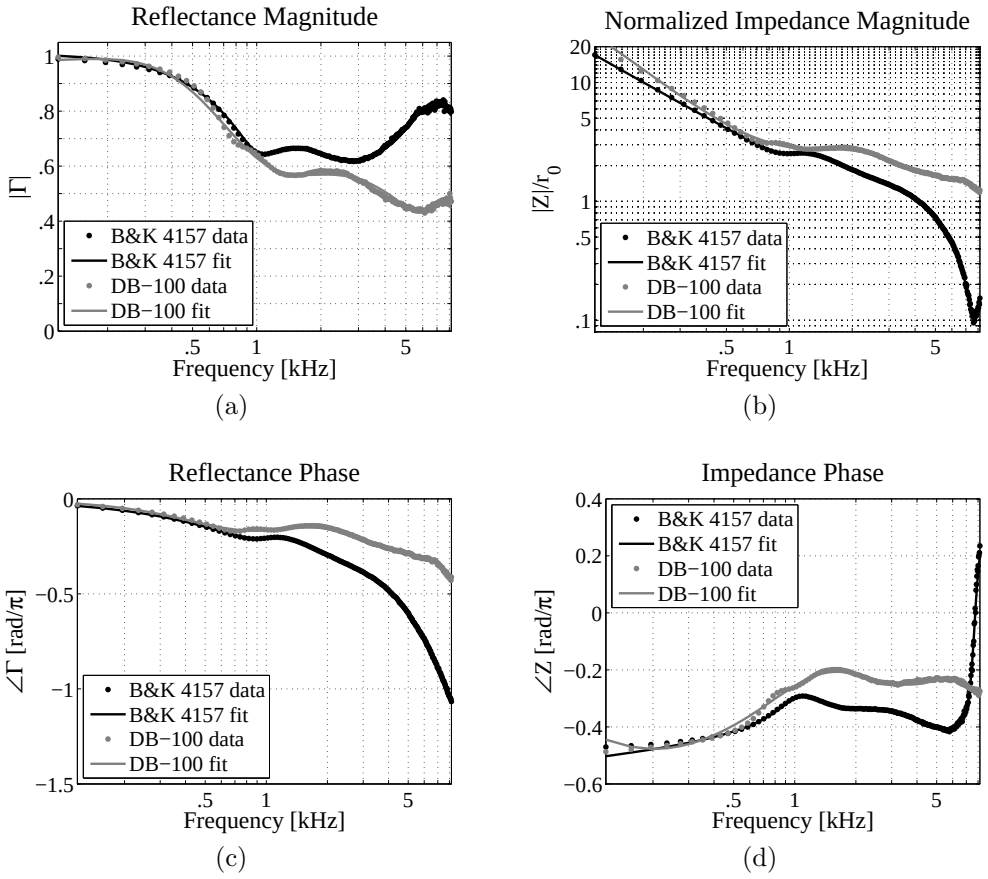

Figure 3.1: Standard ear simulator measurements from Voss and Allen [1994]. (a) Reflectance magnitude $|\hat{\Gamma}(j\omega)|$, (b) normalized impedance magnitude $|\hat{Z}(j\omega)|/r_0$, (c) reflectance phase $\angle\hat{\Gamma}(j\omega)$, (d) impedance phase $\angle\hat{Z}(j\omega)$. Example measured data (dots) and pole-zero fit (lines) are shown for the B&K 4157 (black) and the DB-100 (gray). The fits were performed in the reflectance domain over 0.1 to 8.2 [kHz], yielding 6 poles and 6 zeros for each fit. The B&K 4157 fit has a RMS relative error of 1.7%, and the DB-100 fit has a RMS relative error of 2.9%. The magnitude reflectance (a) of the B&K 4157 is more similar to an average normal ear across the entire frequency range than the DB-100. The DB-100 exhibits a much shorter ear canal behavior than the B&K 4157 considering the impedance magnitude (b) and the reflectance phase (c).

between the probe tip and TM; such a notch may still exist, but at a higher frequency outside of the measured range. Finally, considering the impedance magnitude and phase, the B&K 4157 ear canal impedance becomes mass dominated at high frequencies (beyond the standing wave frequency) while the DB-100 impedance does not.

According to Voss and Allen [1994], the reflectance magnitude of the DB-

100 ear simulator best resembles that of their ten human ear average below 4 [kHz], but the B&K 4157 is a better match to the average for frequencies up to 10 [kHz]. Considering Fig. 3.1a, the B&K 4157 reflectance magnitude is close to one at low frequencies, has a broad minimum from about 1 to 4 [kHz], and rises again at high frequencies; this is also similar to the average results obtained by Rosowski et al. [2012], among others. However, the reflectance magnitude of the DB-100 does not share this high frequency behavior, instead continuing to decrease above 4 [kHz]. Thus, the B&K 4157 measurement is a better standard for comparison of complex pole-zero fits, and will be used in this paper to represent an average normal ear. It is important to note that while the average magnitude reflectance of normal middle ears has a broad, flat minimum from about 1 to 4 [kHz], individual ears have variable fine-structure minima and maxima in this range [Rosowski et al., 2012, Allen et al., 2005]. These intersubject variations are typically due to anatomical differences across ears, including properties of the TM, ossicles, middle ear cavities and inner ear load [Voss et al., 2000, Aibara et al., 2001, Rosowski et al., 2012].

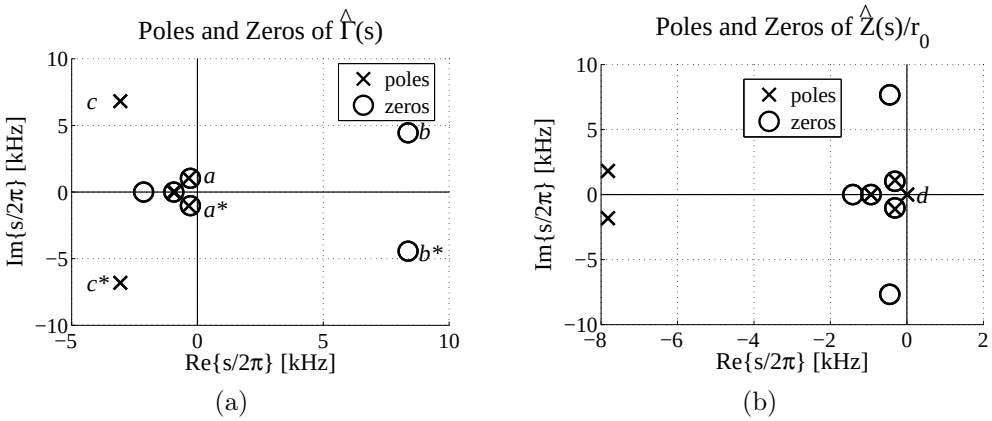

Figure 3.2: Pole-zero fit of the B&K 4157 measurement from Voss and Allen [1994]. (a) Poles and zeros of $\hat{\Gamma}(s)$, (b) poles and zeros of $\hat{Z}(s)/r_0$. Note that there are two closely-spaced poles on the real axis in Fig. 3.2a, though they appear to overlap on this scale. The fit was performed in the reflectance domain over 0.1 to 8.2 [kHz], and the impedance domain poles and zeros were calculated via Eq. 2.3. This pole-zero fit produces the curves shown in Fig. 3.1. The pole-zero pair labeled a (a) appears to characterize the first minimum of $|\hat{\Gamma}(j\omega)|$ (Fig. 3.1a), and the pole at d (b) appears to characterize the low-frequency stiffness of $|\hat{Z}(j\omega)|$ (Fig. 3.1b).

Figure 3.2 shows the poles and zeros that produce the fit to the B&K 4157

shown in Fig. 3.1. Figure 3.2a shows the poles and zeros of the reflectance fit $\hat{\Gamma}(s)$ and Fig. 3.2b shows the poles and zeros of the normalized impedance fit $\hat{Z}(s)/r_0$, which have been calculated from the fitted reflectance domain poles via Eq. 2.3. Notice that in both domains the poles and zeros have complex conjugate symmetry (those in the upper half s-plane mirror those in the lower half s-plane); this is a necessary condition for the polynomial coefficients in Eq. 3.1 to be real. With relation to the magnitude and phase response, the $\omega = \mathrm{Im}\{s\}$ location of a pole or zero typically determines the frequency region in which it has the largest effect, and the $\sigma = \mathrm{Re}\{s\}$ component of a pole or zero is related to the damping. Poles and zeros with smaller damping, which lie closer to the ω axis, have a larger effect on the fitted magnitude and phase responses. Throughout this presentation, pole-zero locations will be plotted as $s/(2\pi)$, such that the frequency axis $f = \omega/(2\pi)$ may be referenced to the frequency axes of the magnitude and phase responses.

Considering the poles and zeros of $\hat{\Gamma}(s)$ in Fig. 3.2a, the pole-zero pair labeled a (with conjugate a^*) seems to characterize the first minimum of the magnitude reflectance at 1 [kHz] (Fig. 3.1a), while the zero at b (b^*) and the pole at c (c^*) correspond to its high-frequency behavior. Considering the pole-zero plot of the normalized impedance $\hat{Z}(s)/r_0$ (Fig. 3.2b), note the solitary pole, labeled d, on the real axis approximately at the origin. This pole is actually in the *right half s-plane* (RHP), with a relatively small value of $\sigma/(2\pi) = 9$ [Hz], causing the impedance fit to be unstable. Because its $|\sigma|$ value is small, pole d is functionally at the origin; such small instabilities in the impedance can occur when fitting reflectance domain data, and will be discussed at length in Section 3.3. Because it is approximately at the origin, the pole at d characterizes the stiffness of the impedance below 1 [kHz]; it has a stronger effect on $|\hat{Z}(j\omega)|/r_0$ (Fig. 3.1b) than the other zeros and poles on the real axis, as it has the smallest σ value. Thus the pole-zero fits may be used to model some physics of CAR and impedance measurements.

It is important to note that pole-zero fitting of CAR data cannot be accomplished by autoregressive moving-average (ARMA) modeling methods (e.g. Recio-Spinoso et al., 2011), because the time domain signal $\gamma(t) = \mathcal{F}^{-1}\{\Gamma(\omega)\}$ (where $\mathcal{F}^{-1}$ denotes the inverse Fourier transform) is not very precise. CAR is measured as a function of frequency, and measurement noise below 100 or 200 [Hz] typically prevents the accurate calculation of an inverse FFT. Instead, a method developed by Gustavsen and Semlyen [1999] is used

to fit CAR data directly in the frequency domain. This procedure finds a rational approximation of the data as a function of complex frequency, using their 'vector fitting' method. Such pole-zero fits capture magnitude and phase characteristics of CAR measurements with low RMS relative error and a small set of parameters. The fitting procedure is described next, followed by fitting results for CAR data, and their diagnostic implications.

3.2 Pole-Zero Fitting Procedure

Rational approximations to the CAR data as a function of frequency ($\omega = 2\pi f$) were calculated using a vector fitting procedure developed by Gustavsen and Semylen [1999]. $\hat{F}(s)$, where $s = \sigma + j\omega$ is the complex angular frequency variable, will be used to denote the complex frequency domain fit, and $F(\omega)$ will be used to denote the measured complex frequency domain data. It is important to note that the data is only available as a function of ω, thus the data is related to the fitted function by $F(\omega) \approx \hat{F}(s)|_{s=j\omega}$; in words, when $\hat{F}(s)$ is evaluated along the ω axis of the complex s-plane, it approximates the observed data. Because the middle ear is not a lossless system, the poles and zeros of the fit are typically located off the ω axis (have non-zero σ values related to the damping). Thus $\hat{F}(s)|_{s=j\omega}$ typically has minima and maxima instead of zero and infinite values.

The data (e.g. the complex reflectance $\Gamma(\omega)$, impedance $Z(\omega)$, or admittance $Y(\omega) = 1/Z(\omega)$) is fit to a residue expansion of the form

$$\hat{F}(s) = \sum_{i=1}^{N_p} \frac{C_i}{s - A_i} + D + Es, \tag{3.2}$$

where the constants D and E are real quantities, while the constant poles and residues, A_i and C_i, are either real or occur in complex conjugate pairs. Note that if E and D are non-zero, the numerator order (N_z, as in Eq. 3.1) is one greater than the denominator order ($N_z = N_p + 1$). Similarly, if E is zero and D is non-zero the numerator and denominator orders are equal ($N_z = N_p$), and if both D and E are zero the numerator order is one less than the denominator order ($N_z = N_p - 1$). Equation 3.2 is nonlinear in its unknowns, because the unknown poles A_i appear in the denominator. Since

the poles and zeros of a 1-port network impedance are restricted to first order, with a relative order of $|N_z - N_p| \leq 1$, the functional form of Eq. 3.2 is sufficient for fitting impedance domain data [Van Valkenburg, 1964]. The reflectance does not have the same constraints, but given its relationship to impedance (Eq. 2.3) we assume it will also fit well to this form. It is important to note that while the total number of parameters may seem daunting, there are typically fewer 'degrees of freedom' than it seems, because the complex poles and zeros are constrained to come in complex conjugate pairs. For instance, if a fit has twelve poles and ten of them are complex, there are only seven 'degrees of freedom' related to the poles, because five (half) of the complex poles are constrained by conjugate symmetry. This constraint is preserved under the transformation in Eq. 2.3.

The vector fitting procedure is a two-step process, which converts a nonlinear least squares problem to a linear least squares problem by introducing an unknown scaling function with known poles [Gustavsen and Semlyen, 1999]. This procedure is described at length in Appendix A. Given a fixed number of poles, the algorithm converges very rapidly, usually within a few iterations. The algorithm may be re-run with an increasing number of poles, until some error criterion is met. For some measurements, the fitting procedure may return a set of poles and zeros with nearly overlapping pole-zero pairs, due to small extrema from measurement noise. Such pairs may be considered to 'overfit' the data, and it is often possible to eliminate them from the fit without causing an appreciable increase in the fitting error. For the remainder of this presentation, goodness of fit will be described using a *mean squared error* (MSE) metric, in decibels, relative to the L2 norm of the signal:

$$\text{MSE [dB]} = 10 \log_{10} \left[\frac{\sum |F(\omega) - \hat{F}(j\omega)|^2}{\sum |F(\omega)|^2} \right]. \tag{3.3}$$

A MSE of -30 [dB] corresponds to a relative error of about 3%.

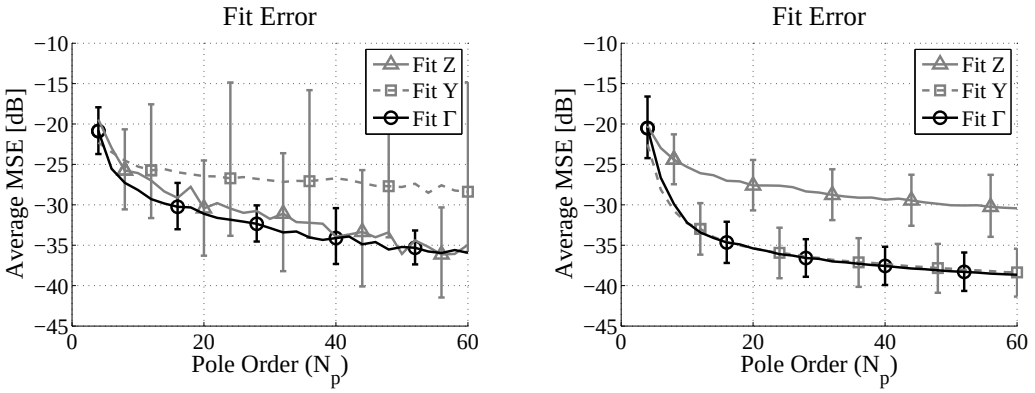

(a) Voss and Allen [1994] data

(b) Rosowski et al. [2012] data

Figure 3.3: Fit error evaluation across the impedance (Z), admittance (Y) and reflectance (Γ) domains for different data sets (18 iterations of the fitting algorithm). Lines show the average MSE [dB] vs. pole order (N_p) for each domain, with error bars indicating one standard deviation. (a) 14 measurements of normal ears [Voss and Allen, 1994] fit over the 0.1 to 10 [kHz] range, (b) 112 measurements of normal ears [Rosowski et al., 2012] fit over the 0.2 to 6 [kHz] range. Fitting measurements in the Γ domain achieves the lowest fitting error overall.

3.3 Domain of Fitting

An error analysis of the fitting procedure is given in Fig. 3.3. Average MSE vs. pole order is plotted for pole-zero fits of two data sets of normal middle ears in different domains. The impedance (Z), admittance (Y), and reflectance (Γ) domains are examined. Figure 3.3a shows the average MSE for fits of 14 normal ear measurements made by Voss and Allen [1994] over 0.1 to 10 [kHz]. Figure 3.3b shows the average MSE for fits of 112 normal ear measurements made by Rosowski et al. [2012] over 0.2 to 6 [kHz]. Error bars show ± 1 standard deviation of the MSE for a given data set and fitting domain. Considering Figs. 3.3a and 3.3b, the fit error saturates between about 10 and 20 poles, beyond which the algorithm begins to fit the measurement noise; this behavior is best captured by the admittance and reflectance domain curves in Fig. 3.3b, where the error improves by 15 [dB] between 4 and 20 poles, and by less than 5 [dB] between 20 and 60 poles. Figure 3.3a shows higher average MSEs than Fig. 3.3b. This is primarily because the Voss and Allen [1994] measurements were fit over a larger frequency range, which includes more noise than the Rosowski et al. [2012] measurement range. In Fig. 3.3a, impedance domain fitting performs better than admittance do-

main fitting, and vice versa in Fig. 3.3b, due to the frequency range of the fit and measurement noise. Because of the typical shape of the impedance response (e. g. Fig. 3.1b), low frequency noise has a larger effect on error in the impedance domain, and high frequency noise has a larger effect on error in the admittance domain. There are differing amounts of low and high frequency noise over the 0.1 to 10 [kHz] and 0.2 to 6 [kHz] ranges, causing differences in impedance domain error relative to admittance domain error.

Considering Fig. 3.3, the fitting procedure consistently performs best in the reflectance domain. Additionally, for diagnostic applications it may be desirable to have the best possible fit to the magnitude reflectance, which has shown the greatest promise for detecting middle ear pathologies. While the impedance magnitude and phase are both dominated by the ear canal response, in the reflectance domain only the phase is significantly affected by the ear canal (e.g. Eq. 2.8). Additionally, the dynamic range of the reflectance is much smaller than that of the impedance, typically spanning less than 10 [dB], whereas the impedance may span 20 to 40 [dB] (1 to 2 orders of magnitude). Due to the nature of the least squares procedure, small magnitude data points of $Z(\omega)$ inadvertently receive less emphasis in the fitting procedure than data points with larger magnitude. Thus, fitting to the impedance may provide a better approximation to the low frequency data (where the magnitude is large, as in Fig. 3.1b), but will yield a relatively poorer fit in the mid-frequency region of the reflectance magnitude, where individually varying minima and maxima occur for normal middle ears. To characterize the reflectance for a given ear, it may be useful to capture these fluctuations. Due to the smaller dynamic range of the reflectance, fitting the data in the reflectance domain gives approximately equal weight to the error across frequencies. Fitting 112 measurements over the 0.2 to 6 [kHz] range in the reflectance domain, an average MSE of -33.4 [dB] (2.1% RMS relative error with a standard deviation of 0.7%) is achieved with 12 poles for 18 iterations of the fitting algorithm. Fitting the data over a larger frequency range typically requires more poles.

Considering all measurements from the Rosowski et al. [2012] and Nakajima et al. [2012] studies, it was found that reflectance domain fits usually yield values of E (Eq. 3.2) that are close to zero. Typically, $|E|$ is very small for fits to both normal and pathological CAR measurements, on the order of 10^{-5} for fits with $N_p < 20$. For higher pole orders there is more variation

in the value of $|E|$, which is to be expected as the number of fitting parameters increases. The fact that the average $|E|$ values are similar for normal and pathological data sets indicates that this is a property of reflectance measurements and not a property of middle ear functionality. These results suggest that E should be forced to zero when fitting in the reflectance domain, enforcing a relative pole-zero order of $N_p \geq N_z$. For most fits, forcing E to be zero has a negligible effect on the error; often this effect may be remedied by adding a few more poles. However, the average value of $|D|$ is on the order of 1 for fits with $N_p < 20$. For instance, when fitting 112 measurements of normal ears from Rosowski et al. [2012] with $N_p = N_z = 12$, the average magnitude of D is 0.8 with a standard deviation of 0.4. Thus, it seems necessary to allow D to be non-zero when fitting in the reflectance domain, resulting in a relative pole-zero order of $N_p = N_z$. While it may not be obvious, this is a significant conclusion due to the physical meaning of D, as we will discuss in Section 7.2.

When the fitting procedure is performed in the reflectance domain, all fits to $\Gamma(\omega)$ are stable (all poles are in the *left half s-plane* (LHP)) because stability is enforced by the algorithm (see Appendix A). However, when the fit is transformed to the impedance domain by the relation in Eq. 2.3, stability is not ensured. If E is allowed to be non-zero, out of the fits performed to 112 measurements of $\Gamma(\omega)$ over 0.2 to 6 [kHz] [Rosowski et al., 2012] with a -30 [dB] MSE tolerance, no fits are stable when transformed to the impedance domain. With E forced to zero and all other conditions the same, 59 fits are stable in the impedance domain. All of these fits are also minimum-phase in the impedance domain, meaning that the zeros of $\hat{Z}(s)/r_0$ reside in the LHP as well as the poles, ensuring that both the impedance and admittance are causal and stable. Of the 53 remaining fits to $\Gamma(\omega)$ that are unstable when transformed to the impedance domain, 46 have a single pole of $\hat{Z}(s)/r_0$ that lies on the real axis in the RHP causing the instability; that pole has a mean value of $\sigma/2\pi = 17.8$ [Hz], with a standard deviation of 12.2 [Hz]. Thus, for these 46 fits, the unstable pole is approximately at the origin of the s-plane, characterizing the low frequency stiffness of $Z(\omega)$ for a normal middle ear. The remaining 7 fits to $\Gamma(\omega)$ which are unstable in the impedance domain have higher pole orders and may need more careful attention during the fitting procedure (e.g. the data is noisy). Note that the impedance should be minimum-phase, and it should also have the positive

real property, $\mathrm{Re}\{Z(\omega)\} \geq 0$ for all frequencies, assuming the system is passive [Brune, 1931]. Due to noise, some CAR measurements have $|\Gamma(\omega)| > 1$, corresponding to $\mathrm{Re}\{Z(\omega)\} < 0$ for some ω [Van Valkenburg, 1964]. Typically, all fits to these measurements will also have $|\hat{\Gamma}(j\omega)| > 1$.

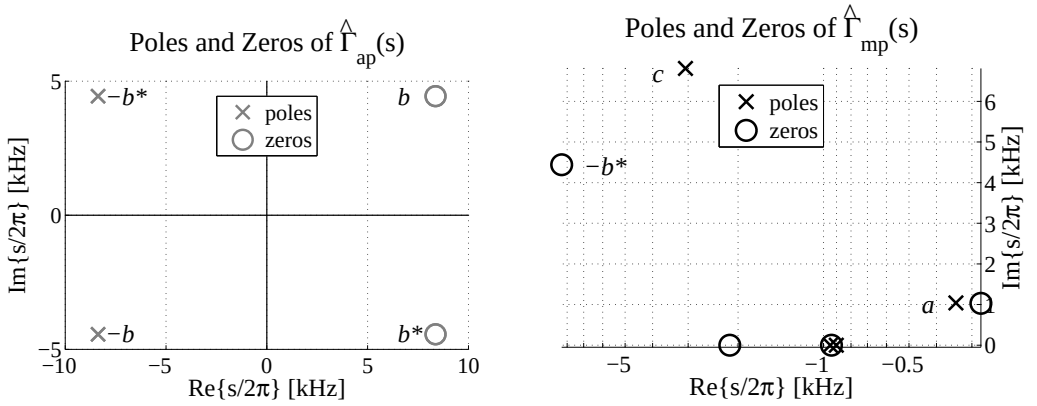

Figure 3.4: An example of the Weiner factorization (Eq. 3.4), using the B&K 4157 pole-zero fit (Fig. 3.2a). (a) Poles and zeros of $\hat{\Gamma}_{ap}(s)$, (b) poles and zeros of $\hat{\Gamma}_{mp}(s)$. Note that by definition $\hat{\Gamma}_{mp}(s)$ has no poles or zeros in the right half s-plane, thus the fit is completely described by northwest quadrant of the s-plane (shown in (b)). All poles and zeros in (b) with non-zero $\omega/(2\pi)$ values have complex conjugates in the southwest quadrant, not shown.

3.4 Comparing Complex Fits

Considering the CAR instead of its magnitude re-introduces the problem of comparing across measurements, because the residual ear canal introduces uncontrolled variation in the complex response (due to varying probe-TM distance, and canal area). This effect is difficult to extract, particularly because the limited high frequency range of the measurements does not allow for a good estimate of any pure delay in the ear canal. Even though measurements are available to 15 [kHz] for the Voss and Allen [1994] study, there is high frequency noise in the data that makes it difficult to accurately estimate the distance L from the probe to the TM (this point was previously made in their 1994 publication).

Under the assumption that the ear canal is lossless, and the rest of the middle ear system has loss, the reflectance may be factored such that the

residual ear canal effect is approximately removed. Using the Weiner factorization technique

$$\hat{\Gamma}(s) = \hat{\Gamma}_{mp}(s)\hat{\Gamma}_{ap}(s), \tag{3.4}$$

where $\hat{\Gamma}_{mp}(s)$ is the *minimum-phase* component and $\hat{\Gamma}_{ap}(s)$ is the *all-pass* component of the pole-zero fit $\hat{\Gamma}(s)$, it is possible to preserve the magnitude reflectance while removing variable residual canal delay.

By definition, it is required that all poles and zeros of a *minimum-phase* function lie in the LHP. To construct the minimum-phase component $\hat{\Gamma}_{mp}(s)$, we must factor a component out of $\hat{\Gamma}(s)$ that accounts for all zeros that lie in the RHP (if the fit was performed in the reflectance domain, all poles will be constrained to the LHP by the fitting algorithm). Let the function $\hat{\Gamma}_{LHP}(s)$ contain all the poles and zeros of $\hat{\Gamma}(s)$ that lie in the LHP; let $N_{z,RHP}$ be the number of RHP zeros of $\hat{\Gamma}(s)$, with values q_i. The reflectance fit may be factored as follows:

$$\begin{aligned}
\hat{\Gamma}(s) &= \hat{\Gamma}_{LHP}(s) \prod_{i=1}^{N_{z,RHP}} (s - q_i) \\
&= \hat{\Gamma}_{LHP}(s) \prod_{i=1}^{N_{z,RHP}} (s - q_i)\frac{(s + q_i^*)}{(s + q_i^*)} \\
&= \underbrace{\left[\hat{\Gamma}_{LHP}(s) \prod_{i=1}^{N_{z,RHP}} (s + q_i^*)\right]}_{\hat{\Gamma}_{mp}(s)} \underbrace{\left[\prod_{i=1}^{N_{z,RHP}} \frac{(s - q_i)}{(s + q_i^*)}\right]}_{\hat{\Gamma}_{ap}(s)}.
\end{aligned} \tag{3.5}$$

Considering Eq. 3.5, overlapping poles and zeros are introduced in the LHP at $s = -q_i^*$. Grouping the terms, a component with LHP poles and RHP zeros symmetrically placed about the ω axis emerges. This is called the *all-pass* component, because its magnitude $|\hat{\Gamma}_{ap}(j\omega)|$ is 1 for all frequencies in the fitting range; it passes all frequencies with no attenuation. The factorization required to form the all-pass component is unique. The remaining terms contain only poles and zeros in the LHP, and form the minimum-phase factor $\hat{\Gamma}_{mp}(s)$. When working with poles and zeros, this factorization requires no additional calculations.

An example of this factorization is shown in Fig. 3.4. Figure 3.4a shows the all-pass component and Fig. 3.4b shows the minimum-phase component of the reflectance fit shown in Fig. 3.2a (the B&K 4157). Note that Fig. 3.4b

shows only the northwest quadrant of the s-plane. This style of plotting will be used for all $\hat{\Gamma}_{mp}(s)$ results; though limited to one quadrant of the LHP, it completely describes the set of poles and zeros for a given fit. By definition, $\hat{\Gamma}_{mp}(s)$ only has poles and zeros in the LHP. Thus, a logarithmic σ axis may be used for the LHP (northwest and southwest quadrants), on which the large dynamic range of σ values may be more easily viewed. Because the southwest quadrant contains only complex conjugates of the poles and zeros in the northwest quadrant, it does not need to be shown. Considering Fig. 3.2a, the zeros at b and b^* correspond to the q_i's in Eq. 3.5. To factor the fit, overlapping poles and zeros are introduced at -b^* and -b, respectively; the zeros are assigned to $\hat{\Gamma}_{mp}(s)$ (Fig. 3.4b), and the poles are assigned to $\hat{\Gamma}_{ap}(s)$ (Fig. 3.4a) along with the RHP zeros of $\hat{\Gamma}(s)$. Note how the poles and zeros of $\hat{\Gamma}_{ap}(s)$ are symmetrically placed about the ω axis, such that the poles and zeros at b, b^*, -b^* and -b are constrained by both complex conjugation and all-pass symmetry.

The minimum-phase and all-pass factors have the following properties:

$$|\hat{\Gamma}_{mp}(j\omega)| = |\hat{\Gamma}(j\omega)| \tag{3.6}$$

$$|\hat{\Gamma}_{ap}(j\omega)| = 1 \tag{3.7}$$

$$\angle\hat{\Gamma}_{mp}(j\omega) + \angle\hat{\Gamma}_{ap}(j\omega) = \angle\hat{\Gamma}(j\omega). \tag{3.8}$$

The reflectance magnitude is maintained in the minimum-phase component of the fit, while the component of the reflectance that is uniformly lossless across the frequency range of the fit, including any pure delay, is accounted for in the all-pass component. Because the factors are multiplied, their phases add.

Assuming negligible losses in the ear canal, we may approximate the residual ear canal contribution to the reflectance as the all-pass component $\hat{\Gamma}_{ap}(s)$. In some cases, the all-pass component of the factorization has an approximately linear phase (constant group delay), resulting in a robust estimate $\hat{L}$ of the ear canal length according to Eq. 2.8. From this equation, the constant group delay may be calculated as

$$\tau_{ap}(\omega) = -\frac{d\phi_{ap}(\omega)}{d\omega} \approx \frac{2\hat{L}}{c}, \tag{3.9}$$

where $\phi_{ap}(\omega)$ is the phase of $\hat{\Gamma}_{ap}(j\omega)$. If $\tau_{ap}(\omega)$ is frequency dependent, a

frequency independent delay may be estimated by taking its minimum over the measured frequency range. When $\hat{\Gamma}_{ap}(s)$ gives a good approximation to the residual ear canal component of the reflectance,

$$\hat{\Gamma}_{mp}(s) \approx \Gamma_{TM}(s). \tag{3.10}$$

Thus, from this factorization it is possible to estimate the normalized TM impedance using Eq. 2.3,

$$\frac{\hat{Z}_{TM}(s)}{r_0} = \frac{1+\hat{\Gamma}_{mp}(s)}{1-\hat{\Gamma}_{mp}(s)}. \tag{3.11}$$

When the approximate residual ear canal contribution has been removed, the magnitude TM impedance $|\hat{Z}_{TM}(j\omega)|/r_0$ typically has no high frequency notch due to ear canal standing waves. In the case of a uniform ear canal area $A(x)$, the TM impedance estimate is similar to the 'propagated impedance' function described by Voss and Allen [1994], calculated by removing a pure delay from the reflectance.

CHAPTER 4

POLE-ZERO CHARACTERIZATION OF MIDDLE EAR CAR DATA

The factorization of CAR pole-zero fits into their all-pass and minimum-phase components is examined in the following sections. This factorization is intended to characterize the residual ear canal effect on individual CAR measurements, in order to enable comparison of complex pole-zero fits across ears. Residual canal lengths estimated from the all-pass characterization are presented to support this approximation. Finally, the sensitivity of individual poles, zeros, and pole-zero pairs is examined in order to show how pole-zero locations of the minimum-phase component of the CAR characterize the reflectance magnitude. This analysis provides intuition for the pole-zero representation of CAR data.

4.1 Factorization of $\hat{\Gamma}(s)$

An example factorization is shown in Fig. 4.1 for a normal ear, subject #7 of Voss and Allen [1994]. The fit was performed in the reflectance domain over 0.1 to 10 [kHz], yielding $N_p = 18$ and $N_z = 18$ with a MSE of -31.9 [dB]; approximately overlapping pole-zero pairs at $\omega/(2\pi) \approx 7.5$ [kHz] and $\omega/(2\pi) \approx 9$ [kHz] were removed, yielding a MSE of -31.5 [dB] and $N_p = 14$ and $N_z = 14$. Figures 4.1a and 4.1b show the poles and zeros of the all-pass and minimum-phase components of $\hat{\Gamma}(s)$, similar to Figs. 3.4a and 3.4b. Note again how the poles and zeros of $\hat{\Gamma}_{ap}(s)$ (Fig. 4.1a) are symmetrically placed about the ω axis, such that the zero labeled a has a symmetrical counterpart at $-a^*$, and the poles and zeros at f, f^*, $-f^*$ and $-f$ are constrained by both complex conjugation and all-pass symmetry. Considering Fig. 4.1b, the pole-zero pairs labeled b, c, d and e correspond in frequency ($f = \omega/(2\pi)$) to minima of the magnitude reflectance, as labeled in Fig. 4.1c. The first pair, labeled b, is located at about 1 [kHz], corresponding to the first minimum

of the magnitude reflectance. This is similarly located to the pole-zero pair at a in Fig. 3.4b, which corresponds to the first minimum of the B&K 4157 magnitude reflectance in Fig. 3.1a; it is aligned with the low frequency edge of the broad minimum in $|\Gamma(\omega)|$ for average normal ears. While the B&K 4157 reflectance fit has an approximately flat magnitude from 1 to 4 [kHz] and has no more pole-zero pairs in this region, the reflectance fit for Voss and Allen subject #7 has closely spaced pole-zero pairs at c, d and e that correspond to the individually varying minima and maxima of the reflectance magnitude in that frequency region.

The total phase and the phases of the all-pass and minimum-phase components of the reflectance fit are shown in Fig. 4.1d. The phase of $\hat{\Gamma}_{ap}(j\omega)$ appears linear, while the phase of $\hat{\Gamma}_{mp}(j\omega)$ appears flatter than $\angle\hat{\Gamma}(j\omega)$, meaning it contains less delay from the residual ear canal. This is apparent in the group delay as well, shown in Fig. 4.3a for the reflectance fit and its all-pass and minimum-phase components. The group delay of the all-pass component of the reflectance appears constant, with a value equal to the gap between the curves for the original reflectance fit and its minimum-phase component. Because the phase of the all-pass component is approximately linear (its group delay is approximately constant), the canal delay may be estimated by Eq. 3.9. For subject #7 [Voss and Allen, 1994], the group delay of $\hat{\Gamma}_{ap}(j\omega)$ has a mean value across frequency of $\bar{\tau}_{ap} = 40.4$ [μs], with a standard deviation of 0.5 [μs]. Taking $\hat{L} = \bar{\tau}_{ap}c/2$ with $c = 350$ [m/s], the estimated residual canal length $\hat{L}$ is 7.1 [mm]; taking $\min(\tau_{ap}) = 38.9$ [μs], the estimated length is 6.8 [mm]. These are reasonable estimates, given that Voss and Allen estimate the length of the foam plug plus probe at 15 [mm], and the typical total ear canal length between the opening and center of the TM is about 23.5 [mm] [Fletcher, 1925]. The TM impedance and phase are shown in Figs. 4.1e and 4.1f. Removing the all-pass component from the reflectance fit $\hat{\Gamma}(s)$ removes the deep notch in the impedance magnitude ($|\hat{Z}_{TM}(j\omega)|/r_0$ does not have a high frequency notch), and causes the impedance phase to have no jump at the $|Z(\omega)|$ notch frequency.

A second example factorization is shown in Fig. 4.2. This is cadaver ear 12R from the Voss et al. [2012] study, in its normal (unmodified) state. The fit was performed in the reflectance domain over 0.2 to 6 [kHz], yielding $N_p = 12$ and $N_z = 12$ with a MSE of -35.8 [dB]. Figures 4.2a and 4.2b show the poles and zeros of the all-pass and minimum-phase components of $\hat{\Gamma}(s)$.

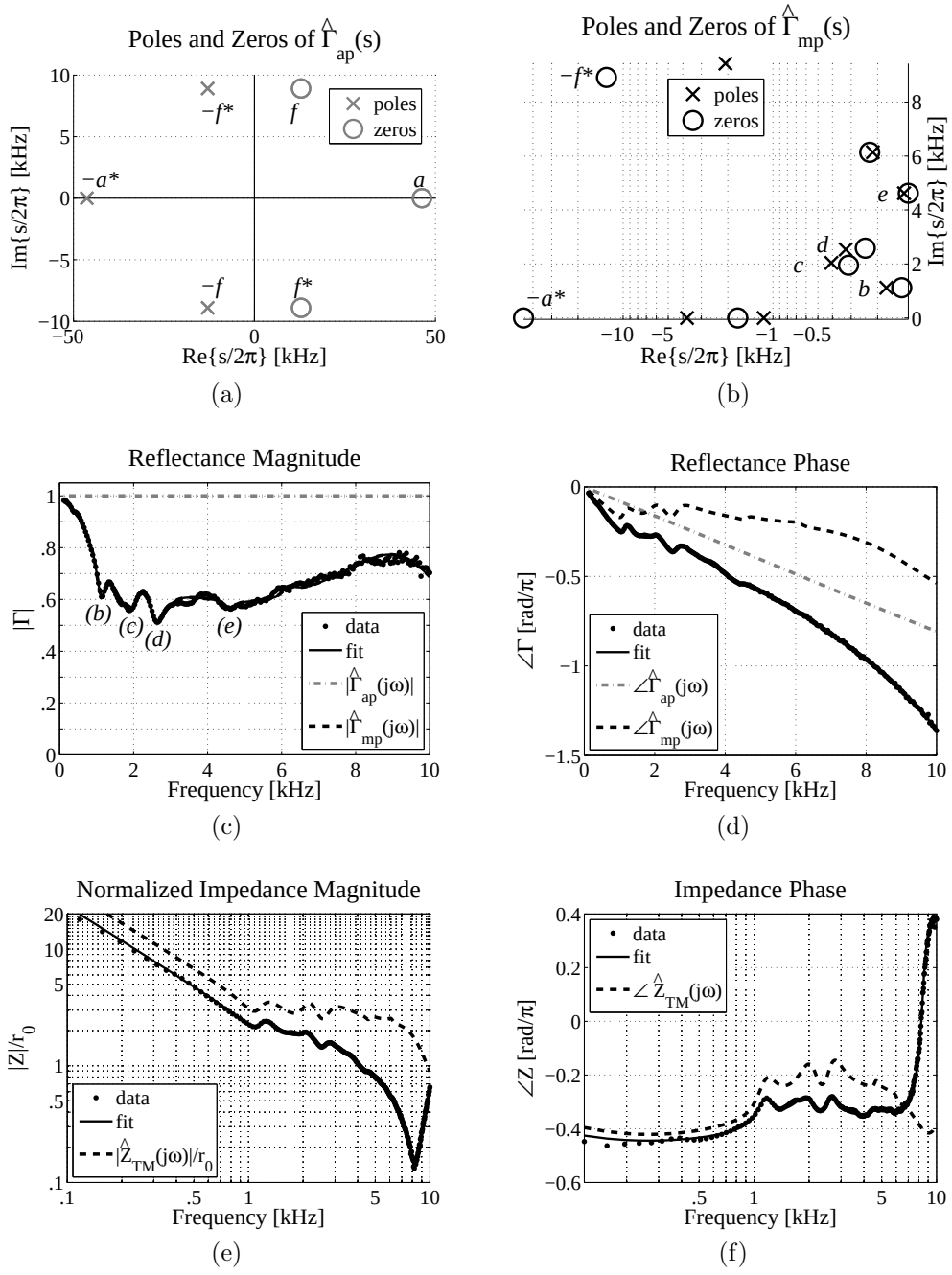

Figure 4.1: Factored reflectance fit for subject #7 from Voss and Allen [1994]. (a) Poles and zeros of $\hat{\Gamma}_{ap}(s)$, (b) poles and zeros of $\hat{\Gamma}_{mp}(s)$, (c) reflectance magnitude, (d) reflectance phase, (e) impedance magnitude, (f) impedance phase. Note that $\hat{\Gamma}_{mp}(s)$ has no poles or zeros in the right half s-plane, thus it is completely described by northwest quadrant of the s-plane. The fit was performed in the reflectance domain over 0.1 to 10 [kHz], yielding $N_p = 14$ and $N_z = 14$ with a MSE of -31.5 [dB].

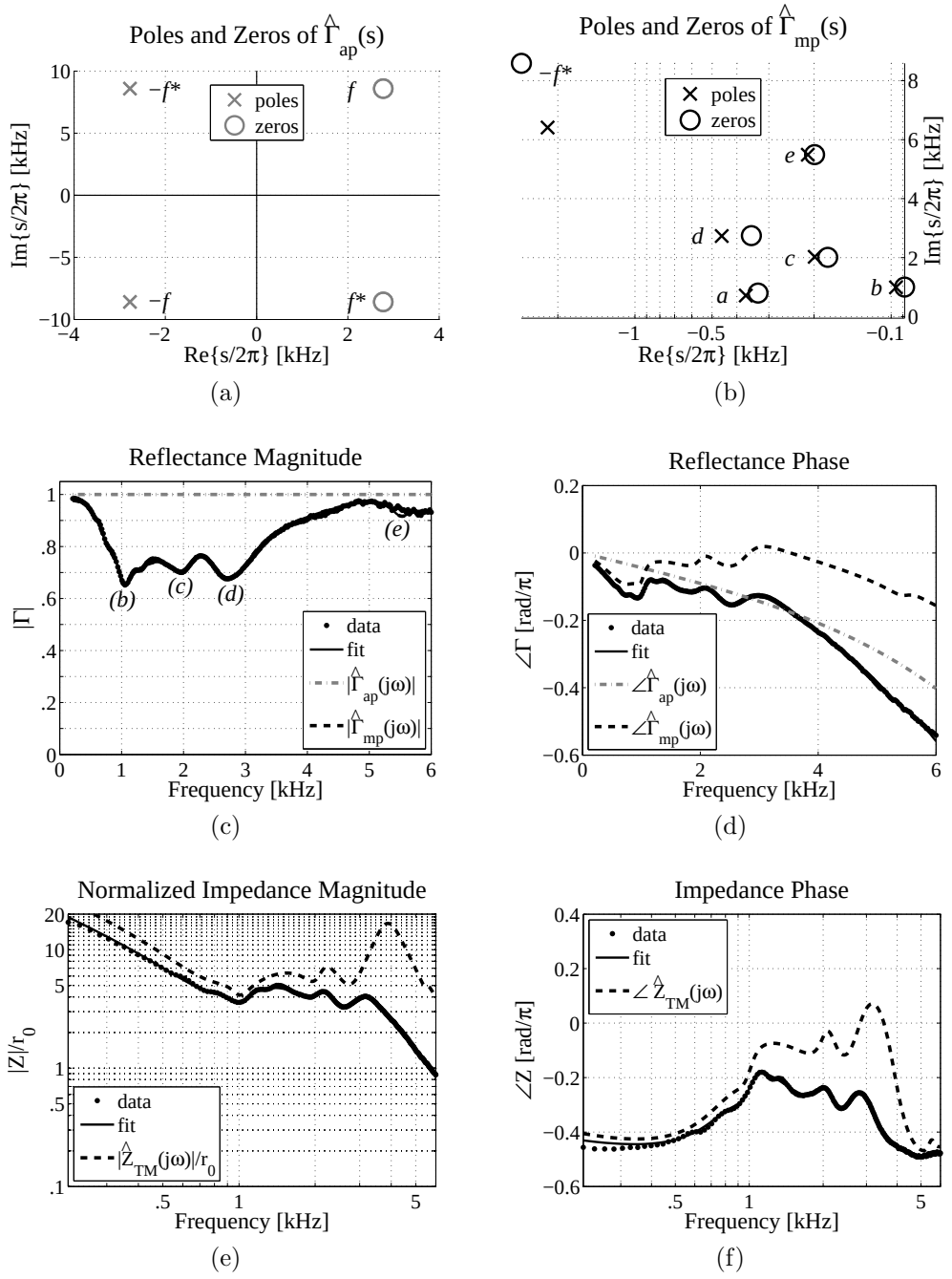

Figure 4.2: Factored reflectance fit for cadaver ear 12R from Voss et al. [2012]. (a) Poles and zeros of $\hat{\Gamma}_{ap}(s)$, (b) poles and zeros of $\hat{\Gamma}_{mp}(s)$, (c) reflectance magnitude, (d) reflectance phase, (e) impedance magnitude, (f) impedance phase. Note that $\hat{\Gamma}_{mp}(s)$ has no poles or zeros in the RHP, thus it is completely described by northwest quadrant of the s-plane. The fit was performed in the reflectance domain over 0.2 to 6 [kHz], yielding $N_p = 12$ and $N_z = 12$ with a MSE of -35.8 [dB].

Considering Fig. 4.2b, the pole-zero pairs labeled b, c, d and e correspond in frequency to minima of the magnitude reflectance labeled in Fig. 4.2c. The pole-zero pair labeled b is located at $\omega/(2\pi) = 1$ [kHz], corresponding to the first minimum of the fit, $|\hat{\Gamma}(j\omega)|$, (similar to Voss and Allen subject #7 and the B&K 4157 ear simulator), and the pole-zero pairs at c and d correspond to the individually varying minima and maxima in the mid-frequency region of the magnitude reflectance. The pole-zero pair at a seems to correspond to a small bend in the reflectance below 1 [kHz]; presumably, it has a smaller effect on $|\hat{\Gamma}(j\omega)|$ because it has more damping than the pairs at b and c, and the pole and zero are closer to overlapping than the pair at d. The tightly spaced pair labeled e corresponds to a small dip in a noisy region of the magnitude reflectance between 5 and 6 [kHz].

The total phase and the phases of the all-pass and minimum-phase components of the reflectance fit are shown in Fig. 4.2d for ear 12R from Voss et al. [2012]. Here the all-pass component phase $\angle\hat{\Gamma}_{ap}(j\omega)$ appears to have a frequency dependent delay. Considering Figs. 4.2e and 4.2f, neither the approximated TM impedance $\hat{Z}_{TM}(j\omega)/r_0$ nor the data $Z(\omega)/r_0$ show a standing wave notch in the magnitude impedance, or a jump in the phase at high frequencies. This behavior is indicative of a very short ear canal distance between the probe tip and the TM. The magnitude TM impedance $|\hat{Z}_{TM}(j\omega)|/r_0$ is relatively large at high frequencies in comparison with Fig. 4.1e; however, this seems plausible because the magnitude reflectance of the cadaver ear (Fig. 4.2c) is much closer to 1 at high frequencies than the magnitude reflectance of the normal ear (Fig. 4.1c, Voss and Allen subject #7).

Unlike measurements made in vivo, CAR measurements of cadaver ears typically have a much shorter residual ear canal, due to the nature of the preparation. For this ear, the group delay of the reflectance all-pass component, shown in Fig. 4.3b, is not constant. For Voss et al. [2012] ear 12R the mean group delay is 34.0 [μs] over the entire frequency range of the fit, with a standard deviation of 12.2 [μs]. Instead, a frequency independent group delay, estimated as the minimum value of the group delay of $\hat{\Gamma}_{ap}(j\omega)$ over the 0.2 to 6 [kHz] range ($\min(\tau_{ap}) = 21.7$ [μs]), yields the estimate $\hat{L} \approx 3.8$ [mm]. This is short compared to $\hat{L}$ for the in vivo measurement in the preceding example, which makes sense given the measurement conditions for cadaver ears. Variation of the all-pass group delay with frequency may be accounted for by non-uniform area of the ear canal, or lossless mass-stiffness properties

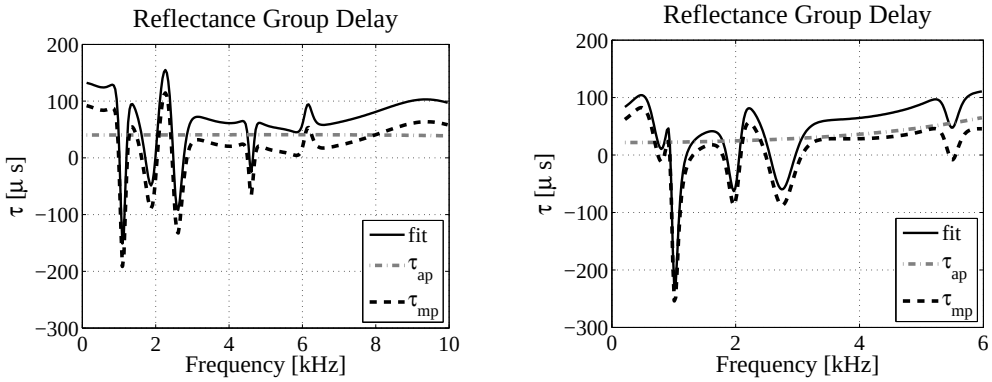

(a) Subject #7 (Fig. 4.1) (b) Cadaver ear 12R (Fig. 4.2)

Figure 4.3: Group delay of the fit $\hat{\Gamma}(s)$, and its factors $\hat{\Gamma}_{mp}(s)$ and $\hat{\Gamma}_{ap}(s)$. (a) Voss and Allen [1994] subject #7, (b) Voss et al. [2012] cadaver ear 12R ('normal' unmodified state). In (a), $\hat{\Gamma}_{ap}(s)$ has an approximately constant group delay; in (b), $\hat{\Gamma}_{ap}(s)$ has a frequency dependent group delay.

of the TM and middle ear. The TM in particular may contribute a significant amount of lossless delay [Puria and Allen, 1998, Parent and Allen, 2010].

Estimating the residual ear canal length from the all-pass factor of the reflectance fit, the probe-TM distance for the B&K 4157 and DB-100 ear simulators are estimated to be 7.6 [mm] and 2.3 [mm], respectively. Considering Fig. 3.1, these results are reasonable, and agree with the observations made in Section 3.1. While the B&K 4157 shows large residual canal effects in the magnitude impedance and reflectance phase, the DB-100 does not. With a shorter probe-TM distance, the standing wave impedance notch for the DB-100 would be at a higher frequency than that for the B&K 4157, outside of the range shown. Additionally, the shorter canal of the DB-100 simulator requires the probe tip to be much closer to the middle ear (TM) for a good acoustic seal.

Finally, it is of note that the all-pass factors $\hat{\Gamma}_{ap}(s)$ in Figs. 3.4a, 4.1a, and 4.2a bear some resemblance to the equal order Padé approximation of a pure delay, $e^{-j\omega\tau}$. In Serwy [2012], it is shown that the equal order Padé approximation of a pure delay gives rise to poles and zeros that are symmetrically placed about the $j\omega$ axis, in an oval-like formation centered at the origin (where all poles are in the LHP, all zeros are in the RHP, and the poles and zeros have conjugate symmetry). This rounded configuration is particularly apparent in Fig. 4.1a, where the pole and zero on the real axis have larger $|\sigma|$ values than the other poles and zeros. This configuration

indicates that $\hat{\Gamma}_{ap}(s)$ may be related to a pure delay. In fact, considering the approximately constant $\tau_{ap}(\omega)$ in Fig. 4.3a, it is clear that the all-pass component shown for Voss and Allen [1994] subject #7 in Fig. 4.1a must represent an approximately pure delay.

4.2 Estimating the Residual Canal Length

Factoring the reflectance fit into its all-pass and minimum-phase components according to Eq. 3.4, it appears that for most fits the ear canal is approximately accounted for. Using the approximation in Eq. 3.11, the estimated eardrum impedance typically shows no high frequency 'standing wave' notch due to reflections between the probe tip and the eardrum. At the very least, the minimum-phase component $\hat{\Gamma}_{mp}(s)$ preserves the magnitude reflectance.

Considering the all-pass component of the reflectance, the length of the residual ear canal is estimated via

$$\hat{L} = \min_{\omega} \left[-\frac{d}{d\omega} \left[\angle \hat{\Gamma}_{ap}(j\omega) \right] \right] \times \frac{c}{2}, \tag{4.1}$$

which is equal to $\min(\tau_{ap})$ for all frequencies in the fitting range. For an ear canal of uniform area, the all-pass component group delay may be approximately constant across frequency as in Eq. 3.9. However, because the ear canal typically has a non-uniform area between the probe tip and eardrum, it is necessary to estimate the frequency-independent delay by taking the minimum across frequencies. For the estimates presented here $c = 350$ m/s, which is the approximate speed of sound at body temperature.

Table 4.1 shows the residual ear canal lengths estimated by this procedure for the ears and simulators measured by Voss and Allen [1994], along with the length estimates used by Voss and Allen to calculate an 'advanced impedance.' Voss and Allen mention that these lengths are somewhat arbitrarily chosen, such that when a pure delay was removed the reflectance phase remained between 0 and 2π. To estimate the canal lengths using $\hat{\Gamma}_{ap}(s)$, the CAR measurements were fit over a range of 0.1 to 8.2 kHz; these fits had an average RMS relative error of 2.3%, and 6 to 14 poles (with an equal number of zeros). Depending on the frequency range of fitting and the goodness of fit, residual canal length estimates may vary. For instance, when the Voss

Table 4.1: Estimated residual canal lengths between the probe tip and eardrum for 10 normal ears and 2 ear simulators from Voss and Allen [1994]. The estimates made by Voss and Allen were determined by removing pure delay from the data, keeping the reflectance phase between 0 and 2π. The estimates made in this study were calculated via Eq. 4.1.

Subject	$\hat{L}$ **[mm] (V&A '94)**	$\hat{L}$ **[mm] (this study)**	$\mathbf{\Delta}$ [mm]
1	10.0	8.7	1.3
2	12.0	7.4	4.6
3	5.5	4.9	0.6
4	5.875	10.4	4.525
5	3.0	1.8	1.2
6	0	0.2	0.2
7	8.0	8.7	0.7
8	8.0	6.7	1.3
9	7.0	8.1	0.9
10	7.0	3.4	3.6
DB-100	2.0	2.3	0.3
B&K 4157	8.0	7.6	0.4

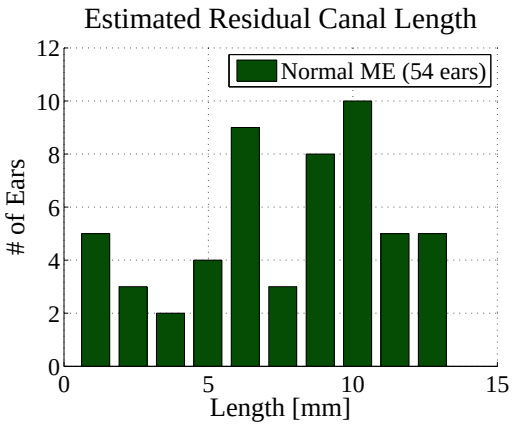

Figure 4.4: Histogram (bin width = 1.30 mm) of estimated residual canal lengths between the probe tip and eardrum for 54 ears from Rosowski et al. [2012]. These estimates were calculated via Eq. 4.1. These estimated lengths are within a reasonable range given the probe configuration in the ear canal.

and Allen [1994] subject #7 measurement is fit over 0.1 to 10 [kHz], $\hat{L}$ is estimated to be 6.8 [mm] (Section 4.1) instead of 8.7 [mm] (Table 4.1). Thus it seems that the broader the frequency range over which $\hat{L}$ is estimated, the more conservative the estimate is likely to be. Results may also differ based on the parameters of the fit, such as the number of poles, N_p.

In many cases, these estimates seem to remove the ear canal effect (impedance standing wave), or significantly reduce it. Voss and Allen estimated their probe to be 15 mm in length, while the typical total ear canal length is about 23.5 mm [Fletcher, 1925]. Thus, the canal length estimates shown in Table 4.1 for both studies are reasonable, considering that the canal may vary in length, and that the back of the probe may or may not be flush against the ear canal opening.

Figure 4.4 shows a histogram of residual canal lengths estimated via Eq. 4.1 for 54 normal ears from the Rosowski et al. [2012] study. Considering that the probe tip is comparable in length to that used in the Voss and Allen [1994] study, these lengths are also reasonable. The CAR measurements were fit over a range of 0.2 to 6 kHz; these fits had an average RMS relative error of 2.5%, and 8 to 14 poles (with an equal number of zeros). Of the missing four ears, two measurements were not included in the data we received, and two measurements were too noisy to yield acceptable pole-zero fits.

4.3 Sensitivity Analysis of Pole-Zero Fits

Figures 4.5 and 4.6 show data and pole-zero fits of four reflectance measurements of ears with varying middle ear conditions (one normal + three pathologies). Figure 4.5 shows a reflectance summary including the magnitude reflectance (Fig. 4.5a) and absorbance level (Fig. 4.5b), while Fig. 4.6 shows a sensitivity analysis of various poles and zeros for each measurement. These poles and zeros were chosen to help the reader develop an intuition for the effect of pole-zero locations on the magnitude response. This exercise is meant as a tour of the pole-zero fits for various pathologies; two poles, zeros, or pole-zero pairs are chosen for each pathology, but any poles and zeros of the fit could be analyzed in this way.

Figure 4.6 is comprised of four subplots. In each subplot, the left panel shows two sensitivity analyses of poles and zeros from the right panel; different analyses are color-coded in red and blue. These color-coded regions display ratios of a modified magnitude reflectance fit to the original $|\hat{\Gamma}_{mp}(j\omega)|$, shown in Fig. 4.5a for each of the four measurements, as a function of frequency; the frequency axes of the left and right panels in each subplot are vertically aligned. For each sensitivity analysis, the reflectance is modified

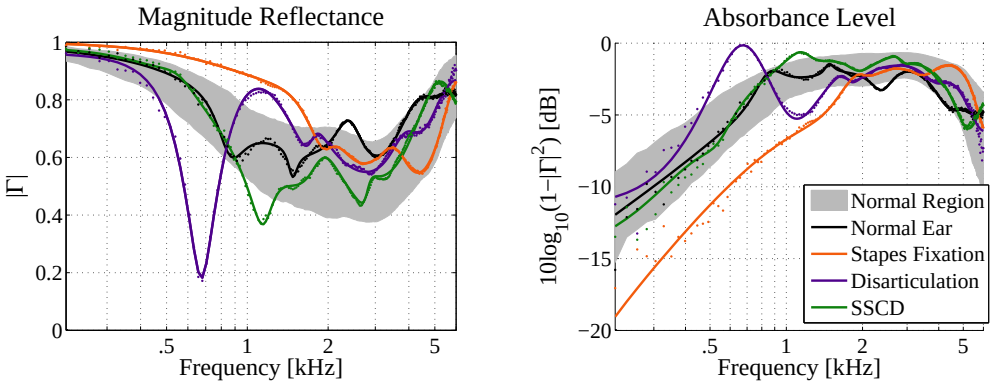

(a) (b)

Figure 4.5: Magnitude reflectance and absorbance level of one normal and three pathological ears. (a) Magnitude reflectance $|\Gamma(j\omega)|$, (b) absorbance level $10\log_{10}(1-|\Gamma(j\omega)|^2)$ [dB]. The gray region shows normative data from the Rosowski et al. [2012] study of normal ears (± 1 standard deviation). The black dots and lines show the raw data and fit for normal ear 22L from Rosowski et al. [2012]. The orange, purple, and green dots and lines show the data and fit for stapes fixation ear 62L, ossicular discontinuity ear 28L, and SSCD ear 52L from Nakajima et al. [2012].

by shifting the color-coded pole, zero, or pole-zero pair of $\hat{\Gamma}_{mp}(s)$ by 10% of its value on the s plane; pole-zero pairs are shifted as a unit about their two-dimensional centers. Sensitivity regions show the minimum and maximum values of the ratio

$$R_\Gamma(\omega) = \frac{|\hat{\Gamma}_{mp}(s+\epsilon(s))|_{s=j\omega}}{|\hat{\Gamma}_{mp}(s)|_{s=j\omega}} \tag{4.2}$$

out of 1000 shifts of the chosen pole, zero, or pair (s_k) by

$$\epsilon(s) = \begin{cases} 0.1\left|\frac{1}{N}\sum_{k=1}^{N} s_k\right| e^{j\Theta} & \text{for } s = s_k \\ 0 & \text{else,} \end{cases} \tag{4.3}$$

where Θ is a random variable uniformly distributed between $-\pi$ and π.

A sensitivity analysis is presented in Fig. 4.6 for a normal ear (Fig. 4.5 black, Fig. 4.6a) from Rosowski et al. [2012] and for three pathological ears from Nakajima et al. [2012]. A representative measurement has been chosen for each pathology examined in that study, including stapes fixation (Fig. 4.5 orange, Fig. 4.6b), ossicular discontinuity (Fig. 4.5 purple, Fig. 4.6c), and SSCD (Fig. 4.5 green, Fig. 4.6d).

4.3.1 Normal Ear

Consider the normal ear measurement shown in Fig. 4.5, ear 22L of the Rosowski et al. [2012] study of normal ears. This fit was performed on reflectance domain data with E forced to zero, achieving a MSE of -35.6 [dB] with 12 poles and 12 zeros. The resulting poles and zeros of $\hat{\Gamma}_{mp}(s)$ are shown in Fig. 4.6a (right). The magnitude reflectance $|\hat{\Gamma}_{mp}(j\omega)| = |\hat{\Gamma}(j\omega)|$ is plotted in Fig. 4.5a (black). Normative data, showing ± 1 standard deviation for 112 measurements of normal ears [Rosowski et al., 2012], is plotted as the shaded gray region in Figs. 4.5a and 4.5b; ear 22L falls within this normal region.

Considering Fig. 4.6a (left), the red shaded region shows a sensitivity analysis of the pole-zero pair labeled a at about 900 [Hz] (close to 1 [kHz]), and the blue region shows a sensitivity analysis of the pole-zero pair labeled b at 2.5 [kHz]. These pole-zero pairs were analyzed because they lie in the mid-frequency region, where normal ears show individually varying minima and maxima of the magnitude reflectance. Note that the frequency axis of the sensitivity plot is aligned with that of the pole-zero plot for comparison. According to Fig. 4.6a (left), the reflectance magnitude is only significantly affected by variations of the pair location in the frequency neighborhood where each pair resides. This indicates that the exact location and curvature of the minima and maxima in those frequency regions are determined by the corresponding pole-zero pairs.

Thus, the individually varying fine-structure minima and maxima in the 1 to 5 [kHz] range [Allen et al., 2005, Rosowski et al., 2012] seem to be characterized primarily by closely-associated pole-zero pairs in that frequency range. Identifying the pole-zero behavior that characterizes the variation of normal ears will allow for better detection of abnormal reflectance measurements. Additionally, the pole-zero pair located close to 1 [kHz] corresponds to the first minimum of $|\hat{\Gamma}(j\omega)|$ and the 'breakpoint' of the power absorbance (Fig. 4.5b), between the low-frequency ramp and the flat region. Based upon the pole-zero fits for this ear, the B&K 4157 (Fig. 3.4b), Voss and Allen [1994] subject #7 (Fig. 4.1b), and Voss et al. [2012] cadaver ear 12R (Fig. 4.2b), it seems that $\hat{\Gamma}_{mp}(s)$ for normal ears will typically have pole-zero pair near 1 [kHz], characterizing the breakpoint of the absorbance level (and the first minimum of the magnitude reflectance).

4.3.2 Stapes Fixation

The orange fit curve and data points in Figs. 4.5a and 4.5b show an example CAR measurement (patient ear 62L, Nakajima et al. [2012]) for a patient with confirmed stapes fixation due to otosclerosis, in the presence of an intact TM and aerated middle ear. The reflectance domain fit has $N_p = 10$, $N_z = 10$, and a MSE of -40.3 [dB]. The absorbance level (Fig. 4.5b) and magnitude reflectance (Fig. 4.5a) for this ear fall significantly outside of the normative regions.

Stapes fixation due to otosclerosis is best characterized by an increased middle ear stiffness [Feeney et al., 2003, Allen et al., 2005, Nakajima et al., 2012]. This typically results in an elevated reflectance magnitude at low frequencies, corresponding to a right shift of the low-frequency sloping region of the absorbance level [Allen et al., 2005]. This behavior is apparent in Fig. 4.5b, where the absorbance level curve for ear 62L is significantly shifted to the right of the normative region below 2 [kHz]. The sensitivity plot in Fig. 4.6b (left) analyzes low frequency singularities, due to the unusual behavior of the magnitude reflectance at low frequencies.

The red region of Fig. 4.6b (left) shows a sensitivity analysis of the pole labeled c on the real axis of $\hat{\Gamma}_{mp}(s)$, closest to the origin. This pole was chosen because it has the least damping, thus the strongest effect on the reflectance, and the magnitude reflectance is higher (has a more pole-like behavior) at low frequencies. The movement of this pole affects the magnitude reflectance at low frequencies up to about 2 [kHz]. Moving this pole towards the origin strengthens its effect, increasing the magnitude reflectance at low frequencies, and moving it away from the origin will decrease the magnitude reflectance at low frequencies. The blue region shows the sensitivity analysis for the pole-zero pair labeled d at about 1.75 [kHz]. This pair was chosen because it is the first pole, zero, or pair occurring in frequency off the σ axis, when we would expect to see a pole-zero pair at about 1 [kHz] for a normal ear. While its largest effect occurs in the frequency neighborhood where the pair resides, movement of this pole-zero pair also affects the magnitude reflectance at low frequencies. This pair appears to characterize the breakpoint of the absorbance level (and perhaps also, in part, its slope) for this pathological ear. For normal ears, this breakpoint occurs significantly lower in frequency, around 1 [kHz], as discussed in Section 4.3.1.

4.3.3 Ossicular Discontinuity

The purple fit curve and data points in Figs. 4.5a and 4.5b show an example CAR measurement (patient ear 28L, Nakajima et al. [2012]) for a patient with confirmed ossicular discontinuity, in the presence of an intact TM and aerated middle ear. The reflectance domain fit has $N_p = 10$, $N_z = 10$, and a MSE of -31.3 [dB]. The absorbance level (Fig. 4.5b) and magnitude reflectance (Fig. 4.5a) for this ear also fall outside the normative regions, but the nature of this variation is quite different from that due to stapes fixation.

Ossicular discontinuity typically causes a narrow-band, tuned resonance in the magnitude reflectance between 0.5 and 0.8 [kHz] [Nakajima et al., 2012]. This is visible in the case of ear 28L, which has a deep notch in the reflectance magnitude at about 700 [Hz] and a corresponding elevated absorbance level in that frequency region. The absorbance level does not have a normal break-point at 1 [kHz]. The poles and zeros of $\hat{\Gamma}_{mp}(s)$ correspondingly show an abnormal behavior in this range. In this case of ossicular discontinuity there are poles and zeros near 1 [kHz], but they are not tightly paired. Hence, the pole and zero closest in frequency to 1 [kHz] are analyzed.

Figure 4.6c (left) shows a sensitivity analysis of the poles and zeros close to 1 [kHz]. The red region indicates that the zero labeled e near 700 [Hz] characterizes the deep notch in the magnitude reflectance. The magnitude reflectance is very sensitive to the location of this zero, experiencing sharp relative dips when it is moved higher or lower in frequency. It makes sense that this zero has a large effect on the magnitude response, because it has a very small σ value compared to the other poles and zeros of $\hat{\Gamma}_{mp}(s)$. The blue region shows the sensitivity of the magnitude reflectance to the pole labeled f at 1 [kHz]. Not only does this pole affect the magnitude reflectance in the 1 [kHz] region (where the magnitude reflectance is higher than average), but it has a significant effect on the magnitude reflectance for all frequencies below 2 [kHz].

4.3.4 Superior Semicircular Canal Dehiscence (SSCD)

The green fit curve and data points in Figs. 4.5a and 4.5b show an example CAR measurement (patient ear 52L, Nakajima et al. [2012]) for a patient with confirmed SSCD, in the presence of an intact TM and aerated middle

ear. The reflectance domain fit has $N_p = 12$, $N_z = 12$, and a MSE of -34.3 [dB]. The absorbance level (Fig. 4.5b) and magnitude reflectance (Fig. 4.5a) for this ear fall slightly outside of the normative regions around 1 [kHz].

SSCD typically shows a similar variation from normal to that caused by ossicular discontinuity, though not as extreme [Nakajima et al., 2012]. In Fig. 4.5a there is an abnormally deep minimum in the magnitude reflectance at 1 [kHz], corresponding to a slight elevation of the absorbance level at that frequency (Fig. 4.5b), relative to the normal middle ear region. Comparing this with the purple curve for ossicular discontinuity, the effect is similar but not as pronounced, and the notch occurs in a slightly higher frequency range. Because the variation in the magnitude reflectance is observed at low frequencies around 1 [kHz], the sensitivity of poles and zeros in that region is analyzed.

Figure 4.6d (left) shows the sensitivity analysis for the pole-zero pairs at 500 [Hz] and 1 [kHz] in Fig. 4.6d (right). The red region of Fig. 4.6d (left) shows the effect of the pole-zero pair labeled g at 500 [Hz] on the magnitude reflectance. This pair was selected because it lies between the σ axis and the normal 1 [kHz] pair location. Shifting this pole-zero pair causes a variation in the reflectance magnitude around that frequency. However, the effect is not very pronounced; the pole and zero are very close together, and appear to be fitting a small noise peak. In fact, this effect is so small compared to the effect of the 1 [kHz] pole-zero pair, that the red region is hard to see. The blue region shows that shifting the pole-zero pair h at 1 [kHz] causes large variations of the magnitude reflectance in that frequency neighborhood. Notice that the zero of this pair has a significantly smaller σ value than the pole, increasing its relative effect on the reflectance. This zero and its distance from the pole affect the depth of the minimum in the magnitude reflectance at 1 [kHz]. This pole-zero pair also characterizes the nature of the breakpoint in the absorbance level between the initial slope and the flat region. Considering the pole-zero pairs near 1 [kHz] found for normal ears in this paper (Figs. 3.4b, 4.1b, 4.2b and 4.6a (right)), the abnormal depth of the 1 [kHz] notch in the SSCD magnitude reflectance could be due to nuances of the location of its 1 [kHz] pair, such as damping and relative distance between the pole and zero.

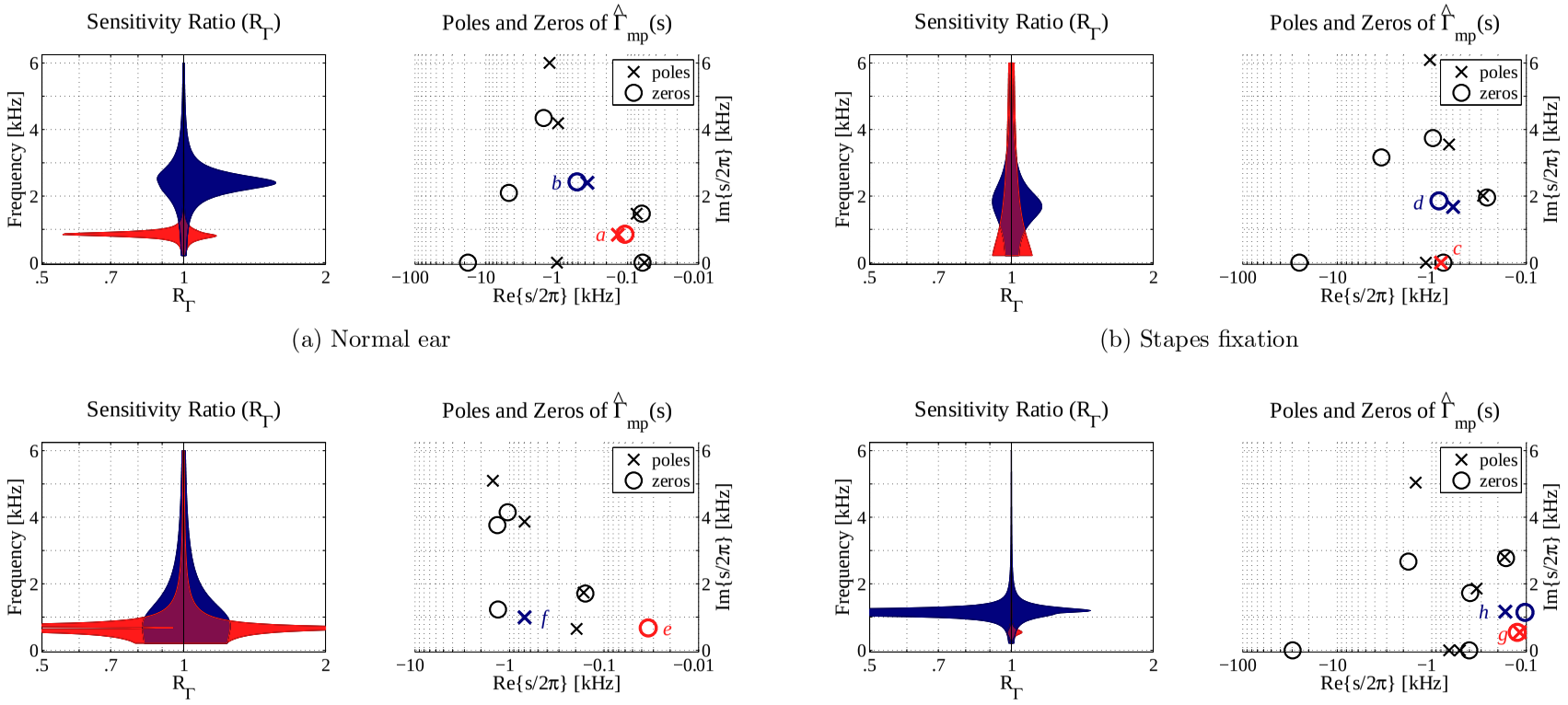

(a) Normal ear

(b) Stapes fixation

(c) Disarticulation

(d) SSCD

Figure 4.6: Sensitivity analysis of select poles and zeros for the ears of Fig. 4.5. Each subplot shows the pole-zero plot of $\hat{\Gamma}_{mp}(s)$ (right), and two color-coded sensitivity analyses corresponding to the highlighted poles and zeros (left); the frequency axes are vertically aligned for each pair of plots. (a) Normal ear, (b) stapes fixation, (c) ossicular discontinuity, (d) SSCD. Each sensitivity analysis shows the minimum and maximum values of R_Γ (Eq. 4.2) across frequency for the corresponding colored pole, zero, or pole-zero pair.

CHAPTER 5

RESULTS FOR NORMAL AND PATHOLOGICAL DATA SETS

Characteristics of pole-zero fits to larger sets of normal and pathological CAR data were studied in order to determine features that might be useful for classification and modeling. Normal middle ear CAR measurements were drawn from Voss and Allen [1994], while pathological measurements for ears with stapes fixation, ossicular discontinuity, and SSCD were drawn from Nakajima et al. [2012]. Each of these data sets is analyzed in its entirety, in order to examine patterns across pole-zero fits to measurements of middle ears in similar conditions.

5.1 Normal Ears

Recall from Section 2.3 that the magnitude reflectance of normal middle ears is close to one at low frequencies, has a broad minimum from about 1 to 4 [kHz], then rises again at high frequencies. The absorbance level has a corresponding rising slope below 1 [kHz], a relatively flat region between 1 and 4 [kHz], and a roll-off at high frequencies. Normal ears typically have individually varying fine-structure minima and maxima in the 1 to 4 [kHz] range of the magnitude reflectance [Rosowski et al., 2012]; this variation corresponds to a small decibel range of the absorbance level [Allen et al., 2005]. In Section 4.3.1, it was observed that the normal ear measurements (N=3 human ears) on which we performed pole-zero fits tended to have a pole-zero pair in the reflectance fit $\hat{\Gamma}_{mp}(s)$ at about 1 [kHz], as did the pole-zero fit of the B&K 4157 middle ear simulator. This corresponds in frequency to the typical location of the first minimum of the magnitude reflectance, or the breakpoint between the low-frequency slope and flat region of the absorbance level. The normal ear measurements also had other closely-placed pole-zero pairs between 1 and 4 [kHz], though the B&K 4157 simulator

did not. Here the entire data set from the Voss and Allen [1994] study is examined.

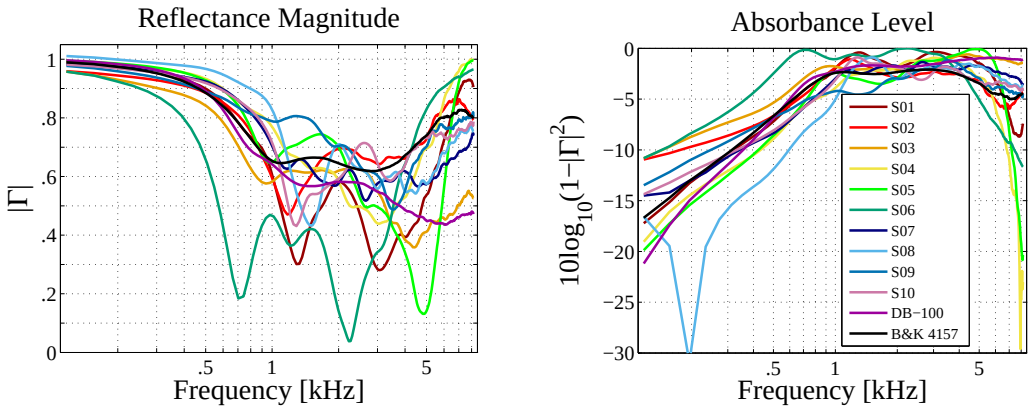

(a) (b)

Figure 5.1: Reflectance summary for the ten human ears and two ear simulators (the B&K 4157 and the DB-100, shown in Fig. 3.1) from Voss and Allen [1994]. (a) Reflectance magnitude, (b) absorbance level [dB]. Pole-zero fits for these ears are shown in Fig. 5.2.

Figure 5.1 shows a reflectance summary for ten human ears and two ear simulators (the B&K 4157 and the DB-100, shown in Fig. 3.1) from Voss and Allen [1994]. Again, it is clear in Fig. 5.1a that magnitude reflectance of normal middle ears has individually varying minima and maxima in the 1 to 4 [kHz] (mid-frequency) range, while this region is much smoother for artificial ears; this is because the ear simulators are each designed to represent an average normal ear. The corresponding absorbance for these ten normal ears and two simulators is plotted in Fig. 5.1b; considering the absorbance, the individual variation of normal ears in the 1 to 4 [kHz] range is condensed to a < 5 [dB] range.

Figure 5.2 shows pole-zero plots of $\hat{\Gamma}_{mp}(s)$ (the approximate reflectance at the eardrum) for the DB-100 and B&K 4157 coupler and for the ten Voss and Allen [1994] normal ears shown in Fig. 5.1. Considering the pole-zero plots of $\hat{\Gamma}_{mp}(s)$ for the ear simulators (lower right side of Fig. 5.2), the simulators both have poles and zeros on the real axis, a pole-zero pair at about 1 [kHz] corresponding to the first minimum of the magnitude reflectance (and the breakpoint of the absorbance), and another, more widely-spaced pair fitting the high-frequency behavior of the response. The magnitude reflectance of the B&K 4157 shows a distinct minimum at 1 [kHz], while that of the DB-100

has a slight bend below 1 [kHz] and a minimum between 1 and 2 [kHz]. The pole-zero plots reflect this difference, as the pole and zero of the B&K 4157 near 1 [kHz] appear at approximately the same $\omega/(2\pi)$ frequency value, while the pole-zero pair near 1 [kHz] for the DB-100 is slightly offset in frequency.

Examining the pole-zero plots of $\hat{\Gamma}_{mp}(s)$ shown in Fig. 5.2 for ten CAR measurements of normal ears, many ears (1, 2, 3, 5, 7, 9 10) show a pole-zero pair near 1 [kHz], where the pole and zero are very close in frequency ($\omega/(2\pi)$). For ears 6 and 8, there is pole zero activity near 1 [kHz], though there are not distinct pairs aligned in frequency; this sort of behavior better resembles the frequency-offset 1 [kHz] pair of the DB-100 than the frequency-aligned 1 [kHz] pair of the B&K 4157. Ear 4 has a downward sloping magnitude reflectance with small bends in it from 1 to 3 [kHz], with no defined minimum near 1 [kHz], thus it seems to have no distinct pole-zero pair near 1 [kHz].

Unlike the ear simulators, the normal ears also have many poles and zeros in the mid-frequency range, from about 1 to 4 [kHz] (or higher). All ears have at least one closely-placed pole zero pair between 1 and 5 [kHz]. Subjects 1, 2, 3, 7, 9, and 10 have particularly cleanly paired poles and zeros, corresponding to fine-structure minima and maxima of the reflectance magnitude. If a pair is almost completely overlapping, it typically corresponds to a very small minimum or maximum, often a noise peak. Widely-spaced pairs tend to fit larger minima and maxima.

For the eventual goal of automated detection and classification of pathologies, it is important to understand the effect of the individual variation of normal ears on pole-zero fits to CAR measurements. Considering these measurements, it appears that the presence of a pole-zero pair near 1 [kHz] is typical of normal ears; its absence or drastic change in frequency location might be an indication of a middle ear pathology. However, these subjects have a lot of variation of pole-zero locations in the mid-frequency region, which is not due to middle ear pathology. More data must be analyzed in order to thoroughly identify this region and the constraints on poles and zeros within it (e.g. the distance between poles and zeros), but if variation in this region can be isolated and identified as 'normal' it will enable better detection of variations due to true middle ear pathologies.

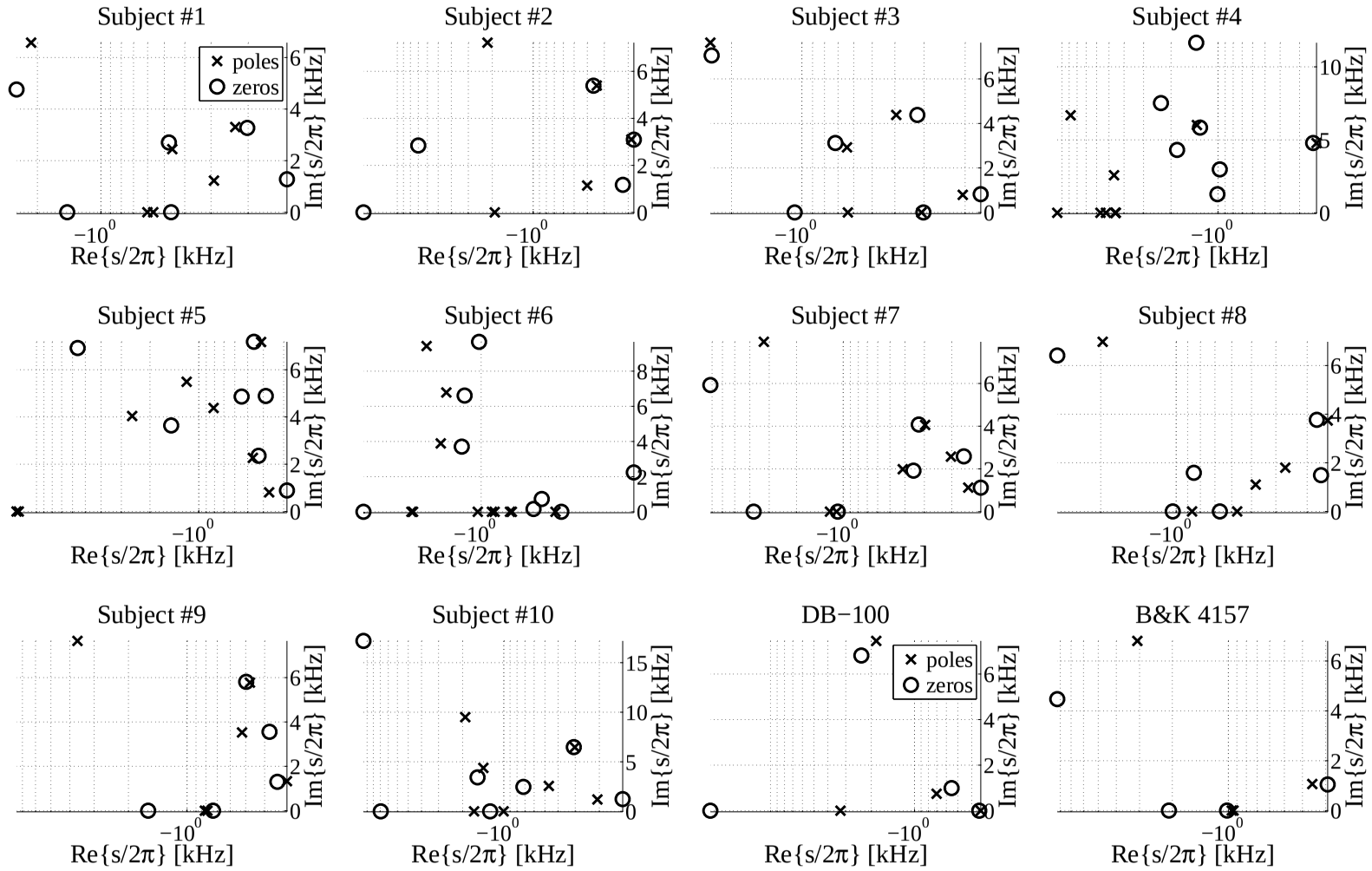

Figure 5.2: Pole-zero plots of $\hat{\Gamma}_{mp}(s)$ for ten normal ear measurements and two ear simulators from Voss and Allen [1994] shown in Fig. 5.1. Most fits have a pole-zero pair located near $\omega/(2\pi) = 1$ [kHz], and other closely-placed pairs between 1 and 4 [kHz] (corresponding to fine-structure minima and maxima of the magnitude reflectance in that region). Simulator fits have a pole-zero pair located near $\omega/(2\pi) = 1$ [kHz], and no other pairs between 1 and 4 [kHz], because the reflectance for each simulator is fairly smooth in that region.

5.2 Stapes Fixation

As previously stated, stapes fixation due to otosclerosis is characterized by an increased middle ear stiffness at low frequencies due to the ossification of the stapes bone; this results in an elevated reflectance magnitude at low frequencies. A simple model of this stiffness is presented here, and ears with stapes fixation are compared to normal middle ears.

Consider the estimated eardrum impedance $\hat{Z}_{TM}(s)$ (Eq. 3.11). At low frequencies, the impedance will be stiffness dominated according to

$$Z_{TM} \sim \frac{1}{sC}, \tag{5.1}$$

where C is the *compliance*, which is inversely proportional to the stiffness (as discussed in Section 2.3). In this expression, there is a pole at $s = 0$, with a residue equal to $1/C$. In the pole-zero fits, there is typically not a pole of $\hat{Z}_{TM}(s)$ exactly at $s = 0$; rather, a pole will appear very close to $s = 0$ on the real axis. For each fit we may estimate the low-frequency compliance C of Z_{TM} by taking the inverse of the residue corresponding to the pole of $\hat{Z}_{TM}(s)$ that lies closest to $s = 0$.

Figure 5.3a shows the absorbance level for 13 ears with stapes fixation due to otosclerosis from Nakajima et al. [2012], in comparison with the normative distribution from Rosowski et al. [2012]. In general, stapes fixation causes a right shift of the low frequency ramp and breakpoint of the absorbance level due to the increased stiffness of the middle ear system, as discussed in Section 4.3.2. However, the effect is not as pronounced for all stapes fixation ears as it is for ear 62L, shown in Figs. 4.5 and 4.6b. In fact, roughly half of the ears with stapes fixation seem to fall within the normal range, or just outside of 1 standard deviation.

Figure 5.3b shows a histogram of $\log_{10}(C)$ values, where C is the compliance from Eq. 5.1, estimated for 54 normal ears from Rosowski et al. [2012] and for the 13 ears with stapes fixation from Nakajima et al. [2012]. There were 14 ears in the original study, but one ear was missing from the data we received. Considering Fig. 5.3, the majority of the ears with stapes fixation lie on the far left side of the distribution, meaning that they have the smallest compliance values (greatest stiffness), as might be expected for this pathology.

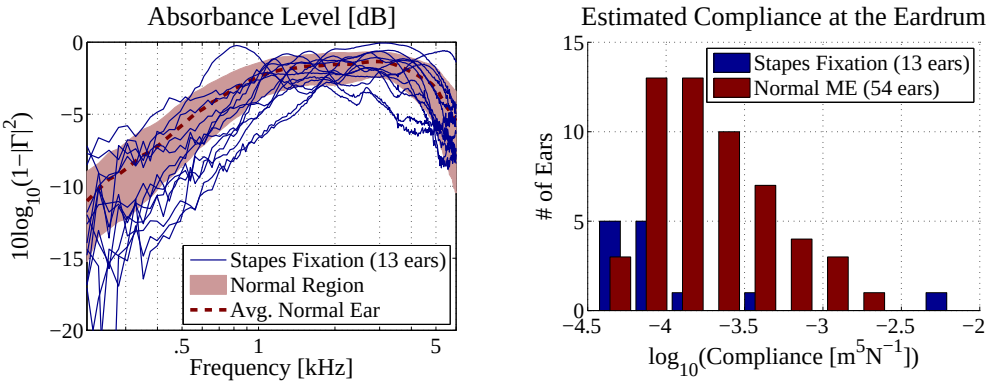

(a) (b)

Figure 5.3: Comparison of 54 normal ears [Rosowski et al., 2012] and 13 ears with stapes fixation due to otosclerosis [Nakajima et al., 2012]. (a) Absorbance level, (b) histogram of the base-10 logarithm of the estimated compliance C (Eq. 5.1) at the eardrum (bin width = 0.23). The ears with stapes fixation are generally less compliant (stiffer) than normal ears.

This result, based on physical intuition and modeling, indicates that this compliance parameter of the pole-zero fit may vary systematically from normal in the presence of stapes fixation due to otosclerosis, and may be used for modeling and detecting this pathology. Though the distributions in Fig. 5.3 overlap, meaning that the compliance parameter may not necessarily be used for a standalone diagnosis, it might be used in combination with other measurements in order to detect stapes fixation. Considering that many of the ears with stapes fixation fall in or near the normal region of the low frequency ramp of the absorbance in Fig. 5.3a, it is not surprising the perfect separation of the distributions is not achieved when modeling the low frequency compliance of the impedance.

For reference, a complete acoustic summary and pole-zero fit is shown for each of the 13 ears with stapes fixation in Appendix B (Figs. B.1 through B.13). Some useful parameters associated with these fits, such as the residual canal length estimate $\hat{L}$, are given in Table B.1. In some cases, as observed in Section 4.3.2, the breakpoint of the absorbance level occurs at an abnormally high frequency, and is characterized by an upward shift in frequency of the first pole-zero pair of $\hat{\Gamma}_{mp}(s)$ (which would typically be seen at about 1 [kHz] for normal ears).

5.3 Ossicular Discontinuity

As discussed in Section 4.3.3, discontinuity of the ossicular chain causes a narrow, low frequency resonance in the magnitude reflectance, corresponding to an abnormal peak of the absorbance level. For the six ears with ossicular discontinuity from Nakajima et al. [2012], this resonance typically occurs between about 0.5 and 0.8 [kHz]. Figures 5.4 and 5.5 show the absorbance level and the minimum-phase factor $\hat{\Gamma}_{mp}(s)$ for pole-zero fits to each of the six ears with ossicular discontinuity.

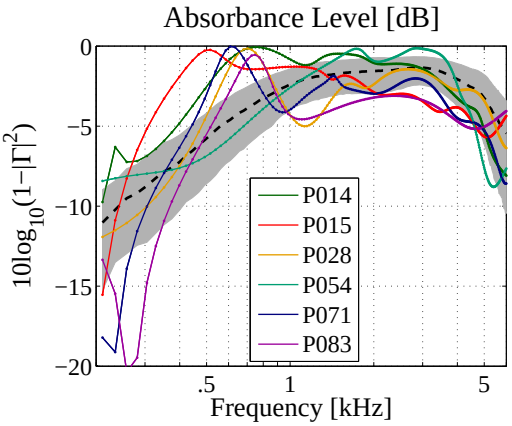

Figure 5.4: Absorbance level [dB] of six pole-zero fits to ears with ossicular discontinuity, compared to normative data from Rosowski et al. [2012].

Considering the absorbance level (Fig. 5.4) for each of the fits, five out of 6 ears show an abnormal peak of the absorbance level below 1 [kHz], as compared to the normative data from Rosowski et al. [2012]. Consequently, these ears do not show the typical 'breakpoint' behavior between the low frequency slope and mid frequency flat region of the absorbance level. The only ear that does not share this behavior is ear 54R. For this ear, the breakpoint occurs at a slightly higher frequency than normal, similar to the absorbance level of the ears with stapes fixation. This indicates that ear 54R is stiffer than normal; this condition interacts with the ossicular discontinuity, making the CAR more difficult to interpret. Little study has been conducted regarding ears with multiple pathologies; however, intuitively, interfering conditions may confound detection of middle ear pathologies.

Figure 5.5 shows the pole-zero fits $\hat{\Gamma}_{mp}(s)$ that produce the curves shown in Fig. 5.4. Five out of the six fits have a zero with small damping ($\sigma/(2\pi)$) between 0.5 and 0.8 [kHz] ($\omega/(2\pi)$), characterizing the low frequency reso-

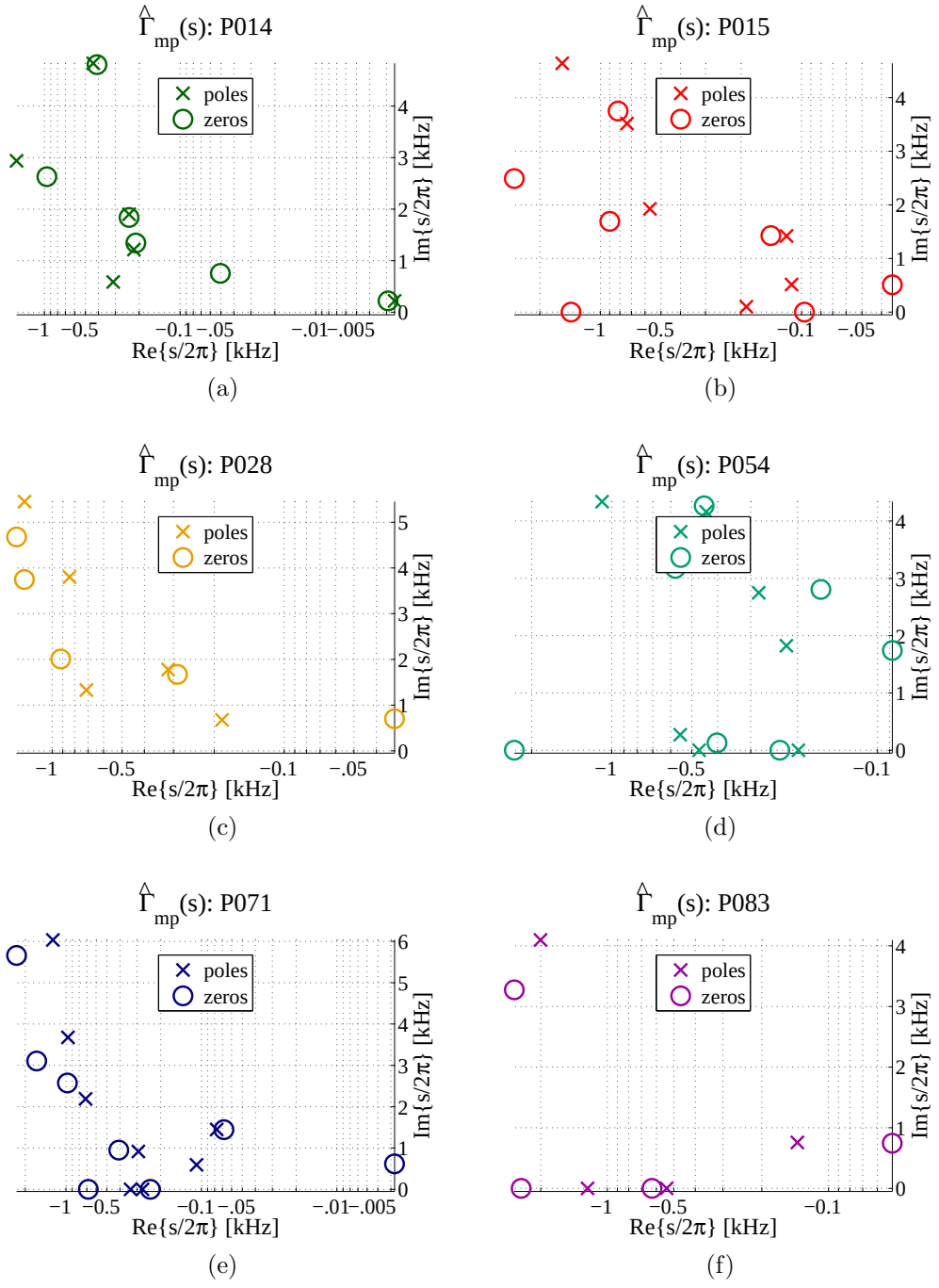

Figure 5.5: Pole-zero fits $\hat{\Gamma}_{mp}(s)$ that produce the curves shown in Fig. 5.4. Five out of six fits have a zero with relatively small damping ($\sigma/(2\pi)$) between 0.5 and 0.8 [kHz] ($\omega/(2\pi)$), characterizing the low frequency resonance due to ossicular discontinuity. Ear 54R (d) does not have such a zero, as the absorbance level for this ear has no peak below 2 [kHz].

nance due to ossicular discontinuity. For ears 15L, 28L, 71L and 83L, the zero characterizing the low frequency resonance has the smallest damping out of all poles and zeros of $\hat{\Gamma}_{mp}(s)$. It appears that the relative damping of that zero, compared to the other poles and zeros of the fit, may partially characterize the width and depth of the resonance. For instance, the zero feature of ear 71L has an order of magnitude less damping than all other poles and zeros in that fit. Correspondingly, the curve for P071 in Fig. 5.4 seems to have a higher and narrower maximum due to the discontinuity that the other ears. Note that for ear 14L (Fig. 5.5a), there is a pole-zero pair closer to the ω axis. However, this pole and zero are nearly overlapping, and appear to fit the noise peak in the absorbance level for ear 14L at about 0.2 [kHz]. Ignoring this pair, ear 14L has a similar low frequency zero to the other four ears. Ear 54R (Fig. 5.5d) does not have such a zero, as the absorbance level has no peak below 2 [kHz].

For reference, a complete acoustic summary and pole-zero fit is shown for each of the six ears with ossicular discontinuity in Appendix B (Figs. B.14 through B.19). Some useful parameters associated with these fits, such as the residual canal length estimate $\hat{L}$, are given in Table B.1. Note that the impedance magnitude of each ear also shows a low frequency resonance due to the discontinuity, similar to the reflectance magnitude.

5.4 Superior Semicircular Canal Dehiscence (SSCD)

For completeness in showing the pole-zero fits to data from Nakajima et al. [2012], an acoustic summary and pole-zero fit is shown for each of the nine ears with SSCD in Appendix B (Figs. B.20 through B.28). Some useful parameters associated with these fits, such as the residual canal length estimate $\hat{L}$, are given in Table B.1.

An extensive analysis of these ears was not performed for this thesis. The CAR results obtained by Nakajima et al. [2012] indicated that the systematic changes to the CAR for SSCD are more subtle than those for stapes fixation and ossicular discontinuity. This makes sense, as the physiological changes due to SSCD occur a later stage in the ear system (as viewed from the probe). SSCD is characterized by an abnormally deep notch in the magnitude reflectance at 1 [kHz] (Section 4.3.4). For ears 18L (Fig. B.20), 44L

(Fig. B.21), 52L (Fig. B.22), 82L (Fig. B.25) and 103R (Fig. B.27), it seems that the abnormally deep notch at 1 [kHz] may be at least partially characterized by the spacing of the pole-zero pair of $\hat{\Gamma}_{mp}(s)$ near 1 [kHz] (the distance between the pole and the zero).

CHAPTER 6

BACTERIAL BIOFILM STUDY

Children with chronic OM often have conductive hearing loss which results in communication difficulties and requires surgical treatment. Recent studies [Nguyen et al., 2010, 2012] have provided clinical evidence that there is a one-to-one correspondence between chronic OM and the presence of a bacterial biofilm behind the TM. In a recent collaboration with Dr. Cac Nguyen, the acoustic effects of bacterial biofilms, confirmed using *optical coherence tomography* (OCT), were investigated in five adult ears. Non-invasive OCT images were collected by Dr. Nguyen to visualize the cross-sectional structure of the middle ear, verifying the presence of a biofilm behind the TM. Wideband measurements of acoustic reflectance and impedance (0.2 to 6 [kHz]) were then used to study the acoustic properties of ears with confirmed bacterial biofilms. Compared to known acoustic properties of normal middle ears, each of the ears with a bacterial biofilm has an elevated power reflectance in the 1 to 3 [kHz] range, corresponding to an abnormally small resistance (real part of the impedance). The reflectance properties of ears with bacterial biofilms are examined in this chapter, followed by a pole-zero analysis of the biofilm data.

This research was conducted under a protocol approved by the Institutional Review Boards of the University of Illinois at Urbana-Champaign and Carle Foundation Hospital (Urbana, IL). All subjects were adults ($>$ 25 years old), and biofilm candidates had a history of chronic OM or were diagnosed with fluid via otoscopy. Normal ears (volunteers) and pathological ears (clinical patients) were assessed according to the OCT result and otoscopic examination. Reflectance measurements were also made for all ears using the MEPA/HearID system (Mimosa Acoustics). Two of the five OCT-confirmed biofilm ears (B2 and B3) appeared to have fluid present during the otoscopic examination, which was performed during the same visit as the reflectance and OCT measurements. Reflectance measurements were

collected in a busy clinical environment (working in a sound booth was not practical), resulting in low-frequency measurement noise. Data is presented for one OCT-confirmed normal and five OCT-confirmed biofilm ears. Normative reflectance data is drawn from Rosowski et al. [2012], as in Section 2.3.

6.1 Bacterial Biofilms

Bacterial biofilms have been considered to be the cause of many chronic infectious diseases [Dohar et al., 2009, Parsek and Singh, 2003, Macassey and Dawes, 2008, Costerton et al., 1999]. Biofilms have been linked to chronic OM and OM with effusion in the middle ear. Biofilms are complex, colonized bacterial structures. This biopolymer structure often has the consistency of glue, and the protected bacteria within a biofilm become inherently resistant to most conventional antibiotics, due to the mechanical protection of the film, resulting in reinfection and treatment complications for chronic OM cases [Aparna and Yadav, 2008].

The impact of a bacterial biofilm on the acoustic characteristics of the middle ear had not been previously studied. Intuitively, the presence of a bacterial biofilm on the surface of the TM affects the motion of the TM, where acoustic pressure waves in the ear canal are transduced to mechanical waves of the ossicular chain. Further, bacterial biofilms may have different thicknesses and cover different areas of the TM, which may cause the acoustic effects to vary greatly across different biofilm cases. It is therefore necessary to further investigate the acoustic impact of bacterial biofilms.

6.2 Biofilm Detection with Optical Coherence Tomography

Detection and imaging of middle ear biofilms was performed using a custom-built OCT-otoscopy system with a hand-held probe designed for clinical use [Jung et al., 2011, Nguyen et al., 2012]. Currently, OCT is the only imaging technique which can acquire *in vivo*, non-invasive images of the middle ear structure [Nguyen et al., 2010, 2012]. The human TM is approximately 100

[μm] thick, while the thickness of a biofilm varies in the range of tens to hundreds of micrometers [Lim, 1995, Xi et al., 2006]. These micro-features of the middle ear are not resolvable by more traditional medical imaging techniques such as CT, MRI, and ultrasound, even with state-of-the-art high-resolution methods. To perform OCT, low-coherence light is generated from a broadband optical source and split by a beam splitter or fiber-optic coupler into two beams that are sent to sample and reference arms of the interferometer. The reference arm contains a stationary mirror, while the sample arm contains beam-delivery optics directed toward the sample. The interference of the two back-reflected or scattered beams is captured by a linear photodetector array and processed by a computer to describe the depth-resolved optical scattering properties of the tissue. The broadband, near-infrared light allows axial resolutions of up to 2 to 3 [μm] and penetration depths of up to 2 to 3 [mm] in highly-scattering tissues. The interference of scattered light from the tissues and reflected light from a mirror provides structural, depth-resolved information about the tissues, in the form of two-dimensional cross-sectional images or three-dimensional volumes.

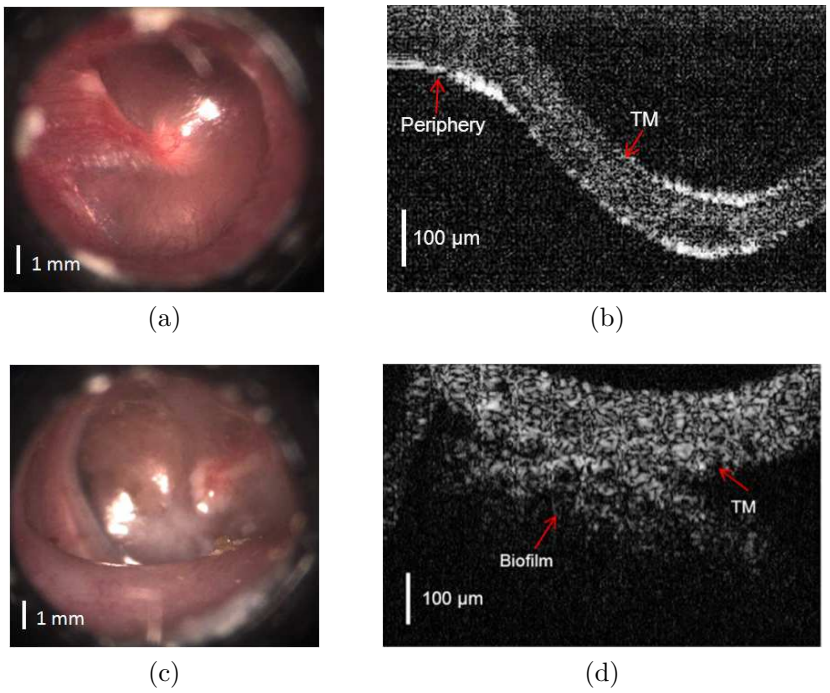

Figure 6.1: Otoscope and OCT images for a normal ear (N1) and an ear with OCT-confirmed bacterial biofilm (B1). (a) Otoscope picture of ear N1, (b) OCT image of ear N1 (perpendicular to the plane of the TM, shown in (a)), (c) otoscope picture of ear B1, (d) OCT image of ear B1.

Figure 6.1 shows otoscope and OCT images for a normal ear (Figs. 6.1a and 6.1b) and an ear with bacterial biofilm (Figs. 6.1c and 6.1d). The TM of a normal human ear appears translucent to opaque under video otoscopy. Figure 6.1a shows an image of the healthy TM captured via video otoscopy. Considering the OCT scan (Fig. 6.1b), the normal TM is readily identified by two sharp edges, about 90 [μm] apart, which is consistent with the average thickness of the human eardrum (about 100 [μm]). As expected from this image, the TM is classified as normal via the algorithm described in Nguyen et al. [2010] and Nguyen et al. [2012]. Note that the thickness of the TM varies with spatial location. TM regions near the periphery are significantly thicker than regions closer to the umbo.

In the case of chronic OM, the appearance of the TM under video otoscopy may differ between patients (e.g. red, cloudy, or retracted). The ear with a biofilm, which has a cloudy TM, is shown in Fig. 6.1c. Using OCT, various biofilm structures have been observed in patient ears [Nguyen et al., 2012]. These biofilms can appear with different thicknesses, scattering levels, and have either partial or complete presence within the cross-sectional scans. In the OCT image (Fig. 6.1d), the bacterial biofilm and TM structures are indicated. This biofilm is about 130 [μm] thick at the scan location, and is attached to the inner surface of the TM. Thus the thickness of this biofilm at the imaging location was 30% greater than that of the normal TM. Such a thickening is consistent with predictions of the characteristic impedance of the TM as a function of radius from the umbo [Parent and Allen, 2010].

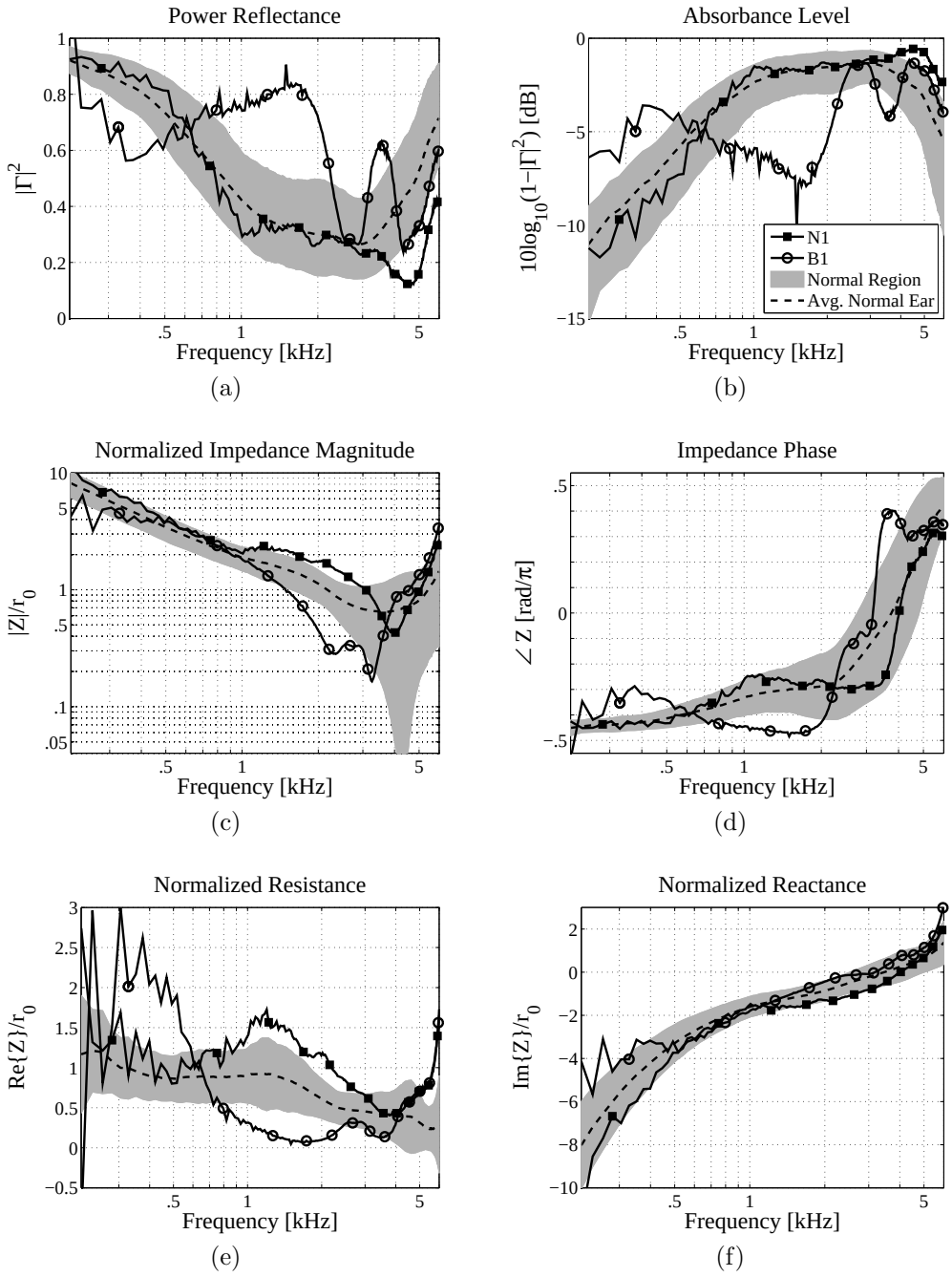

Figure 6.2: Acoustic comparison of normal ear N1 and OCT-confirmed biofilm ear B1. (a) Normalized impedance magnitude, (b) impedance phase, (c) normalized resistance, (d) normalized reactance. The dotted black lines and gray regions show the average normal ear ± 1 standard deviation from Rosowski et al. [2012]. The main marker of a biofilm is the near-zero resistance between 1 and 2 [kHz], corresponding to an impedance phase close to $-\pi/2$ (consistent with a purely imaginary impedance).

6.3 Acoustic Properties of Biofilm Ears

Figure 6.2 shows an acoustic comparison of an OCT-confirmed biofilm ear (B1) with an OCT-confirmed normal ear (N1). For these plots, the light gray regions show ±1 standard deviation about the mean for 112 measurements of 56 normal ears from Rosowski et al. [2012]. Black dotted lines show the normative means based on that study. Considering the power reflectance (Fig. 6.2a) and absorbance level (Fig. 6.2b), ear N1 falls well within the normal region up to about 4 [kHz]. Assuming the absorbance is an approximation to the middle ear transfer function, this ear actually performs better than normal above 4 [kHz]. Considering the same plots, ear B1 (the ear with biofilm) falls well outside of the normal range. Most notably, the power reflectance has an abnormal maximum with a peak of 0.8 (80% reflected power) at 1.7 [kHz], causing the power reflectance to be much higher than normal between 1 and 2 [kHz]. The unusual maximum at 1.7 [kHz] causes a 'reverse slope' appearance, as the power reflectance curve between 0.4 and 1 [kHz] is approximately perpendicular to the normal mean curve. Considering the absorbance level, the abnormal maximum in the power reflectance corresponds to a minimum of the absorbance level at 1.7 [kHz], about 6 [dB] below the mean normal absorbance level. Considering that the ±1 standard deviation region is about 2 [dB] wide at this frequency, this seems to be a severe effect.

In order to further analyze the acoustic effects of this bacterial biofilm, the acoustic impedance (related to the reflectance via Eq. 2.3) of the biofilm ear (B1) is compared to that of the normal ear (N1) in Figs. 6.2c through 6.2f. Consider the acoustic impedance measurements of normal ear N1 and biofilm ear B1 near 1.7 [kHz], where the power reflectance shows the greatest abnormalities for the biofilm ear. In Fig. 6.2e, normal ear N1 has a normalized resistance that is slightly higher than normal near 1.7 [kHz], while the biofilm ear B1 has a normalized resistance that is much lower than normal, approaching zero. Because the middle ear is a passive system, the resistance must be greater than zero. Thus, the resistance of the biofilm ear approaches this fundamental limit, making its deviation from normal noteworthy. Thus, at 1.7 [kHz], the impedance of the biofilm ear becomes almost purely reactive. This is apparent in the impedance phase of ear B1 as well, which approaches $-\pi/2$ at this frequency (a pure compliance). As the impedance becomes purely reactive, the reflectance magnitude must approach 1, thus

the minimum of the resistance corresponds to a maximum of the power reflectance at 1.7 [kHz]. One possible physical interpretation of this data is that at 1.7 [kHz] the bacterial biofilm causes the TM to behave as a rigid surface; thus, the middle ear is effectively blocked and the impedance becomes that of an approximately lossless (purely reactive) cavity. Further experimental evidence will be required to confirm this conjecture.

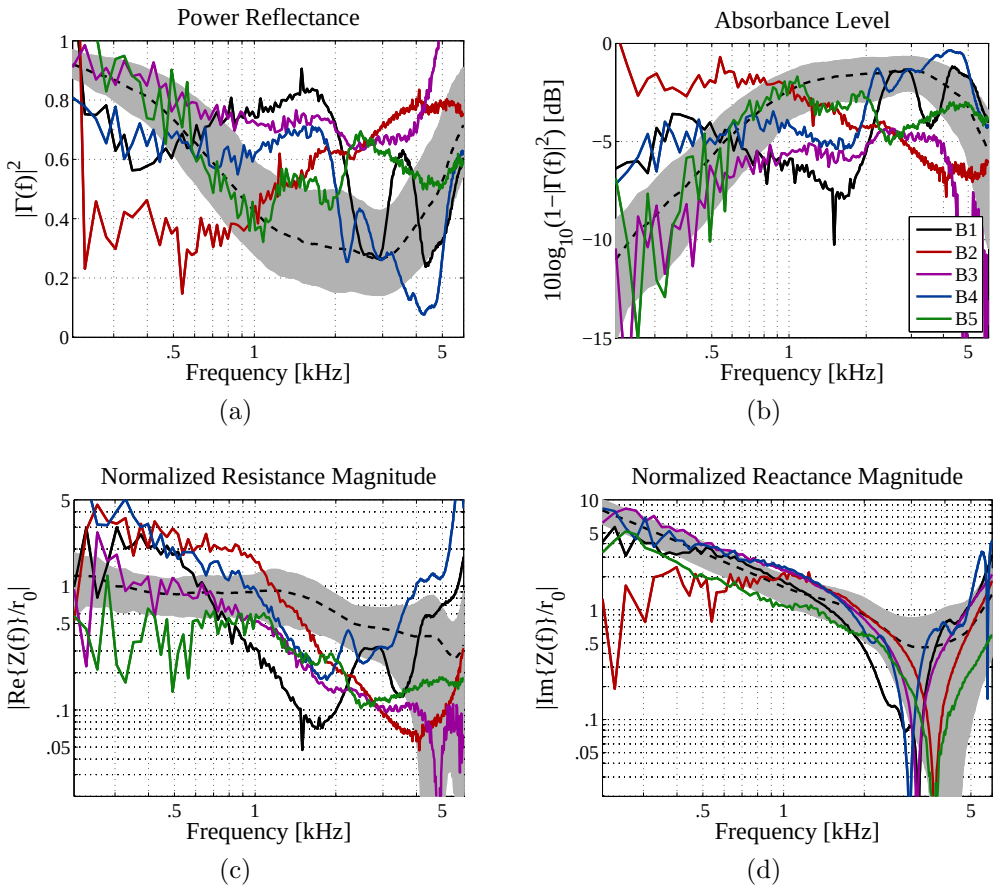

Figure 6.3: Five ears with OCT-confirmed biofilms. (a) Power reflectance, (b) absorbance level [dB], (c) normalized resistance magnitude, (d) normalized reactance magnitude. The dotted black lines and gray regions show the average normal ear ±1 standard deviation from Rosowski et al. [2012]. Note that ears B2 and B3 were also diagnosed with OM during the otoscopic examination. All five biofilm ears show a depressed resistance between 1 and 3 [kHz], even though ear B5 appears close to normal when considering the power reflectance, and ears B2 and B3 have different high-frequency properties (presumably related to OM).

Figure 6.3 shows an acoustic summary of all five ears with confirmed biofilms. Ignoring low-frequency abberations, which in part are due to noise,

the power reflectance (Fig. 6.3a) is higher than normal, and the absorbance level (Fig. 6.3b) is lower than normal, for all ears within the 1 to 3 [kHz] range. Abnormal maxima in this range result in the 'reverse slope' behavior of the power reflectance in the 0.5 to 2 [kHz] range. While the power reflectance and absorbance levels for ears B1, B4 and B5 return approximately to normal at higher frequencies, the two ears that were diagnosed with fluid as well, B2 and B3, also show an elevated power reflectance (a depressed absorbance level) above 3 [kHz]. This is consistent with previous studies of reflectance for middle ears with effusion [Feeney et al., 2003, Allen et al., 2005, Ellison et al., 2012].

Figures 6.3c and 6.3d show the normalized acoustic resistance and reactance; unlike Figs. 6.2e and 6.2f, these figures show magnitude quantities plotted on a log-log scale. Note that normalized reactance magnitude is similar to the normalized impedance magnitude (Fig. 6.2c), because the normalized resistance magnitude is comparatively small for most frequencies. Considering Fig. 6.3d, like ear B1, the other biofilm ears have reactance measurements that lie approximately within the normal region, with slight deviations at low frequencies, which are most likely related to measurement noise (Fig. 6.3d). Considering Fig. 6.3c, the effect of a biofilm on the normalized acoustic resistance appears to be consistent. All five biofilm ears have an abnormally low normalized resistance in the 1 to 3 [kHz] range, corresponding to the abnormally high power reflectance.

Figure 6.4 shows the distributions of the normalized resistance for normal ears and for ears with OCT-confirmed bacterial biofilms. The light gray region shows ± 1 standard deviation for the Rosowski et al. [2012] normal ears, the dark gray region shows ± 1 standard deviation for the biofilm ears from this study, and the dotted lines show the means of both distributions. The normalized resistance of the biofilm ears has a large standard deviation at low frequencies due to measurement noise. However, there is a clear separation of the distributions between about 1 and 3 [kHz], particularly just below 2 [kHz]. This indicates that considering the normalized acoustic resistance in this frequency region may aid in the detection of biofilms using acoustic measurements.

Variations across measurements of the ears with biofilms presented in this study have two primary sources: some of the ears have interacting pathologies (e.g. a biofilm and fluid), and biofilms may coat different areas of the

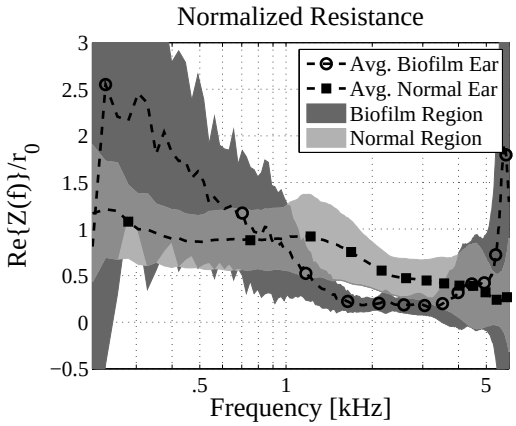

Figure 6.4: The dotted black lines show the average normal ear from Rosowski et al. [2012] and the average biofilm ear from this study; the light gray region shows ±1 standard deviation for normal ears, and the dark gray region shows ±1 standard deviation for biofilm ears. Just below 2 [kHz], these regions do not overlap, indicating that a depressed resistance near 2 [kHz] may be a useful feature for detecting biofilms.

TM with differing thicknesses. For each of the five abnormal ears, a biofilm was confirmed, but the three-dimensional biofilm colonization within these middle ears could not be described with the current OCT system. Variations of the power reflectance and acoustic resistance features, such as the frequencies at which abnormal elevation of the power reflectance (depression of the normalized resistance) occur, may be related to spatial and thickness variations of the biofilm colonizations. Therefore, modeling acoustic measurements of biofilm ears will likely require consideration of the two- and three-dimensional structural features of biofilms adherent to the TM.

Considering previous reflectance studies of pathological ears, the power reflectance of the OCT-confirmed biofilm ears shows deviations from normal that are dissimilar to the well-studied systematic changes wrought by other middle ear conditions. The power reflectance measurements of the ears that were diagnosed with a biofilm alone, particularly ears B1 and B4, show a potentially unique profile due to the biofilms. All ears show some degree of 'reverse slope' behavior of the power reflectance, between 0.5 and 2 [kHz], related to the abnormal decrease in the normalized resistance.

The most likely confounding conditions in these ears are TM thickening or fluid presence. Ears with biofilms may share some acoustic properties with ears that have a thickened or inflamed TM, because a biofilm is a plaque

buildup on the TM. However, the effects of these two conditions may not be exactly the same, due to differing tissue properties. Considering previous power reflectance measurements of OM ears (e.g. Piskorski et al., 1999 ($N = 1$, child); Feeney et al., 2003 ($N = 4$, adult); Allen et al., 2005 ($N = 1$, child); Beers et al., 2010 ($N = 42$, children)), OM typically causes an elevated reflectance level across most frequencies. The power reflectance measurements of biofilm ears B2 and B3, which were also diagnosed with fluid, show similar traits to existing OM with effusion data; ear B3 has an elevated reflectance across all frequencies, and ear B2 has an elevated reflectance at high frequencies.

Ears B2 and B3 also have a lower normalized resistance (Fig. 6.3c) at high frequencies than the biofilm-only ears. It is possible that the acoustic effects of an effusion and a bacterial biofilm may both cause a depressed normalized acoustic resistance, but for different frequency ranges. Though a power reflectance of 1 does not necessarily mean that the resistance is zero, as mentioned previously, it is provable that a resistance of 0 forces the power reflectance to be 1. Considering previous studies, the power reflectance for ears with an effusion may be close to 1 across all, or most, frequencies. Thus, while biofilm ears may have an abnormally low normalized resistance (high power reflectance) in the 1 to 3 [kHz] range, OM ears with effusion may have an abnormally low normalized resistance over a wider range of frequencies due to fluid interfering with the TM and ossicular motion.

6.4 Pole-Zero Results

An acoustic summary and pole-zero fit is shown for each of the five ears with OCT-confirmed bacterial biofilm in Appendix B (Figs. B.29 through B.33). Some useful parameters associated with these fits, such as the residual canal length estimate $\hat{L}$, are given in Table B.1. Extensive analysis and modeling of these pole-zero fits was not performed, because these fits have relatively high error due to noise in the data. For instance, ear B2 (Fig. B.30), which might be considered the lowest quality measurement, has a lot of noise which causes strange behaviors in the fit at low frequencies. This results in an abnormally high $\hat{L}$ estimate of 17.2 [mm], which is most likely very inaccurate.

Still, there are some consistent irregularities in the fits $\hat{\Gamma}_{mp}(s)$ that charac-

terize the abnormal behavior of the reflectance magnitude, due to bacterial biofilm. Considering the 1 to 3 [kHz] range, where the reflectance magnitude is abnormally high for all five biofilm ears, there a number of unpaired poles of $\hat{\Gamma}_{mp}(s)$, or poles with relatively small damping compared to their neighboring zeros. These poles appear to characterize the abnormal peaks of the reflectance magnitude. The fit $\hat{\Gamma}_{mp}(s)$ of ear B1 (Fig. B.29) has a lone pole at $\omega/2\pi = 2$ [kHz], as do the fits to ears B4 (Fig. B.32) and B5 (Fig. B.33); all three of these ears were diagnosed with bacterial biofilm only. For ears B2 and B3, which also had fluid present, the reflectance magnitude does not have a sharp peak in this frequency region. The fit $\hat{\Gamma}_{mp}(s)$ to ear B2 (Fig. B.30) also has a lone pole just above 2 [kHz], but that pole has fairly high damping compared to other poles and zeros in the fit. For ear B3 (Fig. B.31), $\hat{\Gamma}_{mp}(s)$ has a pole just below 2 [kHz] that is more widely spaced from its neighboring zero than is typically seen for the fine structure minima and maxima of the reflectance magnitude (Section 5.1).

CHAPTER 7

DISCUSSION

Limitations and theoretical constraints of the fitting procedure are discussed in the following sections, along with potential applications for pole-zero characterization of CAR data. Finally, the key results presented in this thesis are summarized. Because this work places such a large emphasis on the methods, results regarding the diagnosis of specific middle ear pathologies are still somewhat preliminary.

7.1 Limitations

The pole-zero fitting method is limited by the data provided, and will typically not be accurate outside of the measured frequency range (either above or below). Because the reflectance is not known at higher or lower frequencies, the calculation of $\hat{\Gamma}_{ap}(s)$, approximating the residual ear canal effect, must be inherently imperfect [Voss and Allen, 1994]. Additionally, the appropriate relative order of the fit (N_z vs. N_p) is related to high frequency asymptotic behavior of the data, which may be unknown. As stated in Section 3.2, the relative order is determined by the values of D and E in Eq. 3.2; these fit the high frequency data, because all other terms (e.g. $C_i/(s - A_i)$) go to zero for large ω values.

Pole-zero fits to the data are also impacted by the estimated surge resistance r_0 (Eq. 2.3). The use of an incorrect area value to calculate r_0 will cause errors in the calculation of the reflectance [Rasetshwane et al., 2012]. For the Mimosa Acoustics HearID system, the canal area A is set according to the size of the foam tip used. It has been shown that small variations in the ear canal area relative to the calibration cavity area, within 20%, cause a negligible change in the reflectance measurement [Keefe et al., 1992, Voss and Allen, 1994]. Nonetheless, this will have a small effect on the CAR function

and the pole-zero locations of its approximation.

7.2 Relative Order of $\hat{\Gamma}(s)$

In Section 3.3, it was determined empirically that the fit parameter E should be set to zero when fitting in the reflectance domain, while the value D should not (though it is typically small). When E is forced to zero, the inverse Laplace transform of the reflectance fit $\hat{\Gamma}(s)$ is

$$\hat{\gamma}(t) = D\delta(t) + \sum_{i=1}^{N_p} C_i e^{A_i t} u(t). \tag{7.1}$$

Thus, a non-zero fit parameter D corresponds to an initial Dirac δ-function singularity of the time domain reflectance [Lundberg et al., 2007]; this value D is related to the reflectance fit via

$$\lim_{\sigma \to +\infty} \left[\hat{\Gamma}(s) \right] = D. \tag{7.2}$$

Now consider the surge resistance, which is defined as the initial δ-function singularity of the time domain impedance (Section 2.1). For a transmission line model of the ear canal and middle ear (e.g. having wave propagation) the impedance $Z(s)$ at the probe tip has the property

$$\lim_{\sigma \to +\infty} \left[Z(s) \right] = \bar{r}_0, \tag{7.3}$$

where $\bar{r}_0$ is the true surge resistance, a real-valued constant. Considering Eq. 2.3 in this limit, we find

$$\lim_{\sigma \to +\infty} \left[\Gamma(s) \right] = \frac{\bar{r}_0 - r_0}{\bar{r}_0 + r_0}. \tag{7.4}$$

If r_0 is equal to the true surge resistance $\bar{r}_0$, the limit of $\Gamma(s)$ as $\sigma \to +\infty$ must be zero. This means there must be no initial δ-singularity in the time domain reflectance. Thus, considering Eqs. 7.2 and 7.4, D should be zero; a non-zero value of D may indicate a fitting inaccuracy, or the use of an incorrect r_0 value. In the latter case, if the fitting procedure yields a good approximation of the initial singularity in the time domain reflectance, due to

an incorrect r_0 value, D might be used to estimate the true surge resistance value from the CAR data via

$$\bar{r_0} = r_0 \frac{1+D}{1-D}. \tag{7.5}$$

7.3 Applications

The fitting algorithm is fast, and may be easily implemented in a reflectance measurement system. Ultimately, it may allow for more robust automated classification than visual assessment or correlations between magnitude reflectance values and audiometric measurements. Pole-zero fitting is advantageous because it reduces the entire complex response to a small set of parameters, without extensive processing of the CAR data. Further study will be needed to meet this objective, using larger sets of normal and pathological CAR data in combination with known physical characteristics of normal and pathological middle ears, to establish final classification strategies.

Pole-zero fits may also be used to synthesize network models of the complex impedance (e.g. Brune, 1931, Van Valkenburg, 1964). However, such RLC networks will not necessarily be unique. Networks synthesized from pole-zeros fits of CAR measurements will often lack direct physical interpretations present in other models, such as the Zwislocki [1962], Kringlebotn [1988], or Parent and Allen [2010] models. However, they will have great utility for quantifying CAR data.

As stated in Section 1, pole-zero fits are not intended to be used in their raw form in the clinical realm; a visual diagnosis may be much better achieved by considering the absorbance level in [dB], as shown in Fig. 4.5b. However, this method may be of great value for modeling and diagnosis of middle ear pathologies based on reflectance. Pole-zero fitting allows for a concise quantitative representation of reflectance that can be useful when designing algorithms to automatically detect pathologies.

7.4 Summary

This thesis establishes a methodology for examining the physical and mathematical properties of CAR data using pole-zero fitting. Pole-zero fits can characterize CAR data with low error and small number of parameters. For instance, 112 CAR measurements of normal ears from Rosowski et al. [2012], measured by the Mimosa Acoustics HearID system over 0.2 to 6 [kHz], may be fit with 12 poles, 12 zeros, and an average RMS relative error of 2.1%. It was determined that for the present analysis it is best to fit the CAR (Γ) measurements directly, instead of fitting in the impedance (Z) or admittance (Y) domain. This is because, across multiple data sets, the reflectance domain fits had the lowest fitting error for a given pole order. Additionally, it is convenient to fit reflectance domain data because the fitting algorithm ensures that $\hat{\Gamma}(s)$ is stable prior to factorization into its minimum-phase and all-pass components. It was empirically determined that reflectance domain data should be fit with an equal number of poles and zeros ($N_z = N_p$; D is nonzero), even though in theory the reflectance should have fewer poles than zeros. This discrepancy may be due to the limited frequency range of the data or an incorrect estimate of the surge resistance r_0, among other things.

While considering the complex data instead of the reflectance magnitude reintroduces undesired variation due to the residual ear canal, measurements may be effectively compared across ears by factoring the reflectance fit into its minimum-phase and all-pass components. The magnitude of the minimum-phase component of the CAR is, by definition, equal to the reflectance magnitude, thus preserving the current diagnostic standard. It was found that the all-pass factor of the reflectance fit resembles a delay, presumably from the ear canal. In some cases this delay is frequency dependent, which is likely due to the non-uniform area of the ear canal or lossless delay in the TM. Estimating the residual ear canal contribution with the all-pass factor, reasonable estimates were achieved for the residual canal length, indicating that this approximation has utility for analyzing pole-zero fits to CAR data.

In this investigation, it was established that reflectance domain fits show distinct pole-zero pairs in the mid-frequency region of individual variation for normal ears, from about 1 to 4 [kHz], characterizing the fine structure minima and maxima of the magnitude reflectance. Perhaps the most important marker of a normal middle ear is the breakpoint between the rising slope and

the flat region of the absorbance level, corresponding to the first minimum of the magnitude reflectance. This breakpoint is typically characterized by a closely-placed pole-zero pair located near 1 [kHz]. If this feature is missing or shifted in frequency in the pole-zero fit, it may be an indication of middle ear pathology.

Considering pathological data from Nakajima et al. [2012], some pole-zero features for stapes fixation due to otosclerosis, ossicular discontinuity, and SSCD were determined. It was found that stapes fixation due to otosclerosis may be partially characterized by modeling the low frequency compliance of the TM impedance, estimated using the minimum-phase component of the reflectance fit. Ossicular discontinuity appears to be well-characterized by a lone zero with a relatively small damping value between about 0.5 and 0.8 [kHz], in combination with the absence of a typical 1 [kHz] pole-zero pair, indicating an abnormal breakpoint. This zero characterizes the resonance due to increased compliance in one of the ossicular joints (typically the incudo-stapedial joint). Finally, SSCD may be partially characterized by an atypically wide spacing of the pole-zero pair near 1 [kHz], corresponding to an unusually deep notch in the magnitude reflectance at that frequency.

In the biofilm study, it was determined that an abnormally low normalized resistance in the 1 to 3 [kHz] range, which corresponds to a 'reverse slope' behavior in the 0.5 to 2 [kHz] range, is the main feature distinguishing the five biofilm cases from normal ears. Future study of a wide range of OM-related conditions, with definitive biofilm and non-biofilm classifications, is needed. Considering pole-zero fits to the biofilm ear measurements, in many cases abnormal peaks in the reflectance magnitude between 1 and 3 [kHz] are characterized by unpaired poles, or poles with relatively small damping, in the same frequency range.

Pole-zero modeling provides a concise, parametric characterization of CAR data, which should enable improved automated identification of middle ear pathology using a noninvasive, yet relatively low cost measurement system. Further analysis of large data sets is required to determine the best features for classification of various middle ear pathologies. However, the preliminary results presented in this thesis show promise for classification and modeling of middle ear pathologies using pole-zero fits to CAR data.

APPENDIX A

VECTOR FITTING

A vector fitting procedure developed by Gustavsen and Semlyen [1999] is used to fit complex, frequency domain data to a function of the form shown in Eq. 3.2. The vector fitting procedure is an iterative two step process, which converts a nonlinear least squares problem to a linear least squares problem by introducing an unknown scaling function Θ, having known poles. Let the iteration index of the algorithm be denoted by m=1,2,...,M. Note that the pole order of the algorithm is fixed; if some error criterion is not met, the algorithm may be re-run with a greater number of poles N_p. On each iteration, a least squares problem is solved based on the following equations:

$$H_m(s) = \sum_{i=1}^{N_p} \frac{c_{i,m}}{s - a_{i,m-1}} + d_m + e_m s \tag{A.1}$$

$$\Theta_m(s) = \sum_{i=1}^{N_p} \frac{b_{i,m}}{s - a_{i,m-1}} + 1. \tag{A.2}$$

These equations are linear in their unknowns $c_{i,m}$, d_m, e_m, and $b_{i,m}$. Both $\Theta_m(s)$ and $H_m(s)$ share the same known poles $a_{i,m-1}$, which have either been determined in the previous iteration, or initialized by the user. It is important that $\Theta_m(s)$ and $H_m(s)$ have the same poles, because the poles algebraically cancel when a ratio of the functions is taken in a later step of the algorithm (Eq. A.4). The algorithm iterates to converge on the unknown poles $A_i = a_{i,M}$ of the fit $\hat{F}(s) = F_M(s)$ (which are a nonlinear unknown in Eq. 3.2). The initial poles $a_{i,0}$ are the 'starting poles' of the algorithm; their selection will be described below.

The vector fitting method relates Eqs. A.1 and A.2 to the measured data $F(\omega_k)$ at a given frequency index k via

$$\Theta_m(s)\Big|_{s=j\omega_k} F(\omega_k) = H_m(s)\Big|_{s=j\omega_k}. \tag{A.3}$$

When evaluated over the many available frequency points of $F(\omega)$, Eq. A.3 results in an over-determined linear problem in the unknowns $c_{i,m}$, d_m, e_m, and $b_{i,m}$. At each algorithm step, the current fit is given by

$$F_m(s) = \frac{H_m(s)}{\Theta_m(s)} \tag{A.4}$$

using the estimated values of $c_{i,m}$, d_m, e_m, and $b_{i,m}$. This fit is related to the data via

$$F(\omega) \approx F_m(s)\Big|_{s=j\omega} \tag{A.5}$$

and should improve with iteration.

Because $H_m(s)$ and $\Theta_m(s)$ share the same poles, by construction there is a perfect cancellation in Eq. A.4. Thus, upon iteration, the zeros of $\Theta_m(s)$ become the poles of $F_m(s)$. To see this, consider the product forms of Eqs. A.1 and A.2 for a non-zero e_m,

$$H_m(s) = \frac{e_m \prod_{i=1}^{N_p+1}(s - z_{i,m})}{\prod_{i=1}^{N_p}(s - a_{i,m-1})} \tag{A.6}$$

$$\Theta_m(s) = \frac{\prod_{i=1}^{N_p}(s - a_{i,m})}{\prod_{i=1}^{N_p}(s - a_{i,m-1})}, \tag{A.7}$$

where $z_{i,m}$ are the zeros of $H_m(s)$, $a_{i,m}$ are the zeros of $\Theta_m(s)$, and $a_{i,m-1}$ are the known poles of both functions. Substituting Eqs. A.6 and A.7 for Eq. A.4 yields

$$F_m(s) = \frac{H_m(s)}{\Theta_m(s)} = \frac{e_m \prod_{i=1}^{N_p+1}(s - z_{i,m})}{\prod_{i=1}^{N_p}(s - a_{i,m})}. \tag{A.8}$$

Thus, on each iteration the zeros of the scaling function $\Theta_m(s)$ become the poles of the fitted function $F_m(s)$. On the last iteration, the poles $a_{i,M}$ become the poles of $F_M(s) = \hat{F}(s)$ (Eq. 3.2) such that $A_i = a_{i,M}$. Gustavsen and Semlyen found that it is better to calculate the remaining quantities C_i, D, and E via the least squares procedure outlined by Eq. A.3, using $a_{i,M}$ as the starting poles. Thus, the final quantities $C_i = c_{i,M+1}$, $D = d_{M+1}$, and $E = e_{M+1}$ are the result of a partial iteration.

An appropriate selection of starting poles $a_{i,0}$ is necessary for the convergence of the vector fitting method. For a function with resonance peaks,

such as the reflectance, Gustavsen and Semlyen [1999] suggest that the starting poles (complex conjugate pairs $a_{i,0} = -\alpha_{i,0} \pm j\beta_{i,0}$, with $\alpha_{i,0} = \beta_{i,0}/100$ advised) be linearly distributed over the frequency range of the data. The linear problem can become ill-conditioned if the starting poles are real. Large differences between the starting poles and the best fit poles of the response can cause large differences between $\Theta_m(s)$ and $H_m(s)$ resulting in poor least squares solutions [Gustavsen and Semlyen, 1999].

If the least squares procedure returns unstable poles ($\mathrm{Re}\{a_{i,m}\} > 0$), their real parts are reflected to the left half s-plane before the next iteration. Due to this, the error will not always decrease monotonically with iteration. Depending on the application, it may also be beneficial to impose additional properties. For example, one might force the impedance to be minimum-phase, instead of merely stable. This could be done by inverting the real part of any zero that appears in the RHP, similar to the procedure for enforcing stability of the poles. Such a constraint may cause an increase in error, but could have utility for physical modeling.

The error depends on the starting pole values due to noise in the data. Additionally, due to the smoothness of the reflectance function and the number of available parameters, there exist multiple non-unique fits yielding reasonable fit errors (e.g. within a certain MSE tolerance). Thus the poles (of an already low error fit) may vary with iteration, resulting in non-monotonic error. Typically, significant MSE improvement over the first few iterations occurs only for low pole orders (e.g. $N_p < 10$ over a 0.1 to 10 [kHz] range). For high pole orders (e.g. $N_p > 20$ over the same range) the fitting procedure achieves close to its lowest MSE within one iteration. When the order is approximately known, as it is here, the starting poles better cover the entire frequency range, causing the fit to commonly converge within a few iterations. For low orders of poles, more iterations may be necessary to migrate the poles to their best fit locations.

APPENDIX B

POLE-ZERO FITS OF PATHOLOGICAL EARS

Table B.1: Useful parameters of the pole-zero fits in Figs. B.1 to B.33.

Ear	**Pathology**	**Zeros/Poles**	**MSE [dB]**	$\hat{L}$ **[mm]**
P008L	Stapes Fixation	12/12	-34.8	10.9
P027R	Stapes Fixation	12/12	-32.8	13.5
P029R	Stapes Fixation	10/10	-35.5	5.4
P031L	Stapes Fixation	12/12	-38.0	8.4
P034R	Stapes Fixation	12/12	-36.4	11.4
P035R	Stapes Fixation	10/10	-34.3	13.0
P039L	Stapes Fixation	14/14	-29.5	7.0
P041R	Stapes Fixation	12/12	-35.5	11.1
P042R	Stapes Fixation	14/14	-35.5	6.0
P049L	Stapes Fixation	10/10	-32.2	8.7
P056L	Stapes Fixation	14/14	-36.6	8.1
P062L	Stapes Fixation	10/10	-40.3	11.7
P067L	Stapes Fixation	12/12	-35.5	15.0
P014L	Ossicular Discontinuity	12/12	-33.9	5.1
P015L	Ossicular Discontinuity	14/14	-32.4	9.7
P028L	Ossicular Discontinuity	10/10	-33.2	9.4
P054R	Ossicular Discontinuity	10/10	-29.6	4.3
P071L	Ossicular Discontinuity	14/14	-33.3	9.4
P083L	Ossicular Discontinuity	6/6	-30.5	11.8
P018L	SSCD	12/12	-32.1	13.5
P044L	SSCD	14/14	-29.9	10.5
P052L	SSCD	10/10	-33.2	8.3
P059R	SSCD	10/10	-33.3	8.1
P074L	SSCD	14/14	-38.3	10.7
P082L	SSCD	12/12	-30.6	11.7
P087R	SSCD	12/12	-30.6	9.8
P103R	SSCD	14/14	-26.3	9.7
P104L	SSCD	12/12	-30.1	6.7
B1	Bacterial Biofilm	11/12	-28.6	10.9
B2	Bacterial Biofilm	10/10	-27.6	17.2
B3	Bacterial Biofilm	8/8	-30.6	7.9
B4	Bacterial Biofilm	14/14	-27.4	11.8
B5	Bacterial Biofilm	12/12	-27.3	4.5

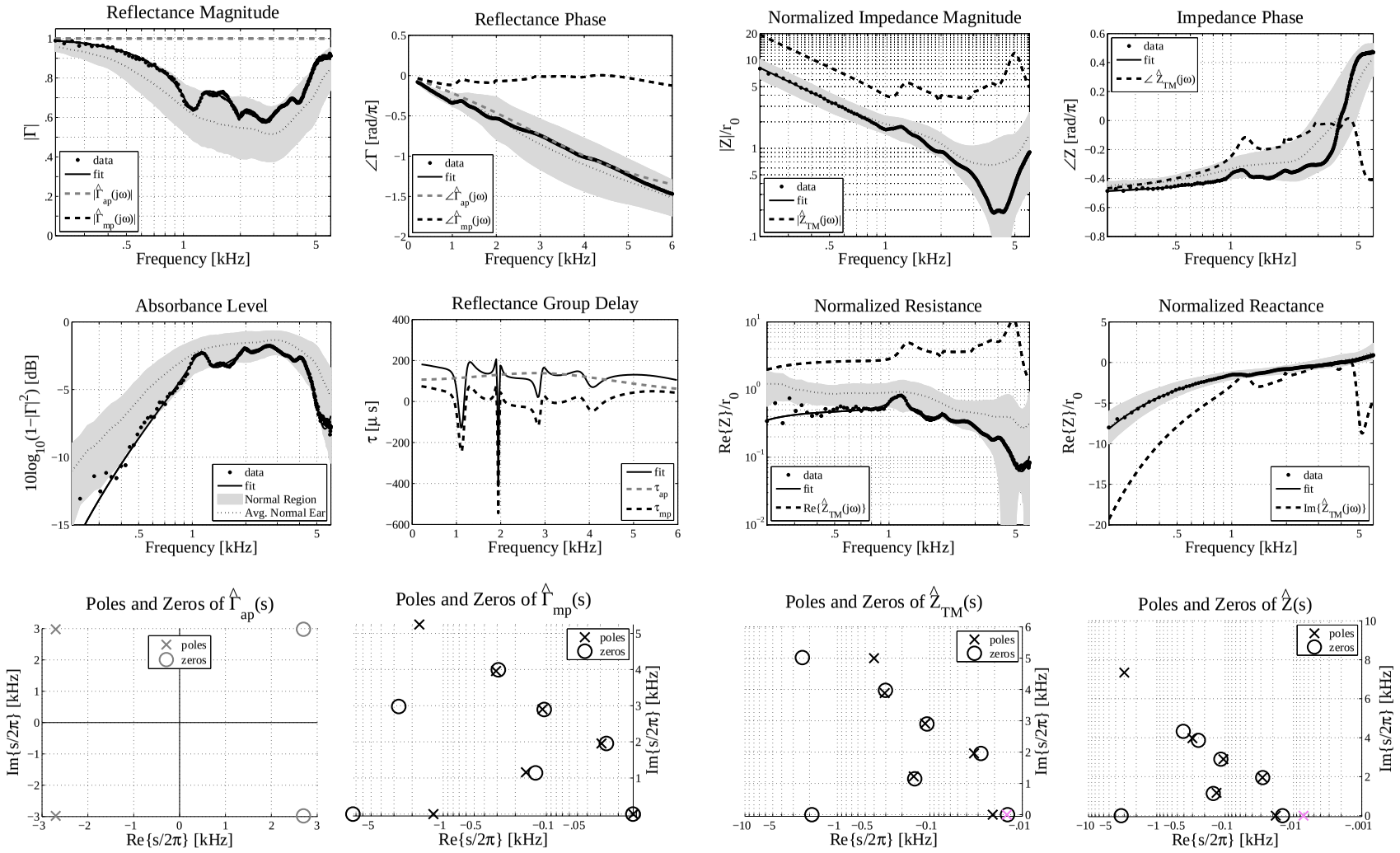

Figure B.1: Acoustic summary and pole-zero fit of an ear with *stapes fixation* due to otosclerosis (P008L) from Nakajima et al. [2012]. The thin dotted black lines and gray regions show the average normal ear ±1 standard deviation from Rosowski et al. [2012]. Factored fit quantities are described in Section 3.4.

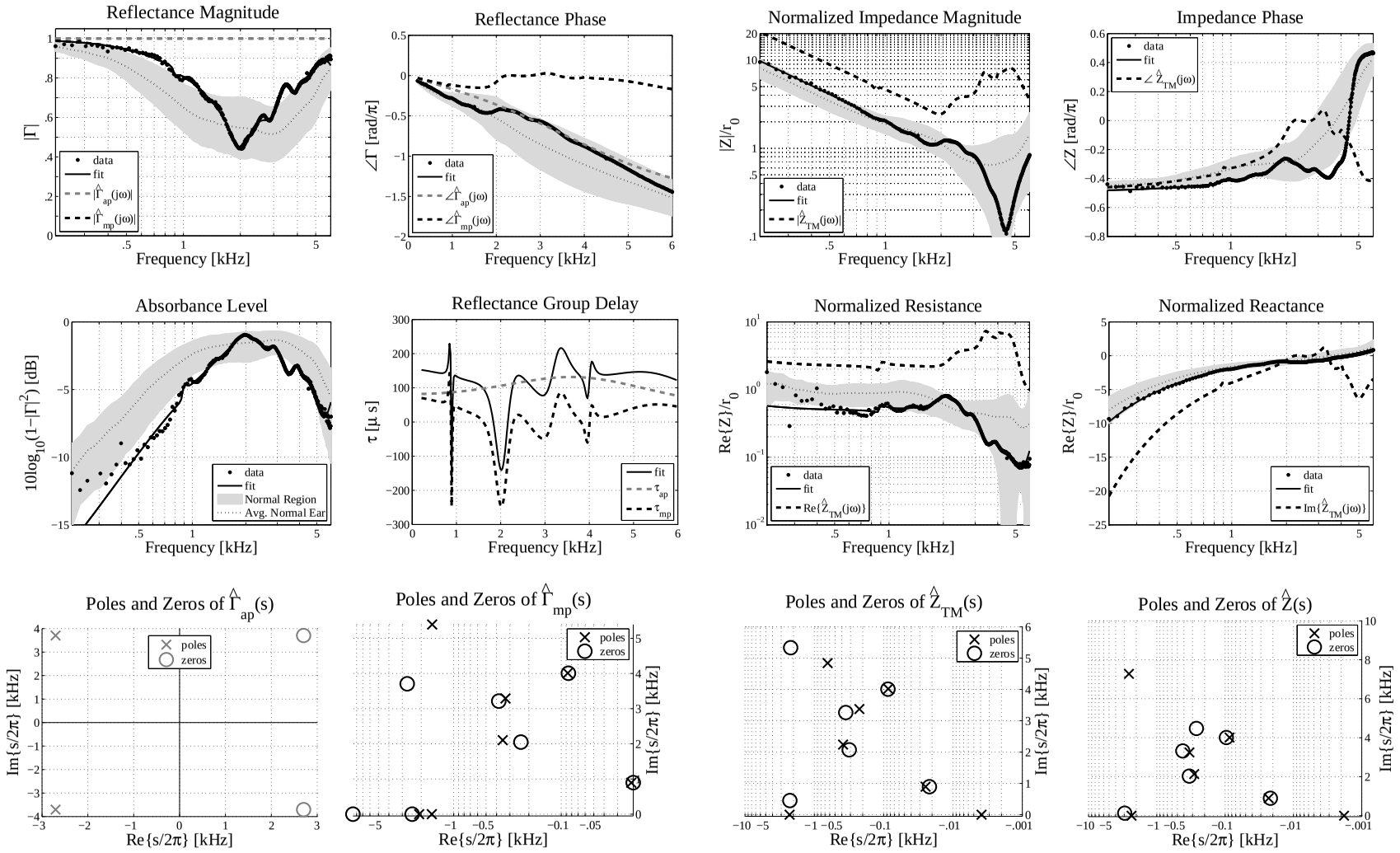

Figure B.2: Acoustic summary and pole-zero fit of an ear with *stapes fixation* due to otosclerosis (P027R) from Nakajima et al. [2012]. The thin dotted black lines and gray regions show the average normal ear ±1 standard deviation from Rosowski et al. [2012]. Factored fit quantities are described in Section 3.4.

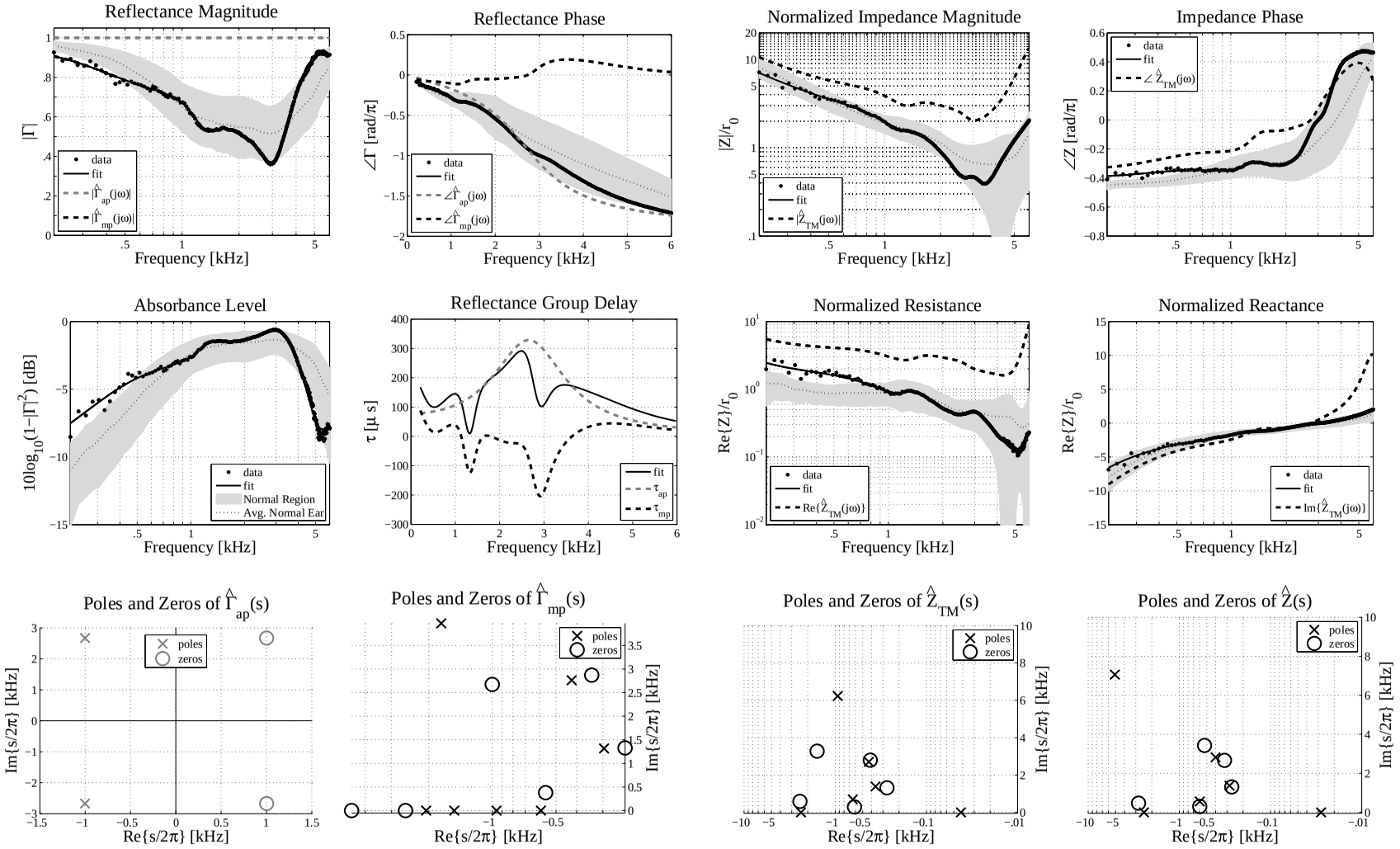

Figure B.3: Acoustic summary and pole-zero fit of an ear with *stapes fixation* due to otosclerosis (P029R) from Nakajima et al. [2012]. The thin dotted black lines and gray regions show the average normal ear ±1 standard deviation from Rosowski et al. [2012]. Factored fit quantities are described in Section 3.4.

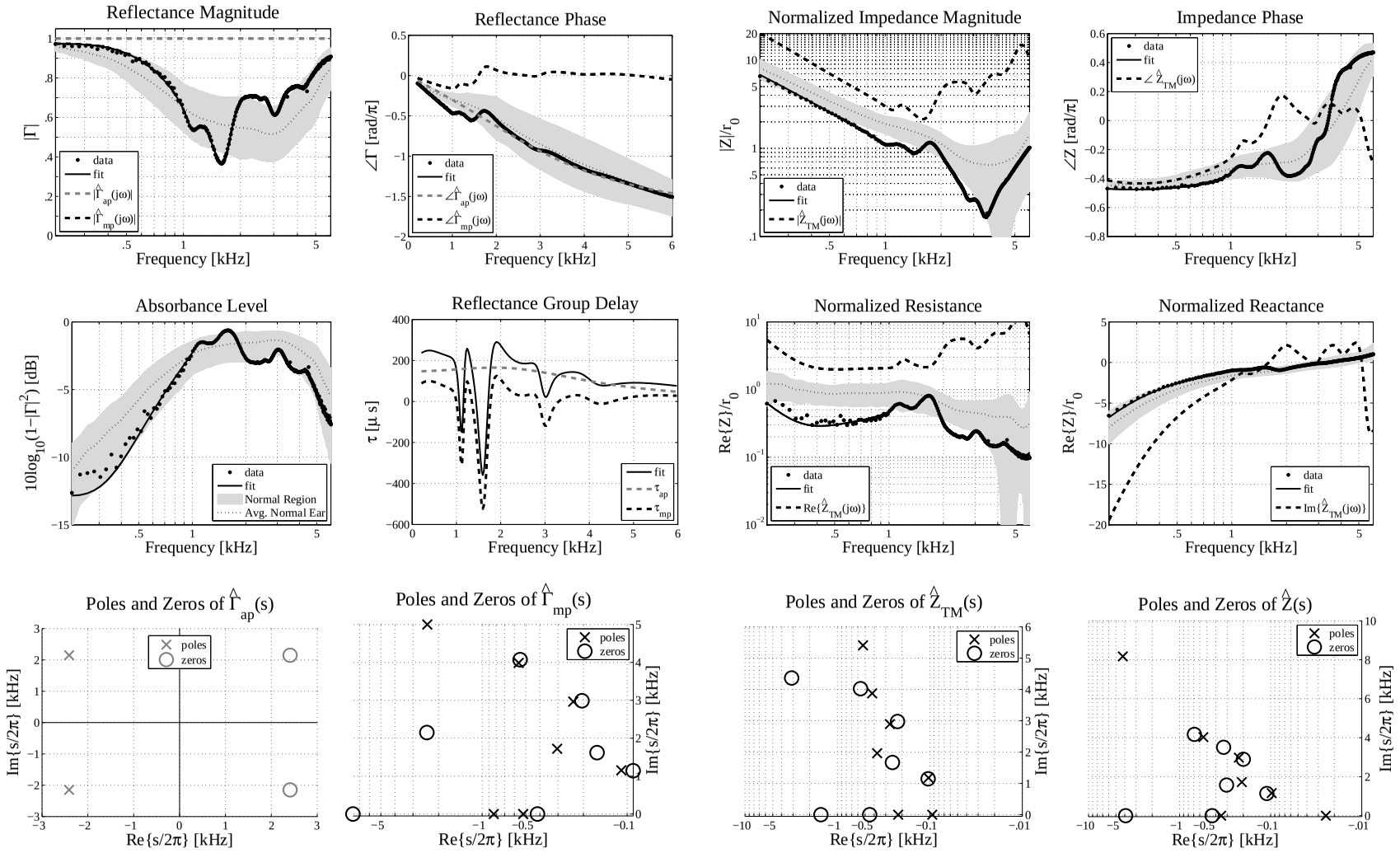

Figure B.4: Acoustic summary and pole-zero fit of an ear with *stapes fixation* due to otosclerosis (P031L) from Nakajima et al. [2012]. The thin dotted black lines and gray regions show the average normal ear ±1 standard deviation from Rosowski et al. [2012]. Factored fit quantities are described in Section 3.4.

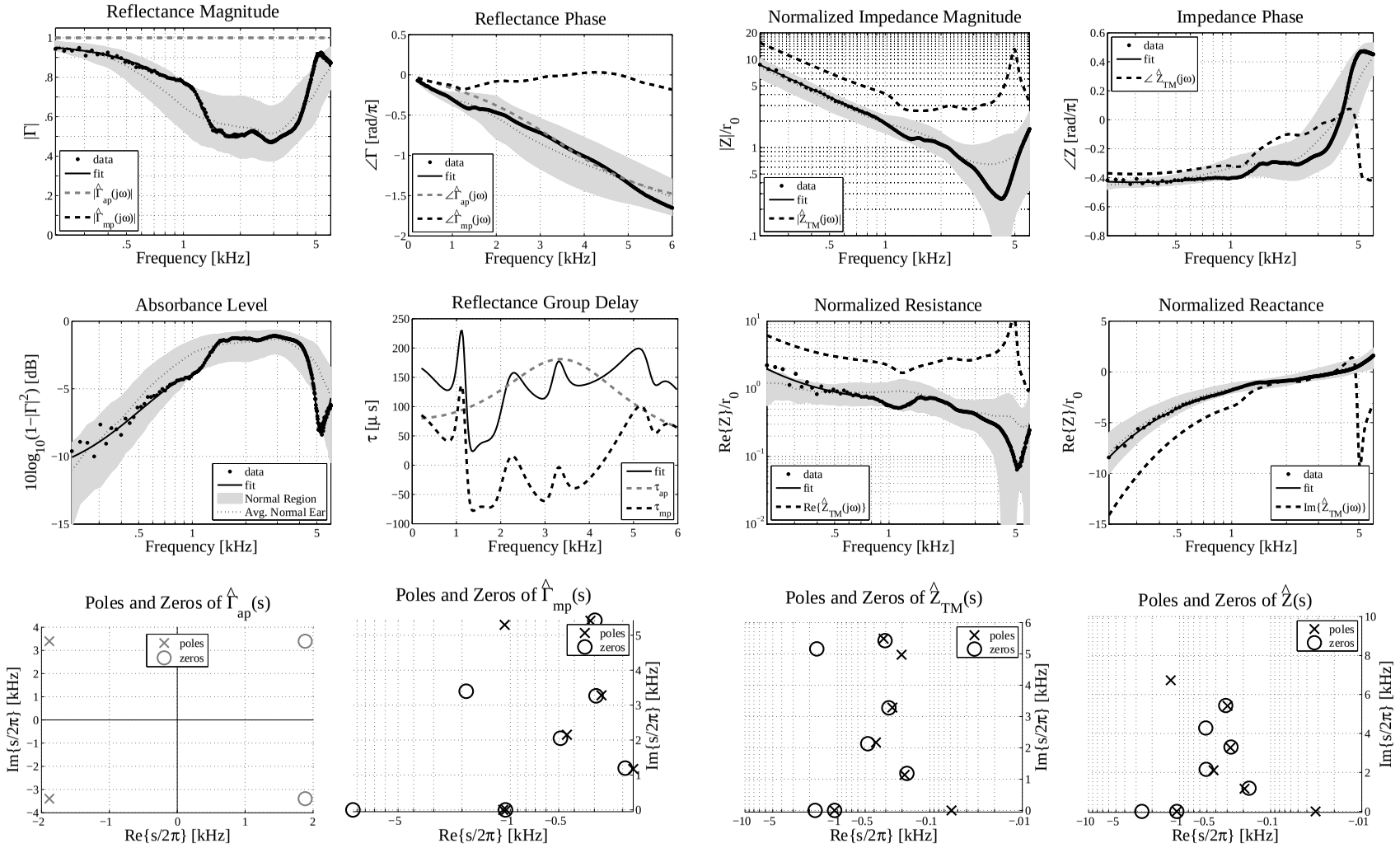

Figure B.5: Acoustic summary and pole-zero fit of an ear with *stapes fixation* due to otosclerosis (P034R) from Nakajima et al. [2012]. The thin dotted black lines and gray regions show the average normal ear ±1 standard deviation from Rosowski et al. [2012]. Factored fit quantities are described in Section 3.4.

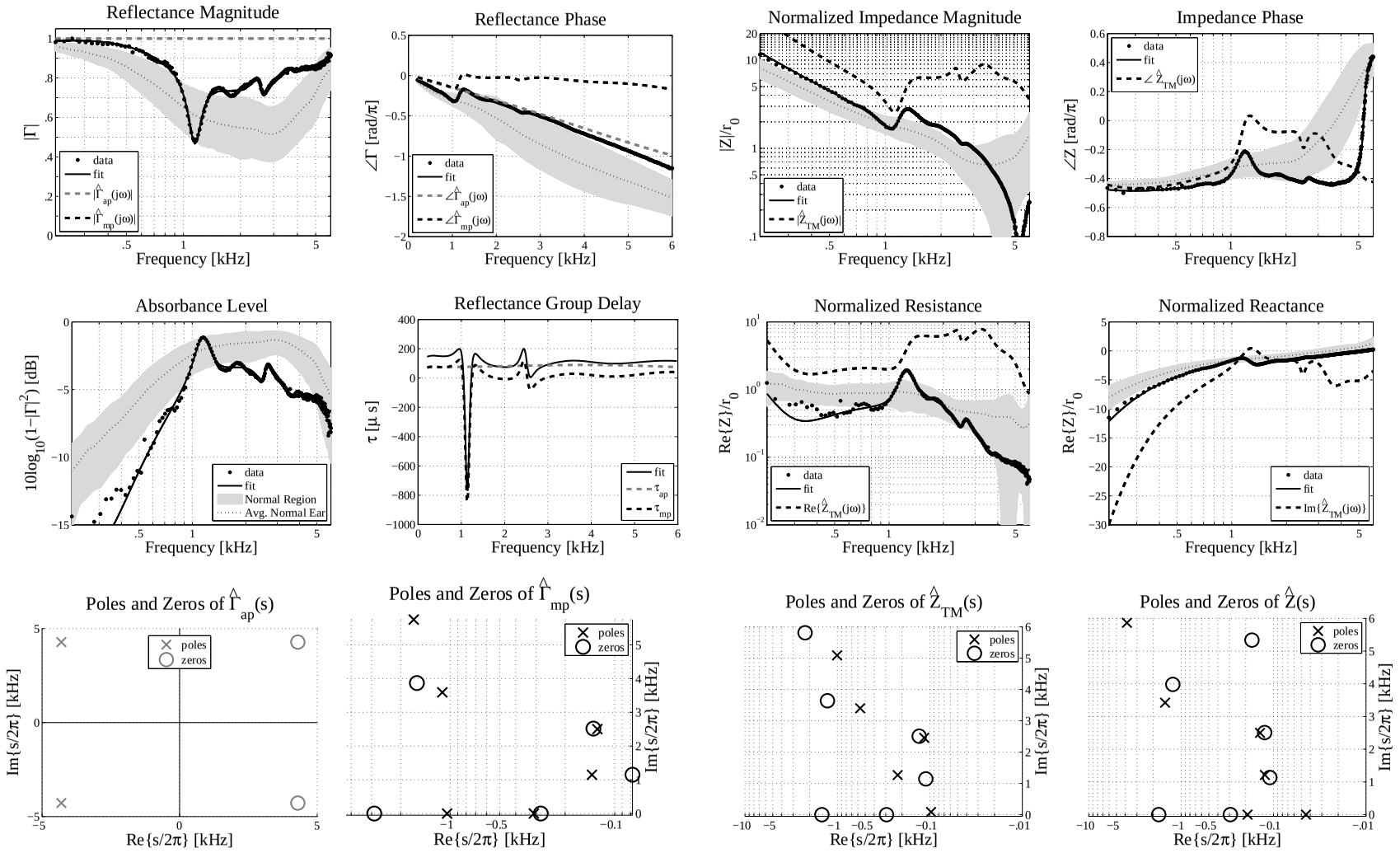

Figure B.6: Acoustic summary and pole-zero fit of an ear with *stapes fixation* due to otosclerosis (P035R) from Nakajima et al. [2012]. The thin dotted black lines and gray regions show the average normal ear ±1 standard deviation from Rosowski et al. [2012]. Factored fit quantities are described in Section 3.4.

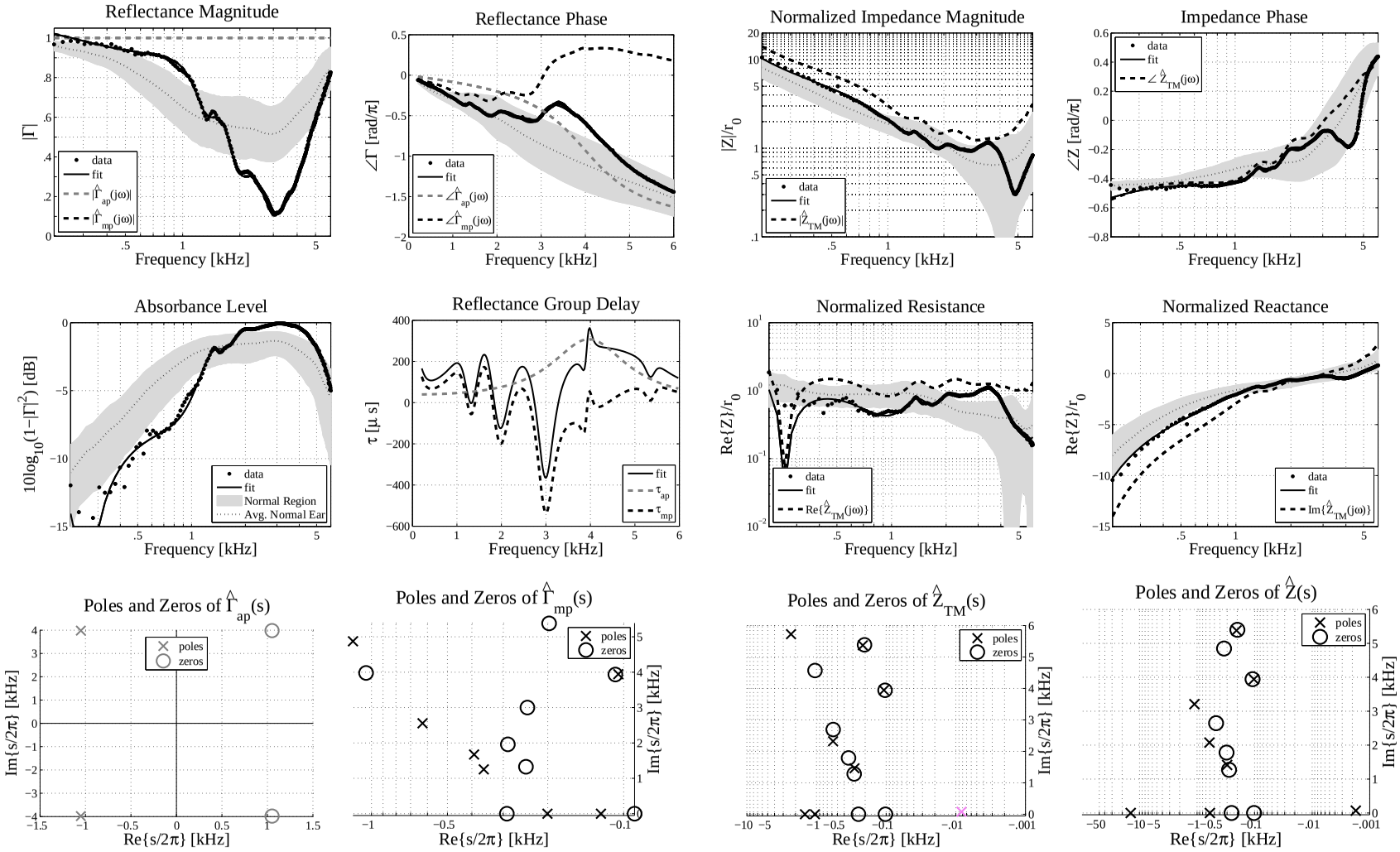

Figure B.7: Acoustic summary and pole-zero fit of an ear with *stapes fixation* due to otosclerosis (P039L) from Nakajima et al. [2012]. The thin dotted black lines and gray regions show the average normal ear ±1 standard deviation from Rosowski et al. [2012]. Factored fit quantities are described in Section 3.4.

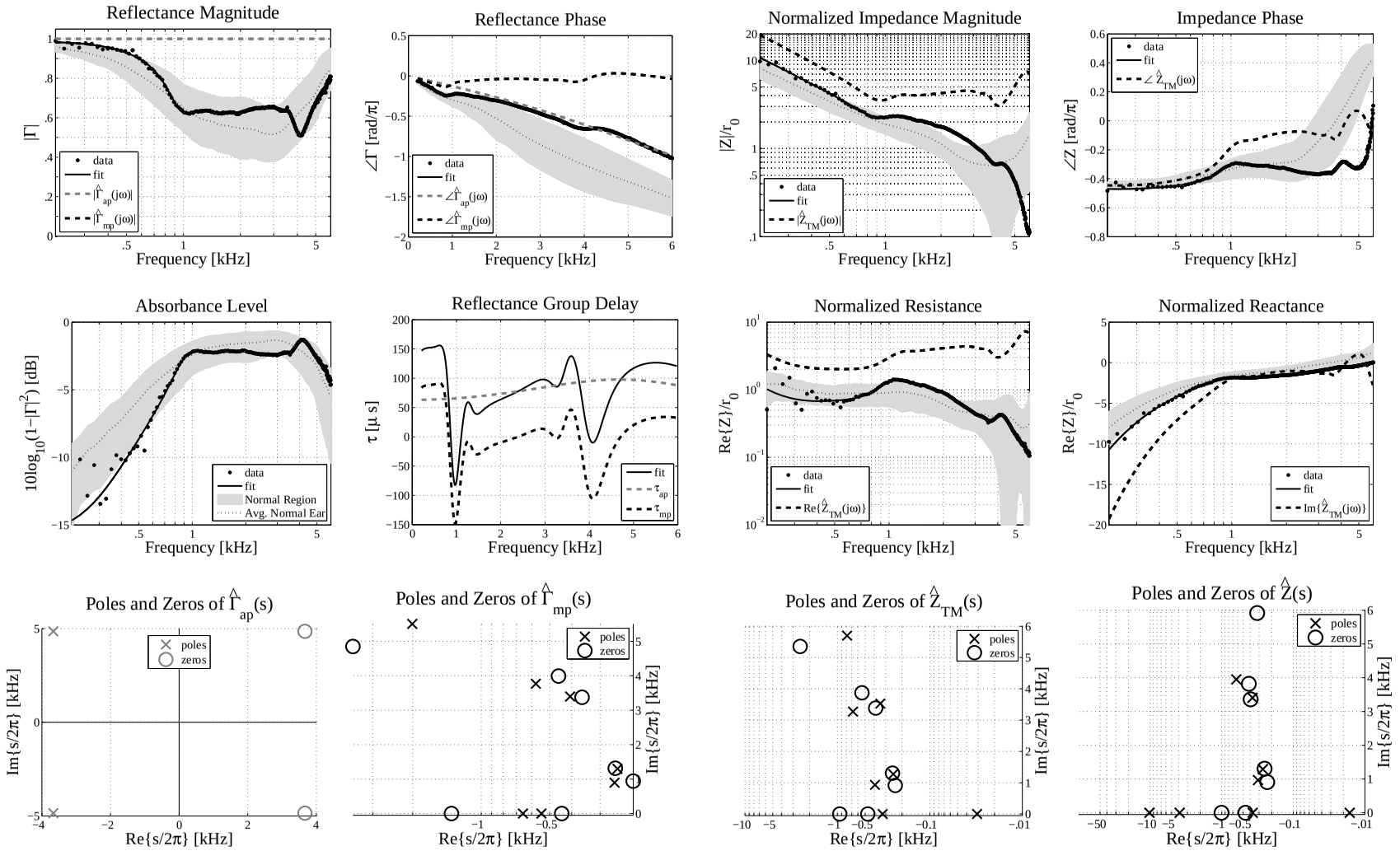

Figure B.8: Acoustic summary and pole-zero fit of an ear with *stapes fixation* due to otosclerosis (P041R) from Nakajima et al. [2012]. The thin dotted black lines and gray regions show the average normal ear ±1 standard deviation from Rosowski et al. [2012]. Factored fit quantities are described in Section 3.4.

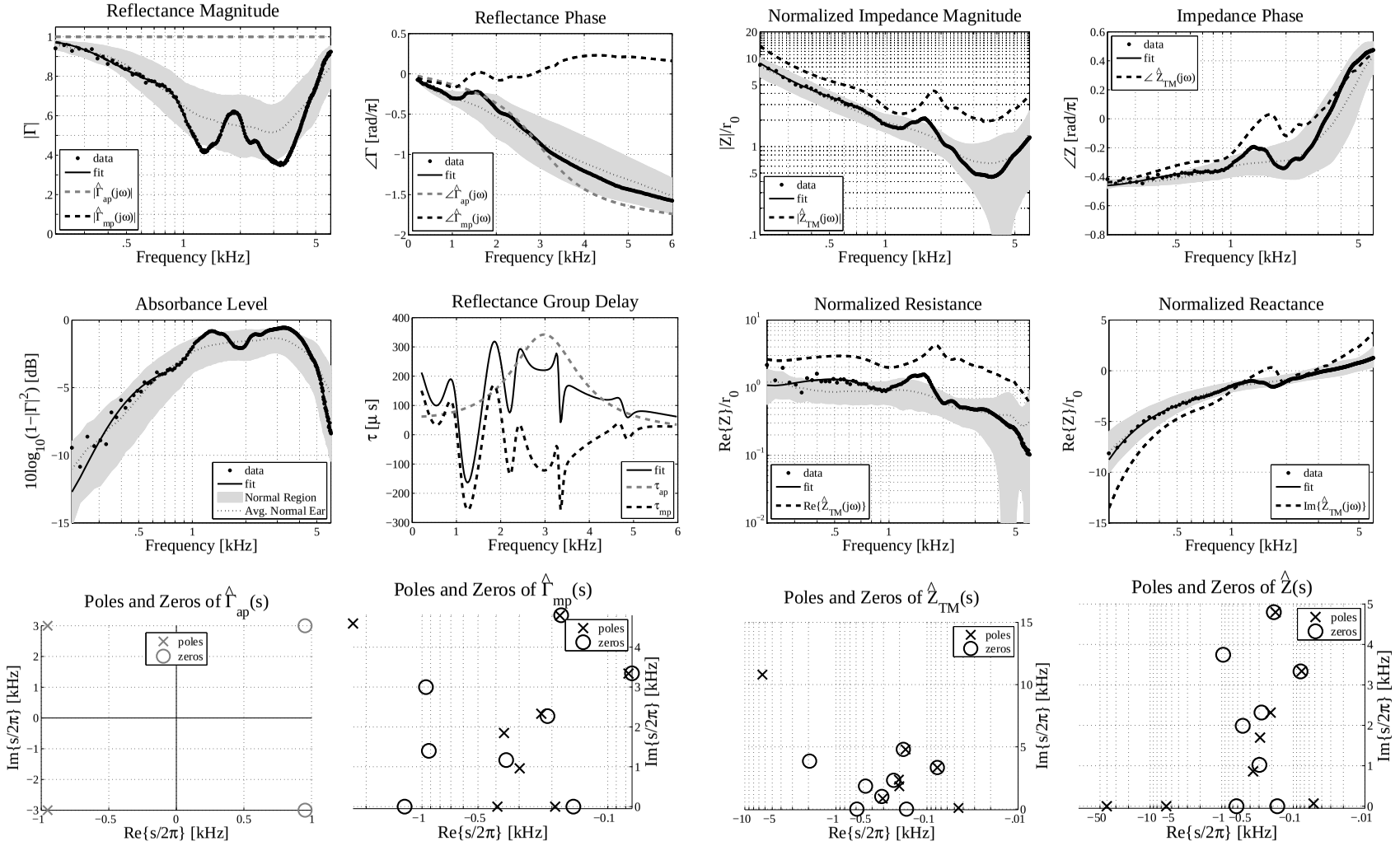

Figure B.9: Acoustic summary and pole-zero fit of an ear with *stapes fixation* due to otosclerosis (P042R) from Nakajima et al. [2012]. The thin dotted black lines and gray regions show the average normal ear ±1 standard deviation from Rosowski et al. [2012]. Factored fit quantities are described in Section 3.4.

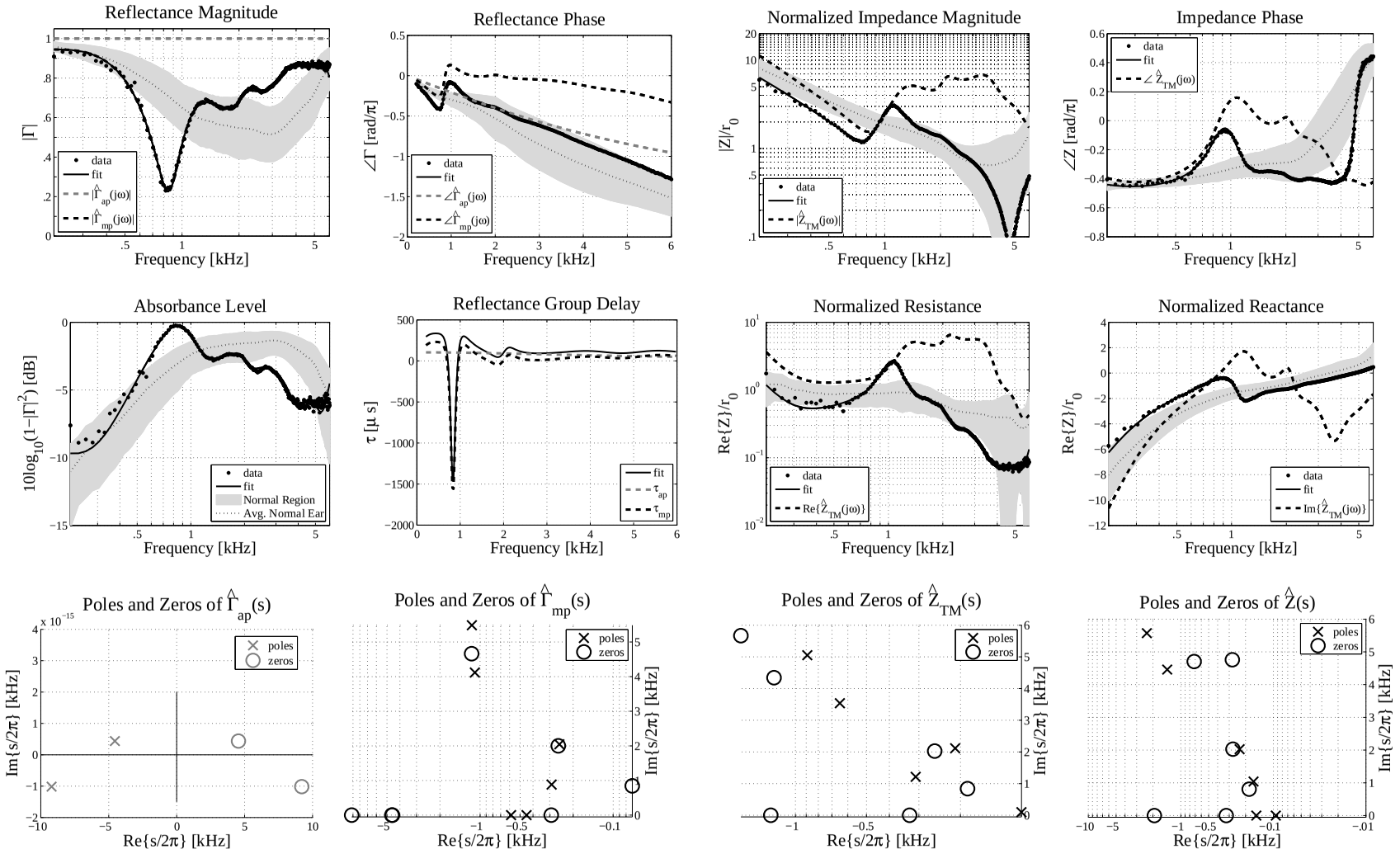

Figure B.10: Acoustic summary and pole-zero fit of an ear with *stapes fixation* due to otosclerosis (P049L) from Nakajima et al. [2012]. The thin dotted black lines and gray regions show the average normal ear ±1 standard deviation from Rosowski et al. [2012]. Factored fit quantities are described in Section 3.4.

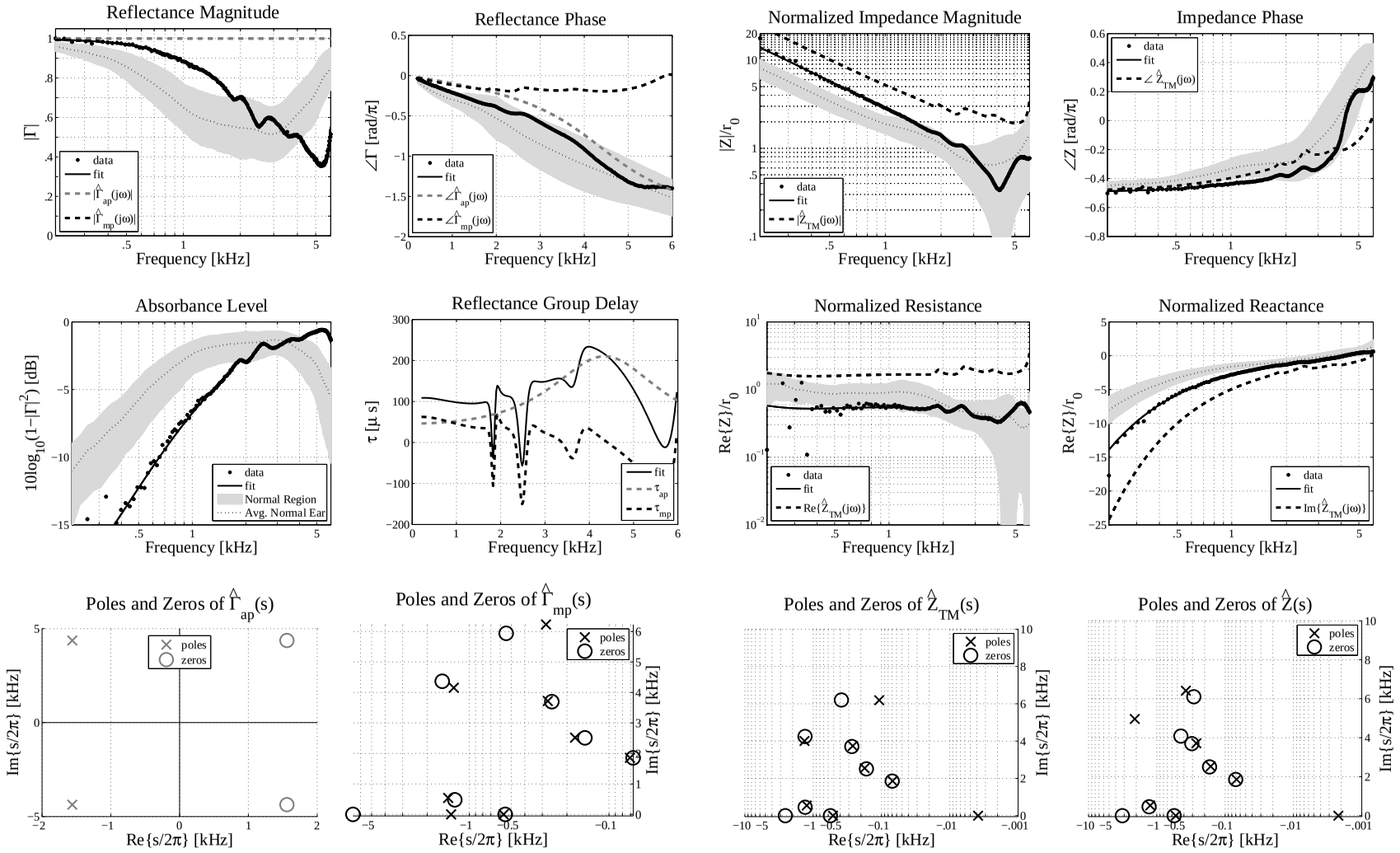

Figure B.11: Acoustic summary and pole-zero fit of an ear with *stapes fixation* due to otosclerosis (P056L) from Nakajima et al. [2012]. The thin dotted black lines and gray regions show the average normal ear ±1 standard deviation from Rosowski et al. [2012]. Factored fit quantities are described in Section 3.4.

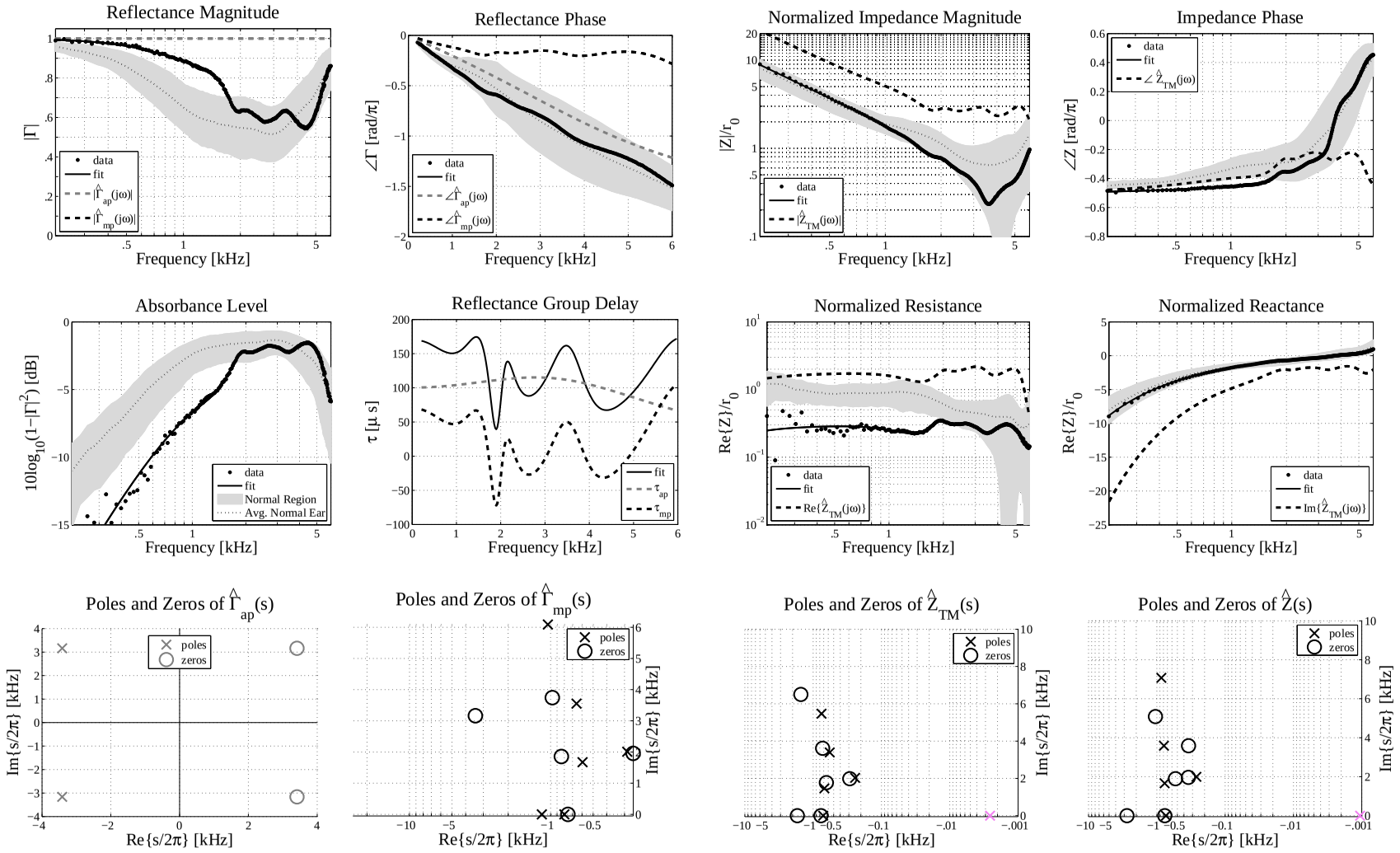

Figure B.12: Acoustic summary and pole-zero fit of an ear with *stapes fixation* due to otosclerosis (P062L) from Nakajima et al. [2012]. The thin dotted black lines and gray regions show the average normal ear ±1 standard deviation from Rosowski et al. [2012]. Factored fit quantities are described in Section 3.4.

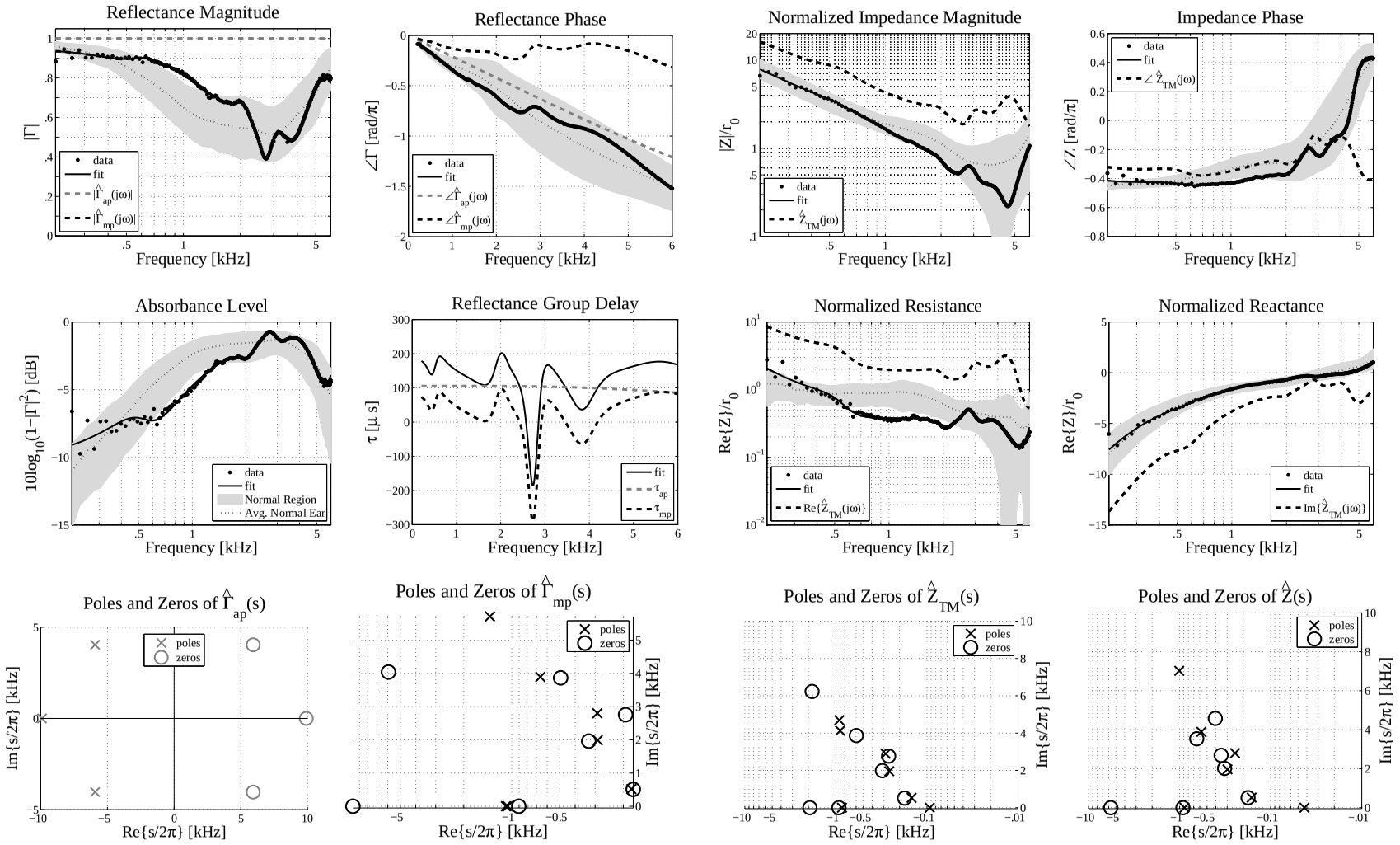

Figure B.13: Acoustic summary and pole-zero fit of an ear with *stapes fixation* due to otosclerosis (P067L) from Nakajima et al. [2012]. The thin dotted black lines and gray regions show the average normal ear ±1 standard deviation from Rosowski et al. [2012]. Factored fit quantities are described in Section 3.4.

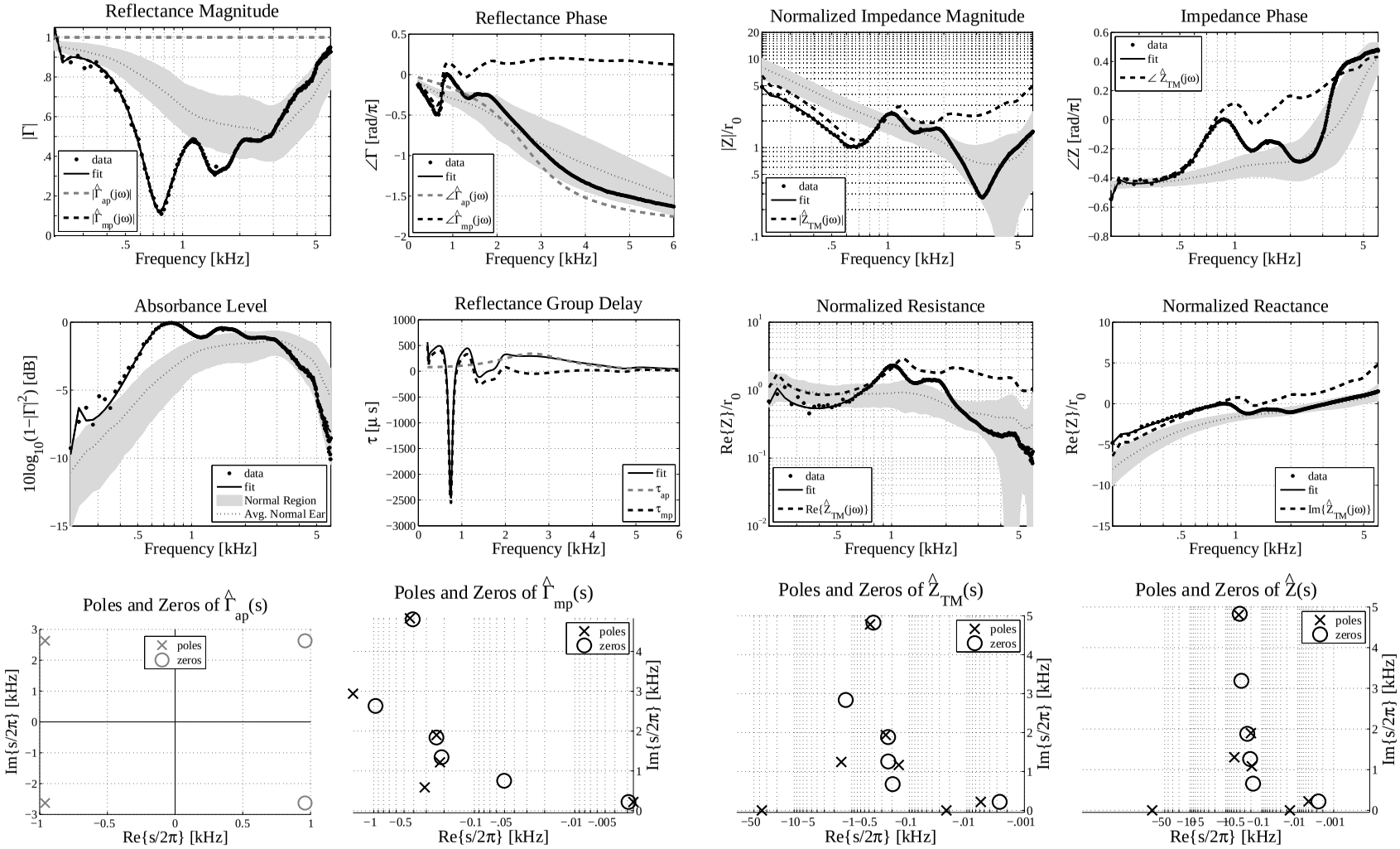

Figure B.14: Acoustic summary and pole-zero fit of an ear with *ossicular discontinuity* (P014L) from Nakajima et al. [2012]. The thin dotted black lines and gray regions show the average normal ear ±1 standard deviation from Rosowski et al. [2012]. Factored fit quantities are described in Section 3.4.

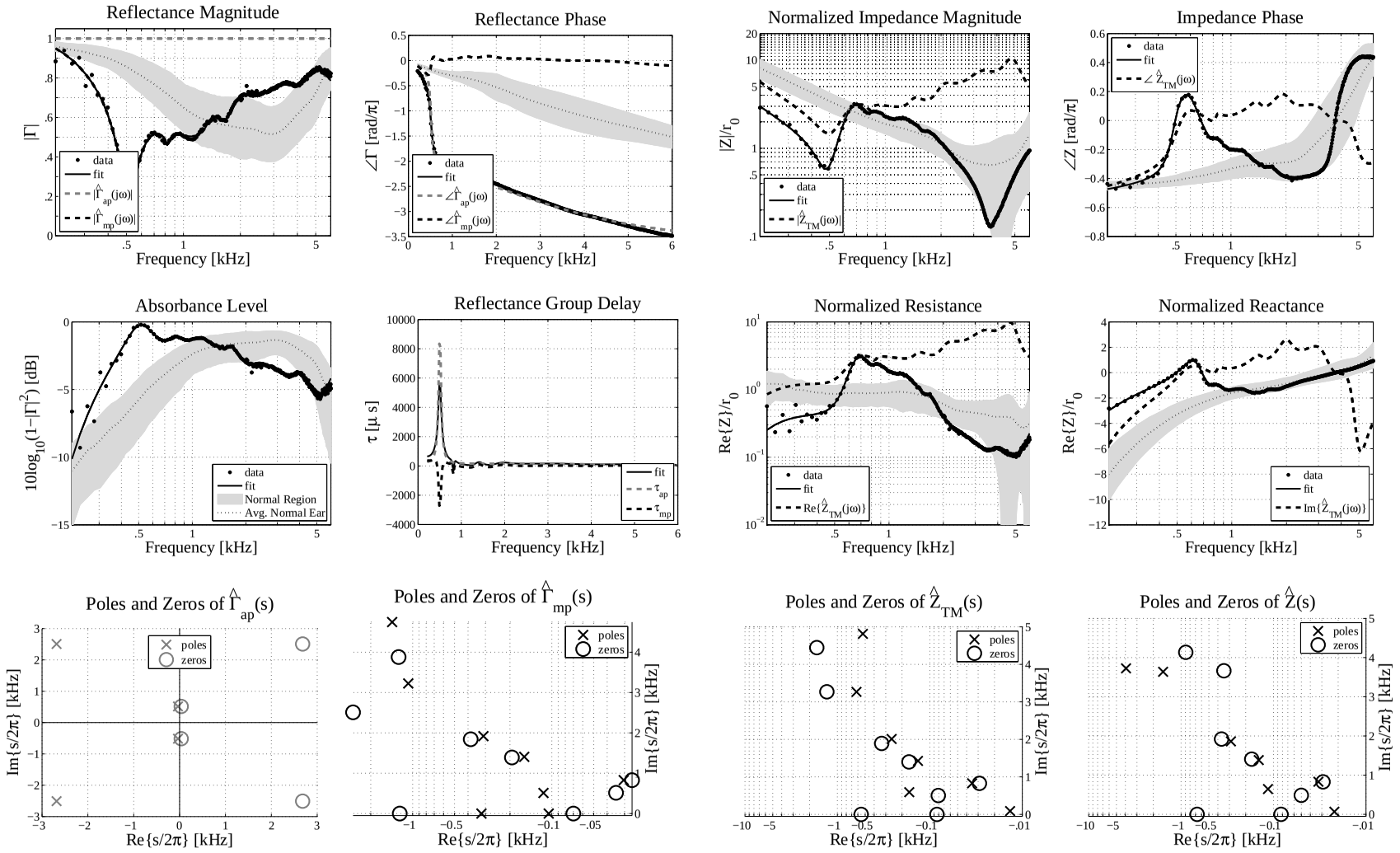

Figure B.15: Acoustic summary and pole-zero fit of an ear with *ossicular discontinuity* (P015L) from Nakajima et al. [2012]. The thin dotted black lines and gray regions show the average normal ear ±1 standard deviation from Rosowski et al. [2012]. Factored fit quantities are described in Section 3.4.

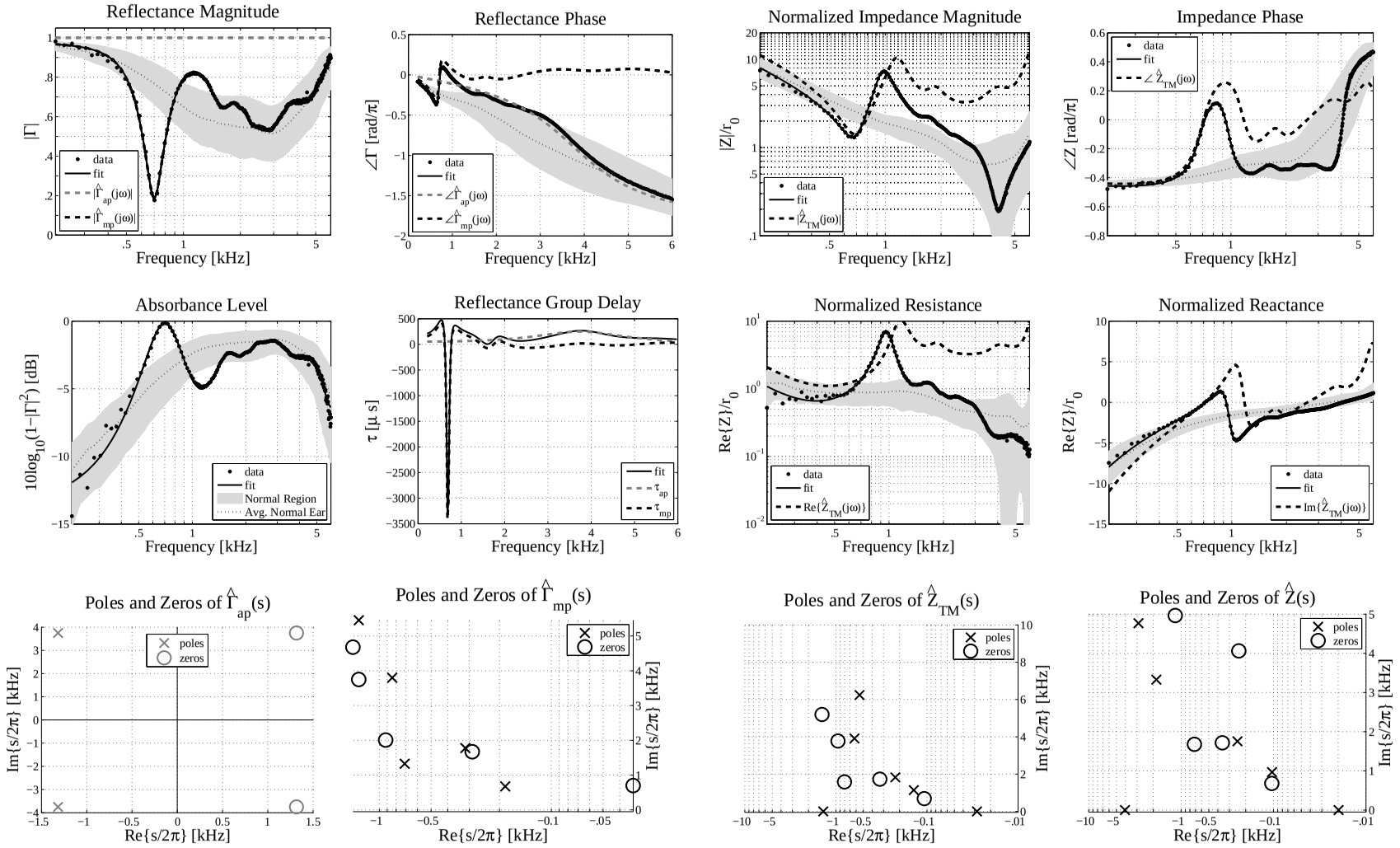

Figure B.16: Acoustic summary and pole-zero fit of an ear with *ossicular discontinuity* (P028L) from Nakajima et al. [2012]. The thin dotted black lines and gray regions show the average normal ear ±1 standard deviation from Rosowski et al. [2012]. Factored fit quantities are described in Section 3.4.

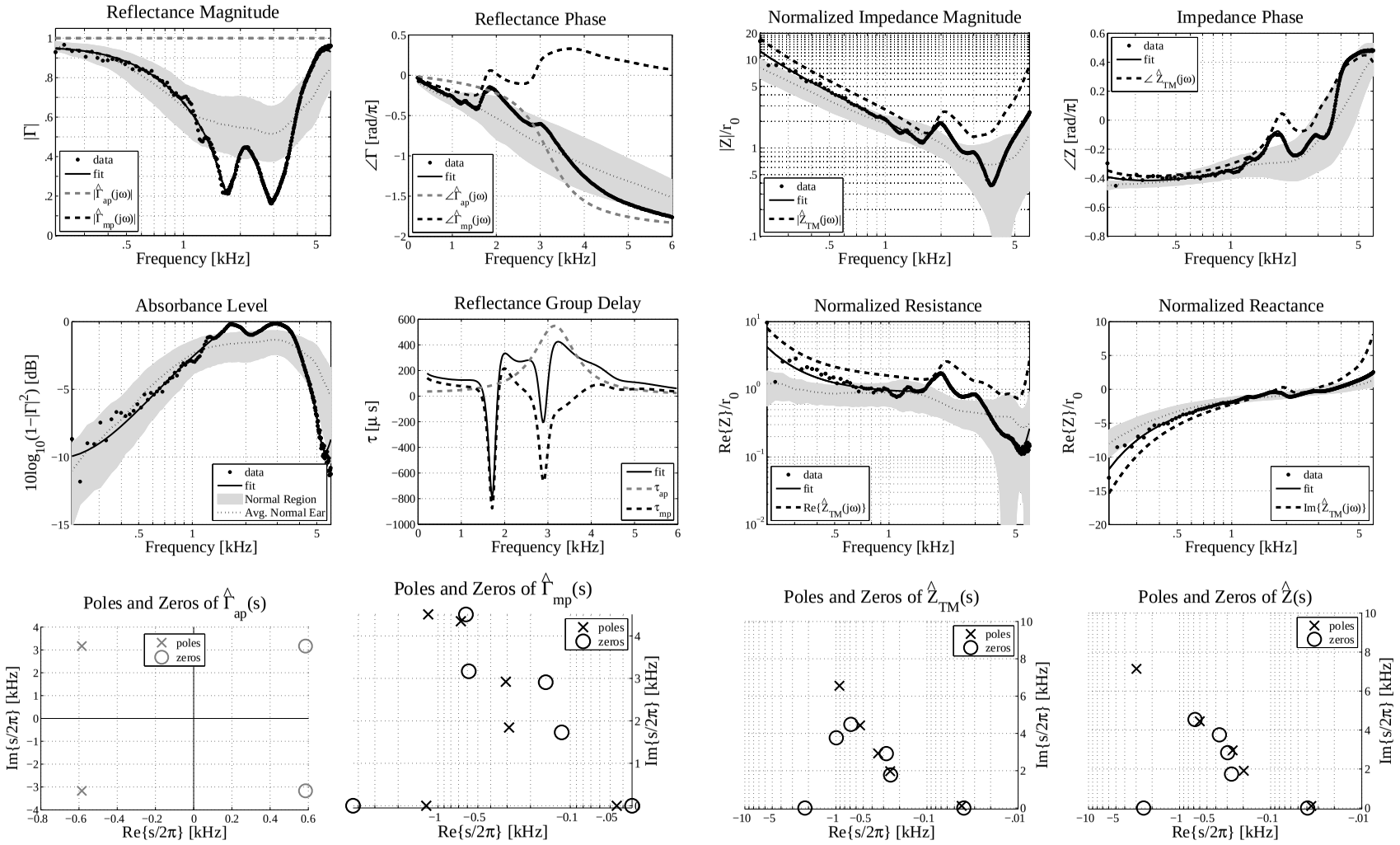

Figure B.17: Acoustic summary and pole-zero fit of an ear with *ossicular discontinuity* (P054R) from Nakajima et al. [2012]. The thin dotted black lines and gray regions show the average normal ear ±1 standard deviation from Rosowski et al. [2012]. Factored fit quantities are described in Section 3.4.

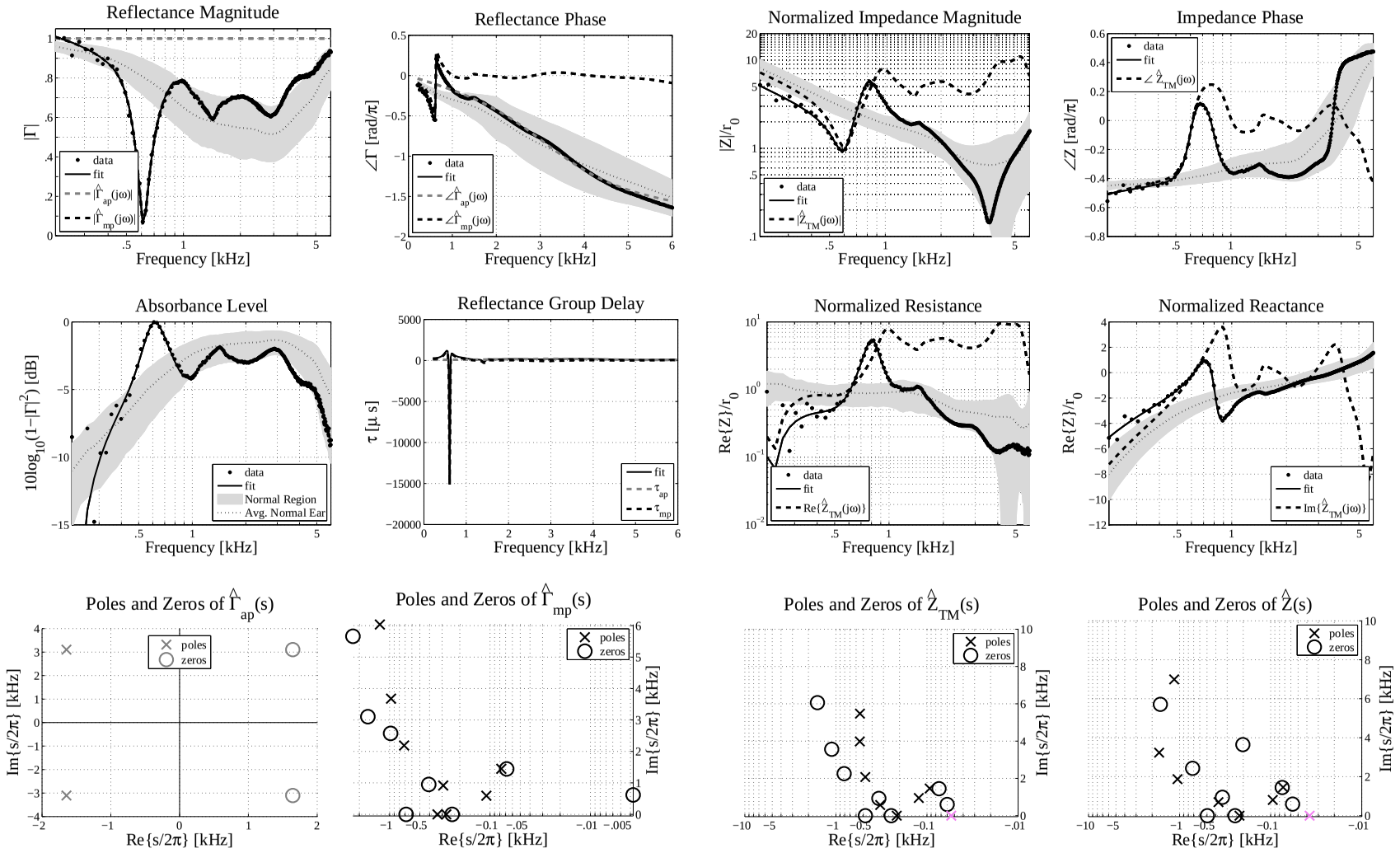

Figure B.18: Acoustic summary and pole-zero fit of an ear with *ossicular discontinuity* (P071L) from Nakajima et al. [2012]. The thin dotted black lines and gray regions show the average normal ear ±1 standard deviation from Rosowski et al. [2012]. Factored fit quantities are described in Section 3.4.

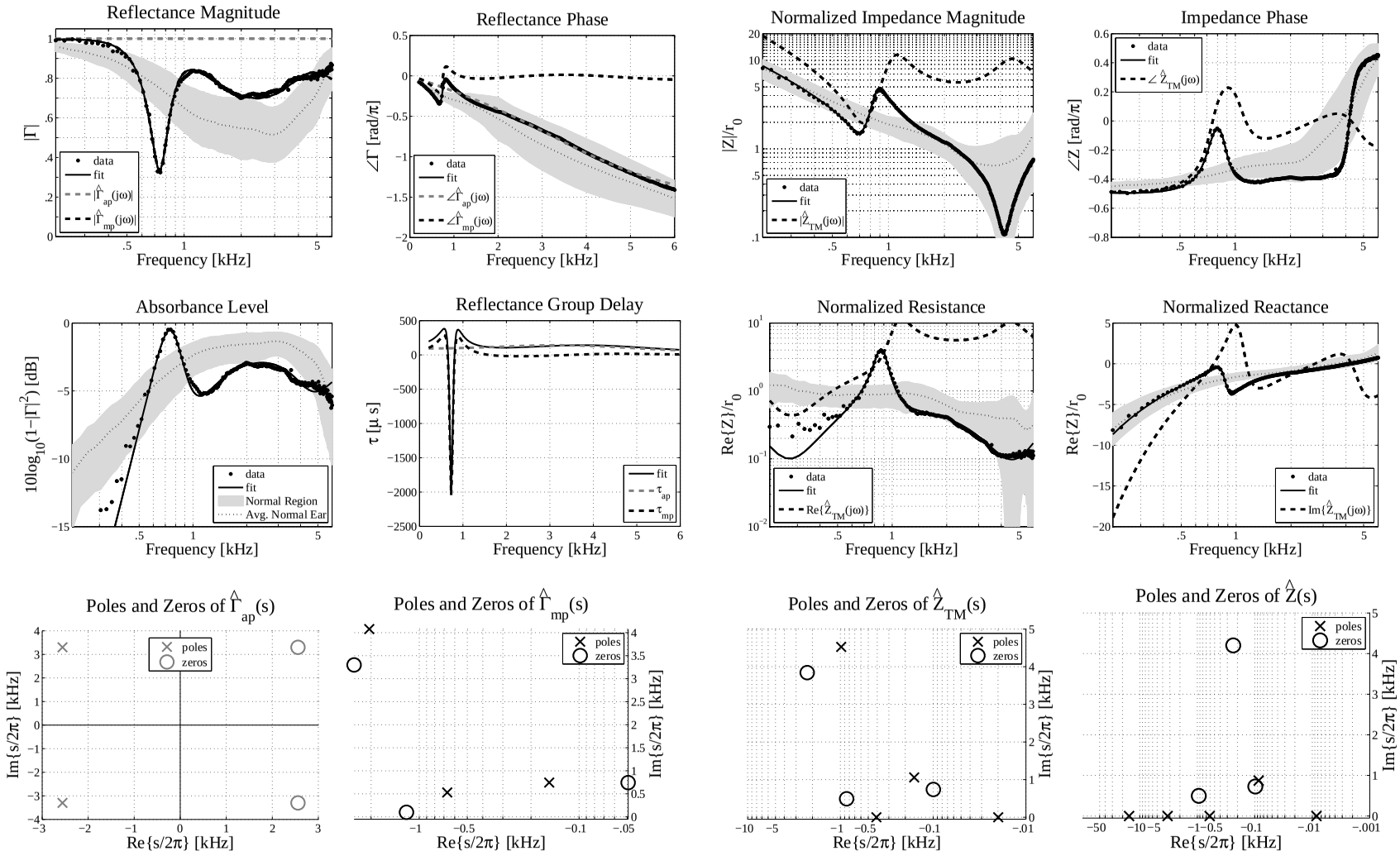

Figure B.19: Acoustic summary and pole-zero fit of an ear with *ossicular discontinuity* (P083L) from Nakajima et al. [2012]. The thin dotted black lines and gray regions show the average normal ear ±1 standard deviation from Rosowski et al. [2012]. Factored fit quantities are described in Section 3.4.

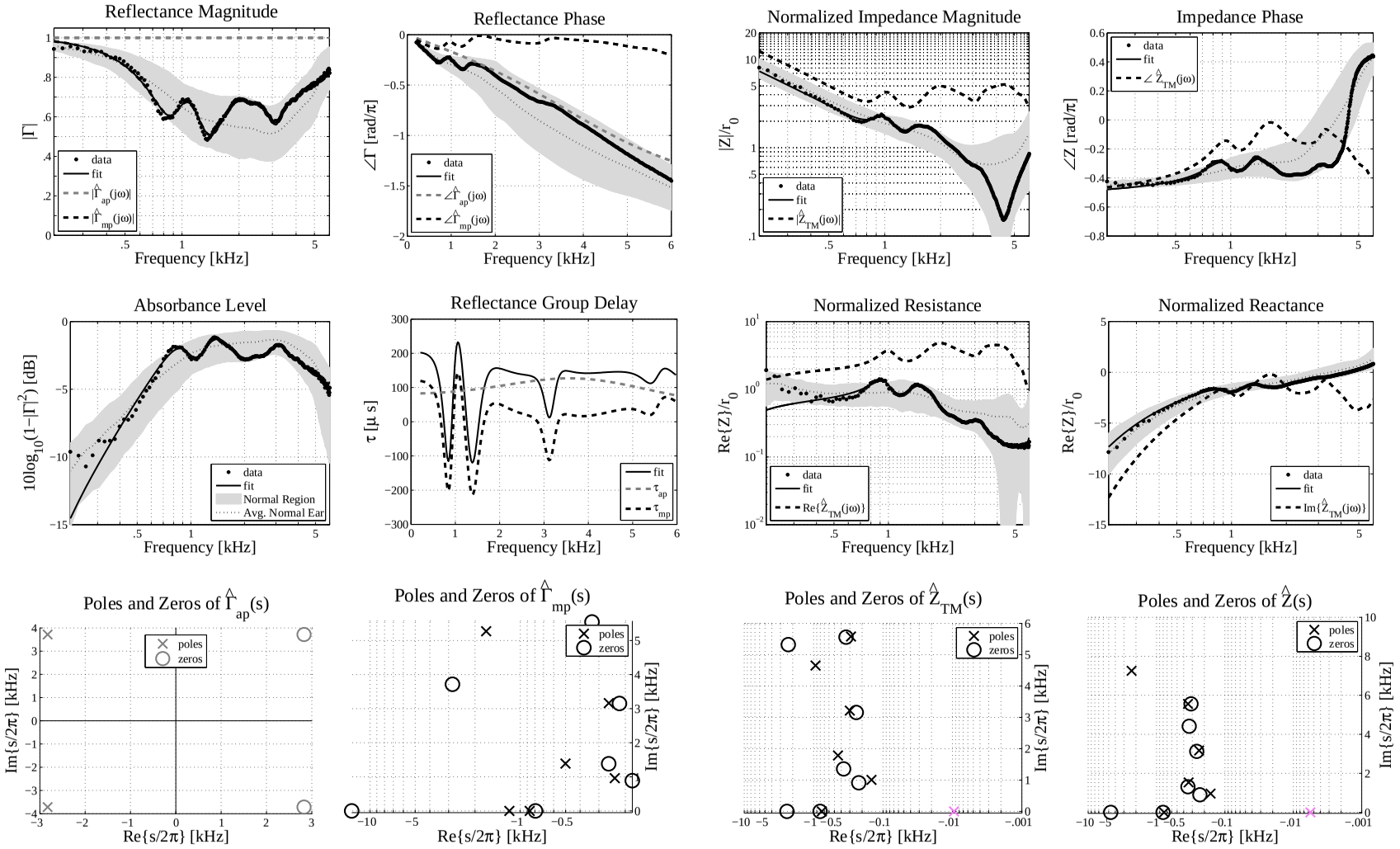

Figure B.20: Acoustic summary and pole-zero fit of an ear with *SSCD* (P018L) from Nakajima et al. [2012]. The thin dotted black lines and gray regions show the average normal ear ±1 standard deviation from Rosowski et al. [2012]. Factored fit quantities are described in Section 3.4.

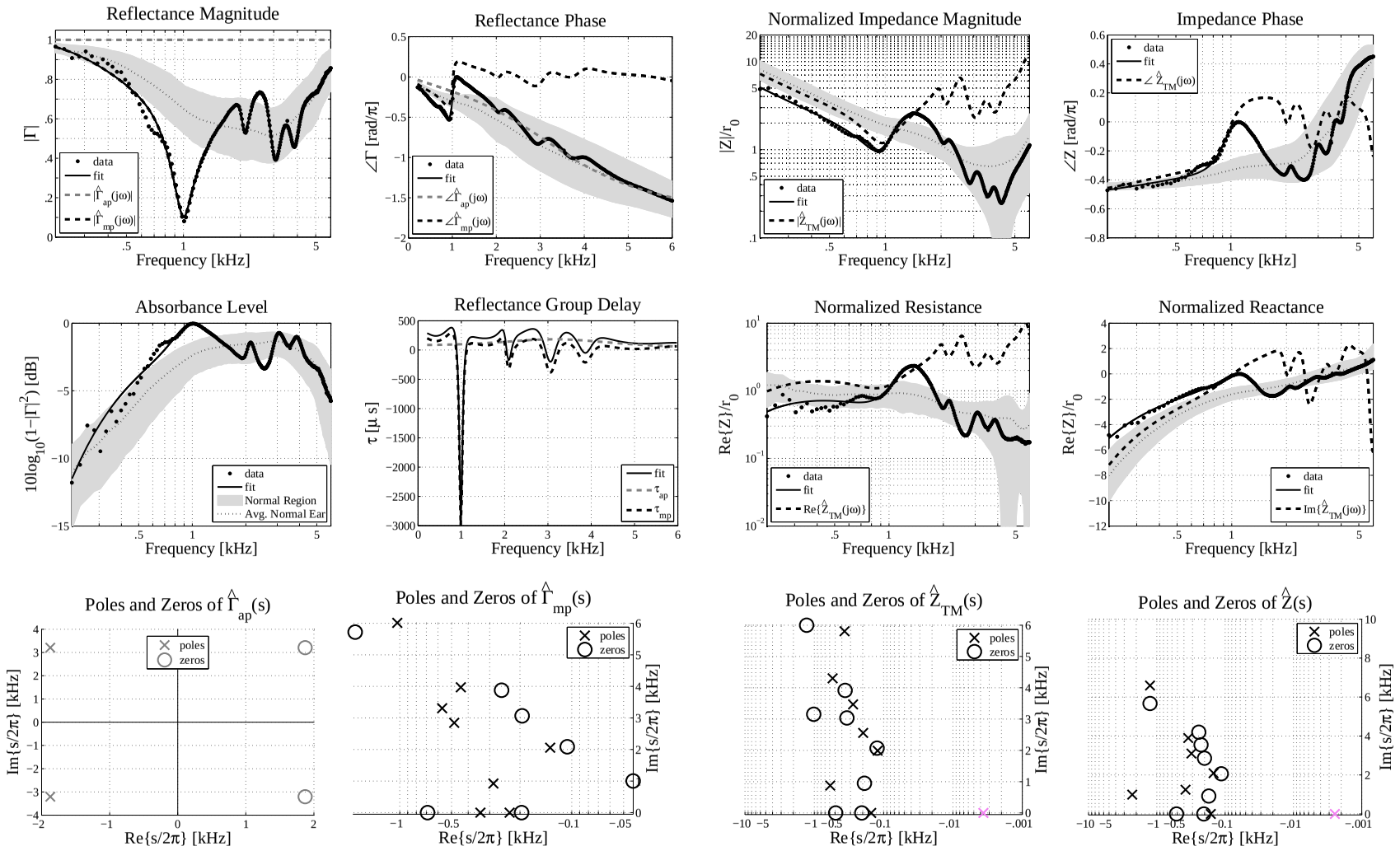

Figure B.21: Acoustic summary and pole-zero fit of an ear with *SSCD* (P044L) from Nakajima et al. [2012]. The thin dotted black lines and gray regions show the average normal ear ±1 standard deviation from Rosowski et al. [2012]. Factored fit quantities are described in Section 3.4.

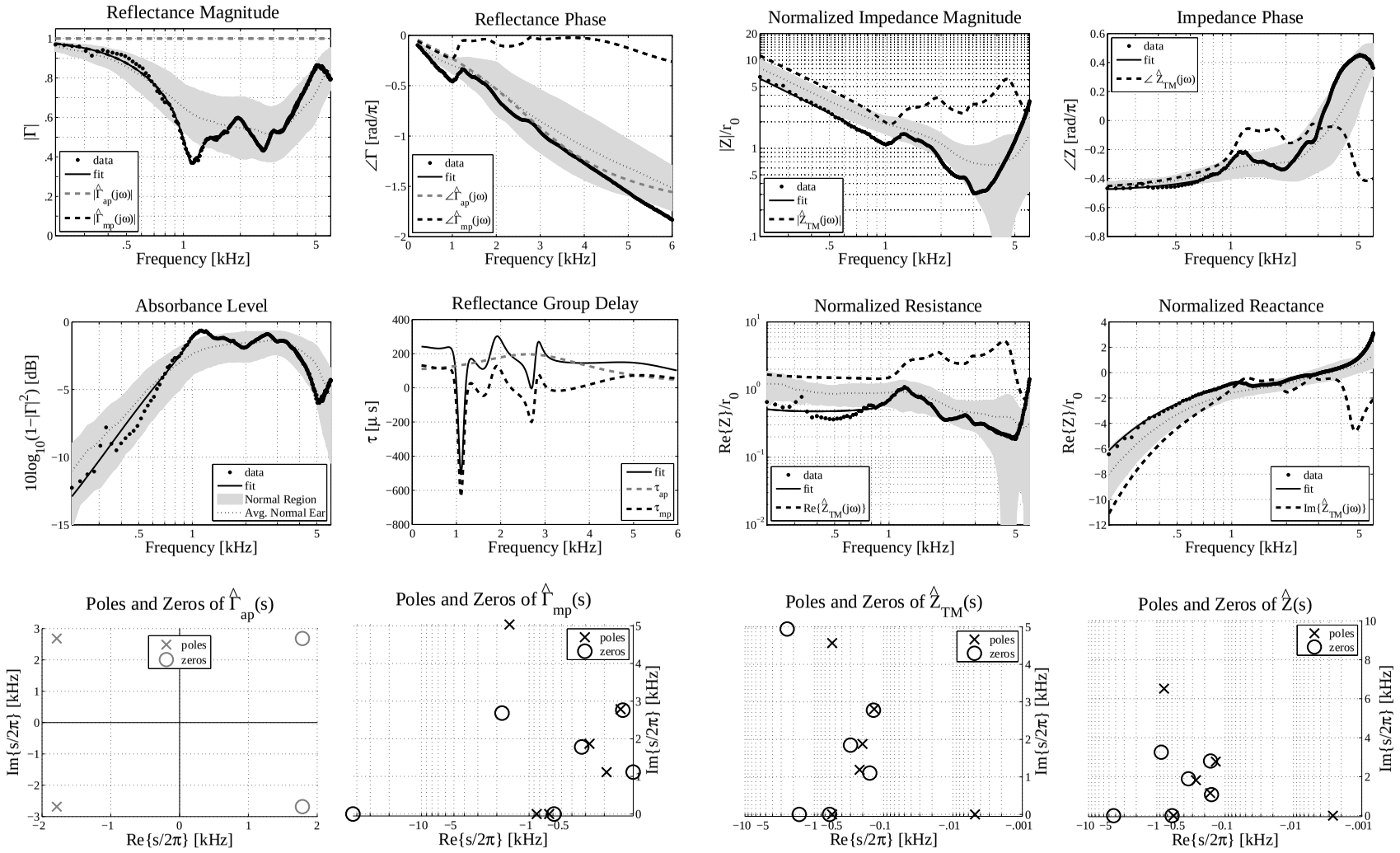

Figure B.22: Acoustic summary and pole-zero fit of an ear with *SSCD* (P052L) from Nakajima et al. [2012]. The thin dotted black lines and gray regions show the average normal ear ±1 standard deviation from Rosowski et al. [2012]. Factored fit quantities are described in Section 3.4.

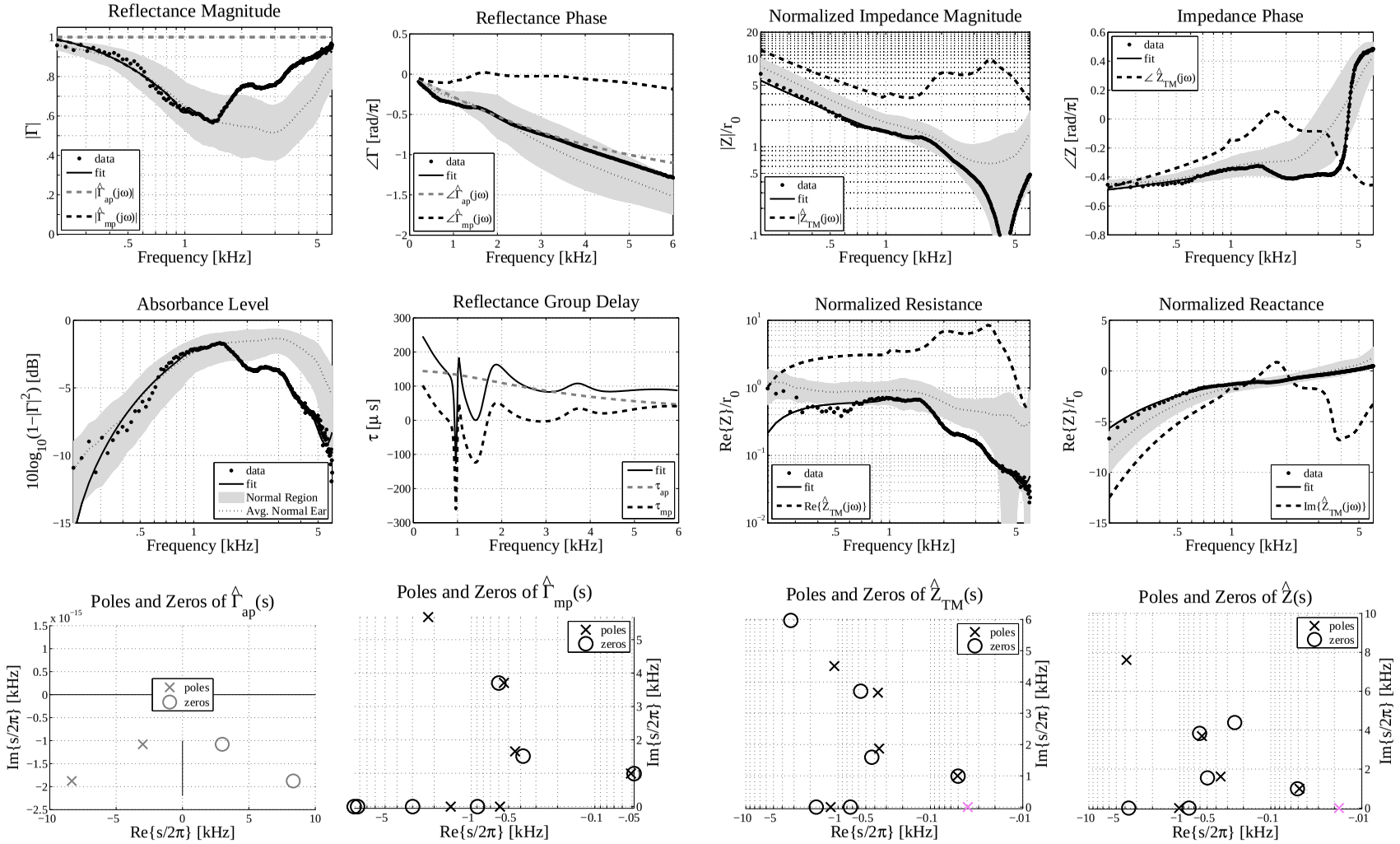

Figure B.23: Acoustic summary and pole-zero fit of an ear with *SSCD* (P059R) from Nakajima et al. [2012]. The thin dotted black lines and gray regions show the average normal ear ±1 standard deviation from Rosowski et al. [2012]. Factored fit quantities are described in Section 3.4.

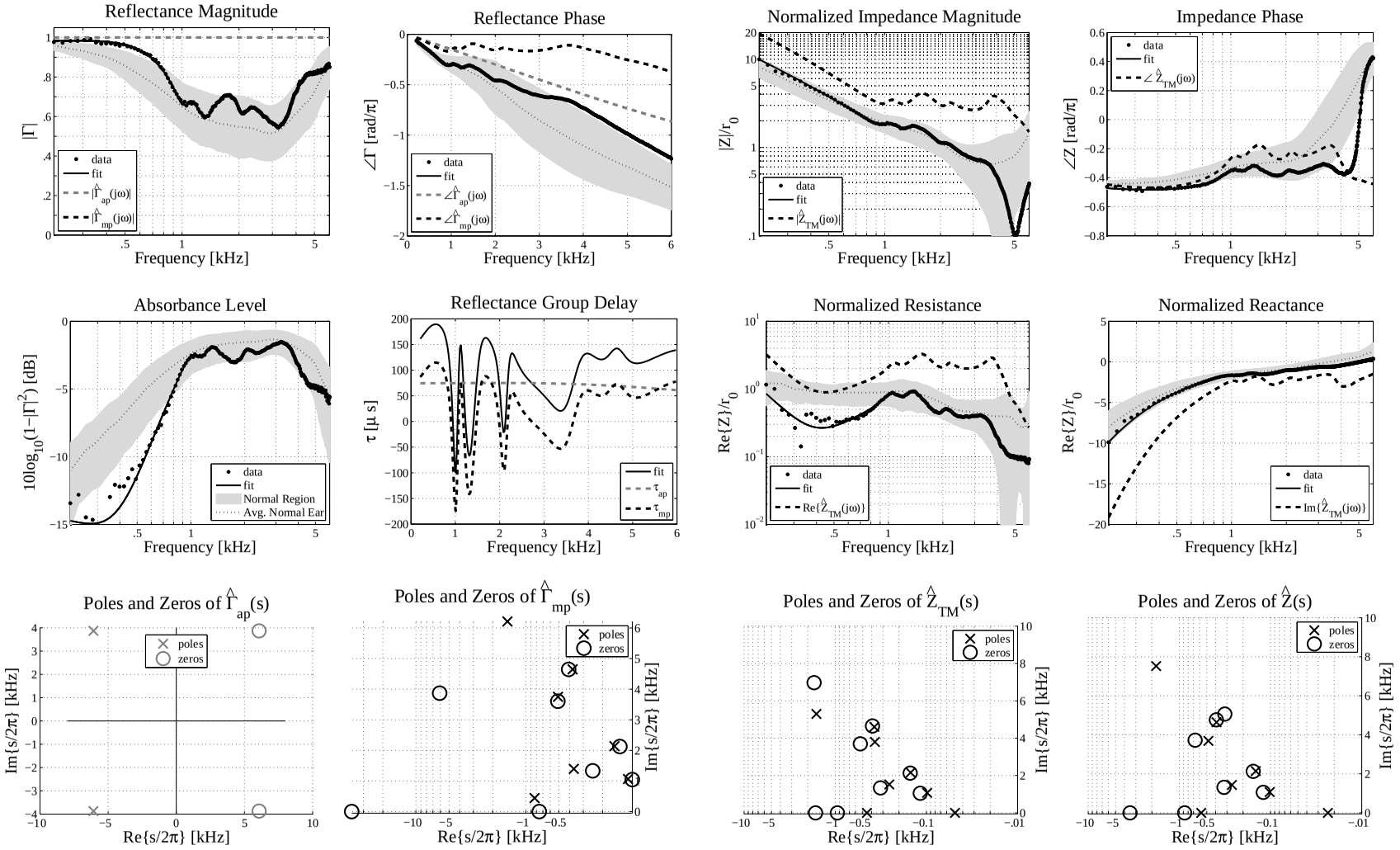

Figure B.24: Acoustic summary and pole-zero fit of an ear with *SSCD* (P074L) from Nakajima et al. [2012]. The thin dotted black lines and gray regions show the average normal ear ±1 standard deviation from Rosowski et al. [2012]. Factored fit quantities are described in Section 3.4.

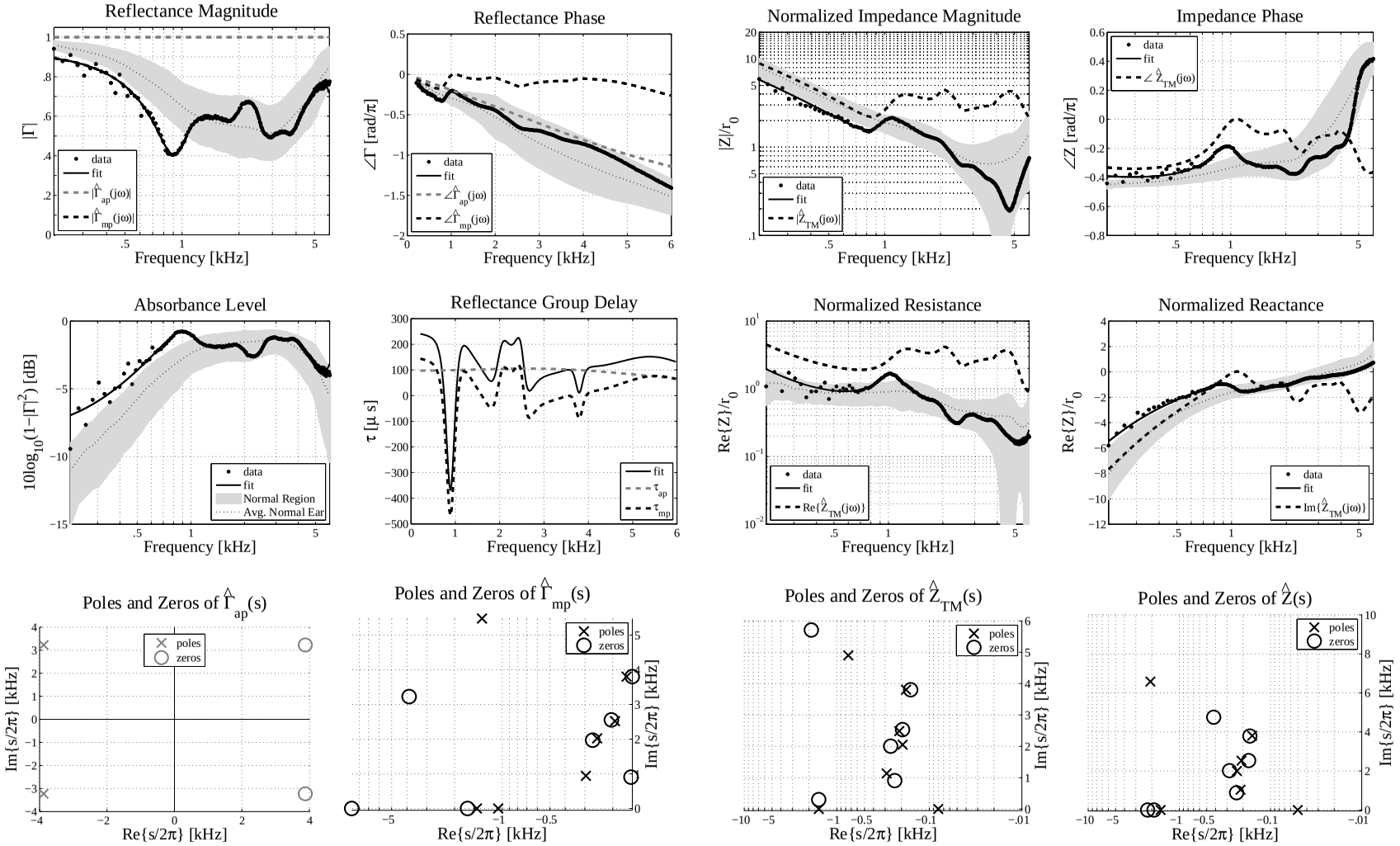

Figure B.25: Acoustic summary and pole-zero fit of an ear with *SSCD* (P082L) from Nakajima et al. [2012]. The thin dotted black lines and gray regions show the average normal ear ±1 standard deviation from Rosowski et al. [2012]. Factored fit quantities are described in Section 3.4.

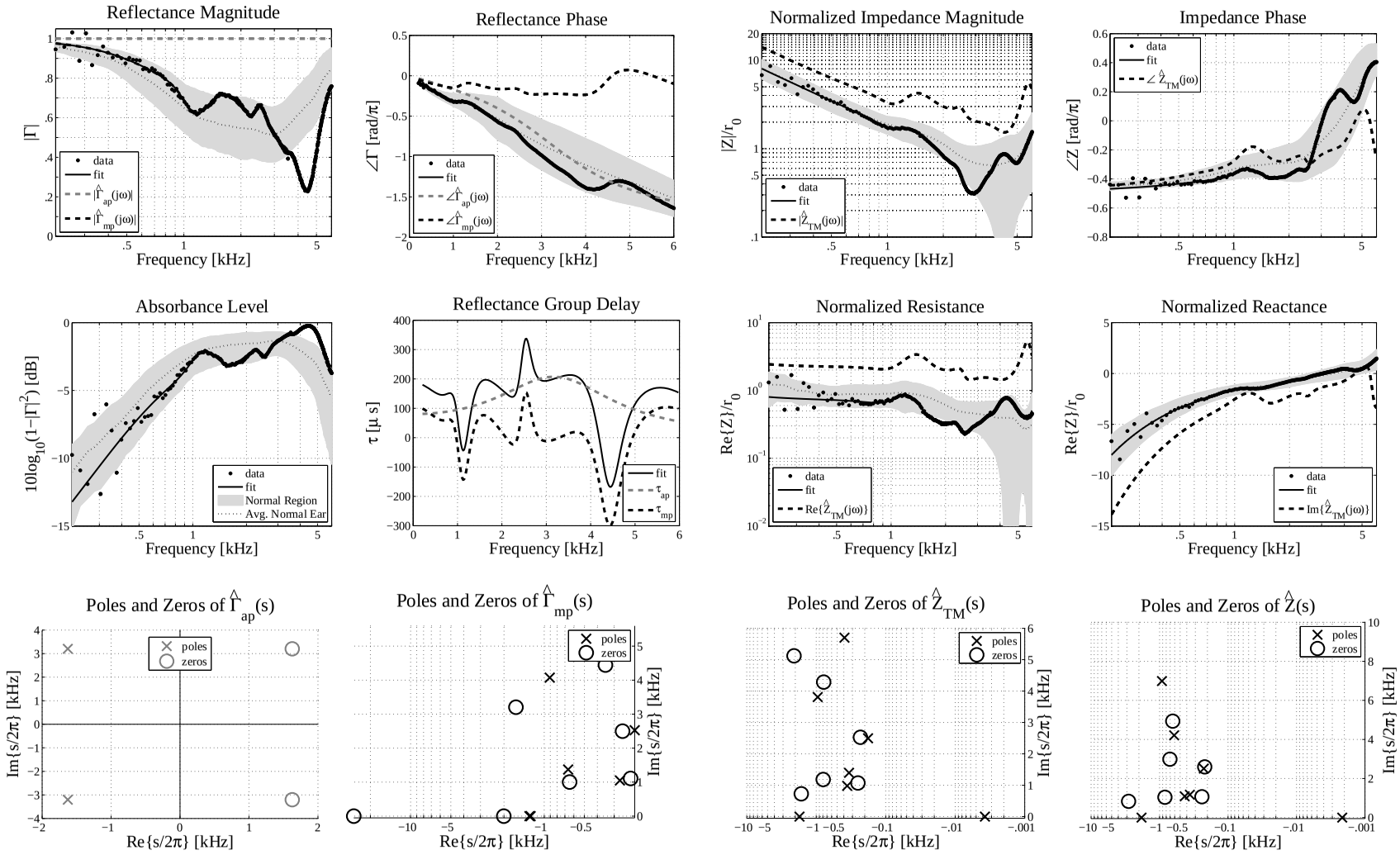

Figure B.26: Acoustic summary and pole-zero fit of an ear with *SSCD* (P087R) from Nakajima et al. [2012]. The thin dotted black lines and gray regions show the average normal ear ±1 standard deviation from Rosowski et al. [2012]. Factored fit quantities are described in Section 3.4.

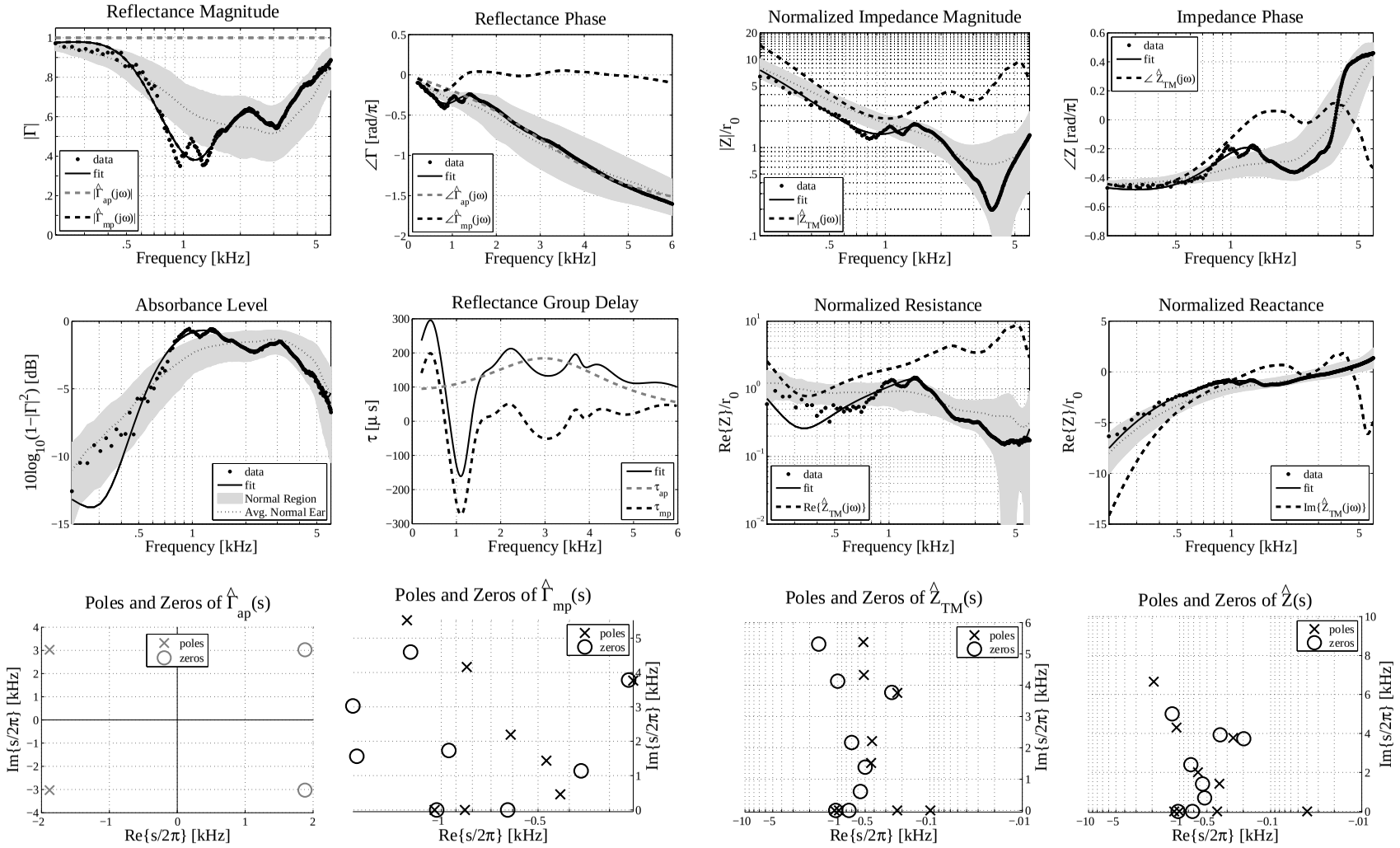

Figure B.27: Acoustic summary and pole-zero fit of an ear with *SSCD* (P103R) from Nakajima et al. [2012]. The thin dotted black lines and gray regions show the average normal ear ±1 standard deviation from Rosowski et al. [2012]. Factored fit quantities are described in Section 3.4.

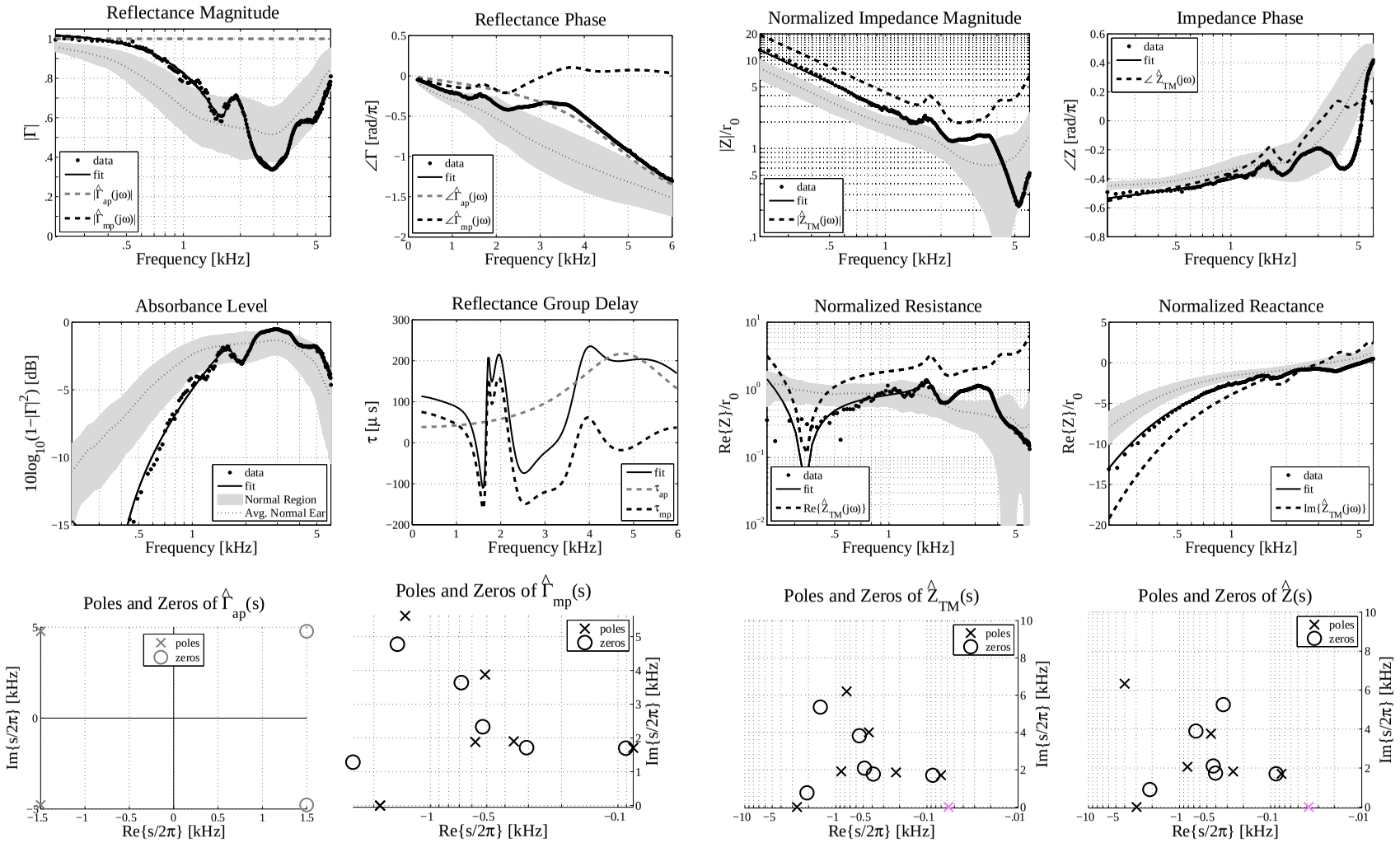

Figure B.28: Acoustic summary and pole-zero fit of an ear with *SSCD* (P104L) from Nakajima et al. [2012]. The thin dotted black lines and gray regions show the average normal ear ±1 standard deviation from Rosowski et al. [2012]. Factored fit quantities are described in Section 3.4.

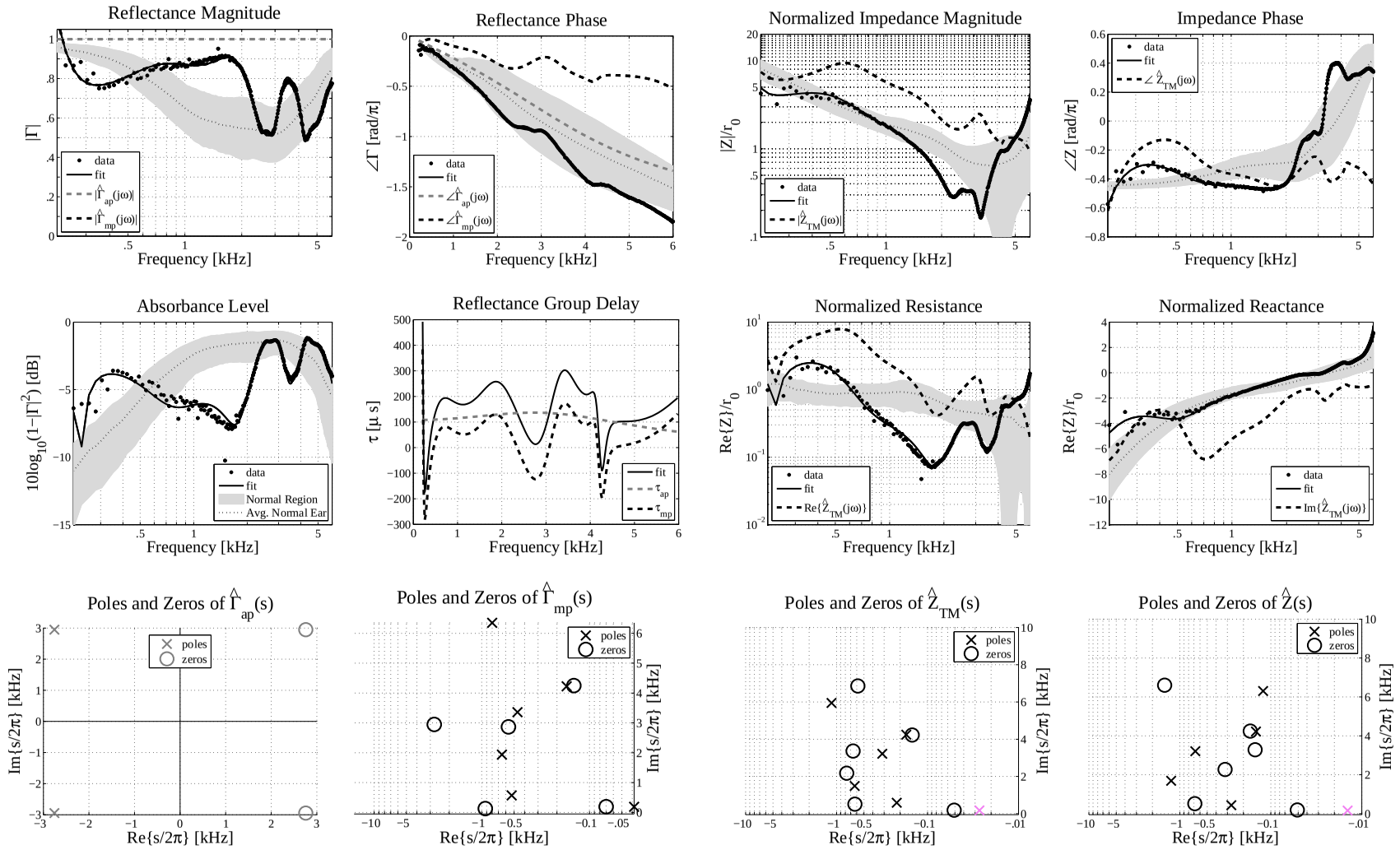

Figure B.29: Acoustic summary and pole-zero fit of an ear with OCT-confirmed *bacterial biofilm* (B1) from Nguyen et al. [2013]. The thin dotted black lines and gray regions show the average normal ear ±1 standard deviation from Rosowski et al. [2012]. Factored fit quantities are described in Section 3.4.

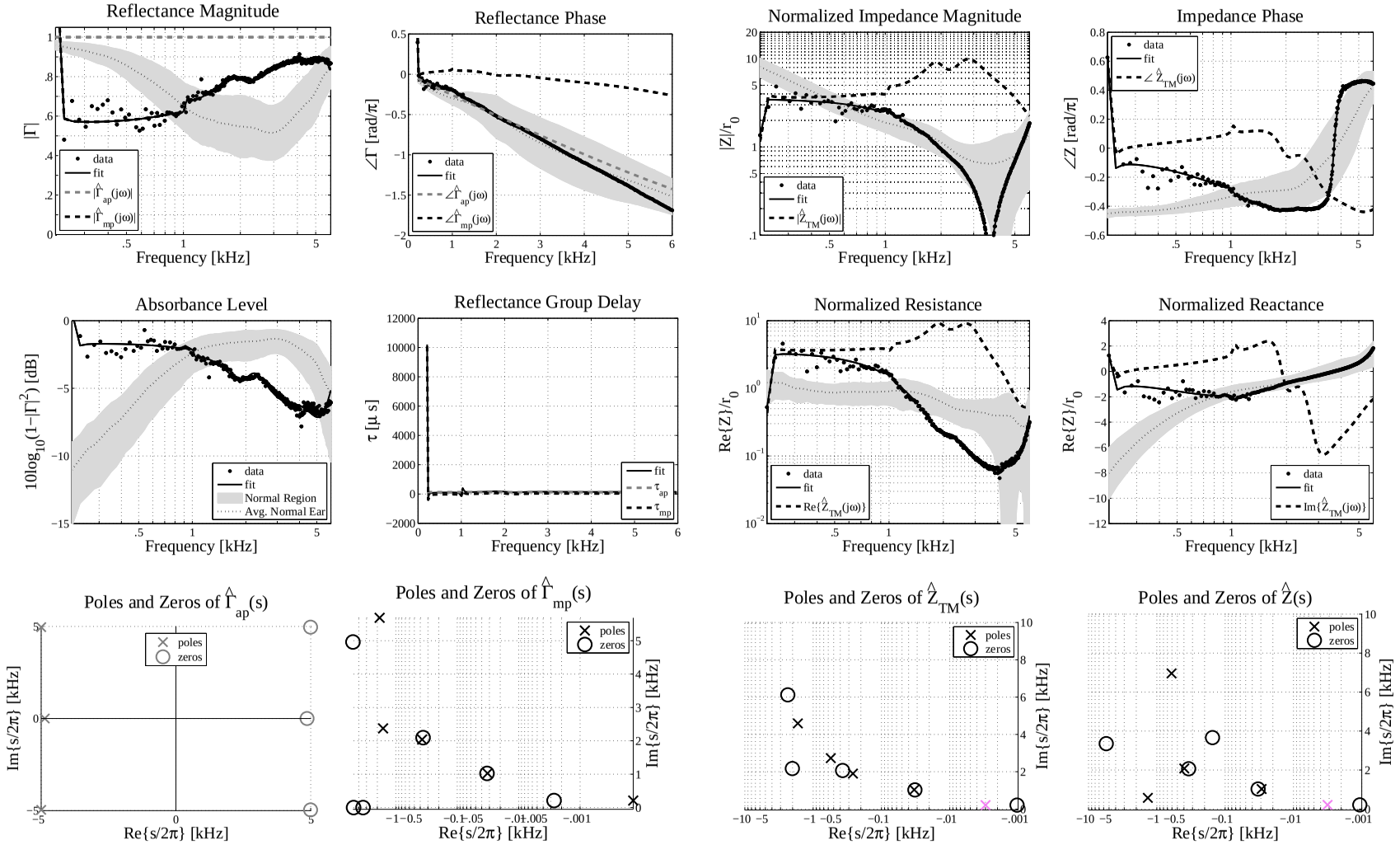

Figure B.30: Acoustic summary and pole-zero fit of an ear with OCT-confirmed *bacterial biofilm* (B2) from Nguyen et al. [2013]. The thin dotted black lines and gray regions show the average normal ear ±1 standard deviation from Rosowski et al. [2012]. Factored fit quantities are described in Section 3.4.

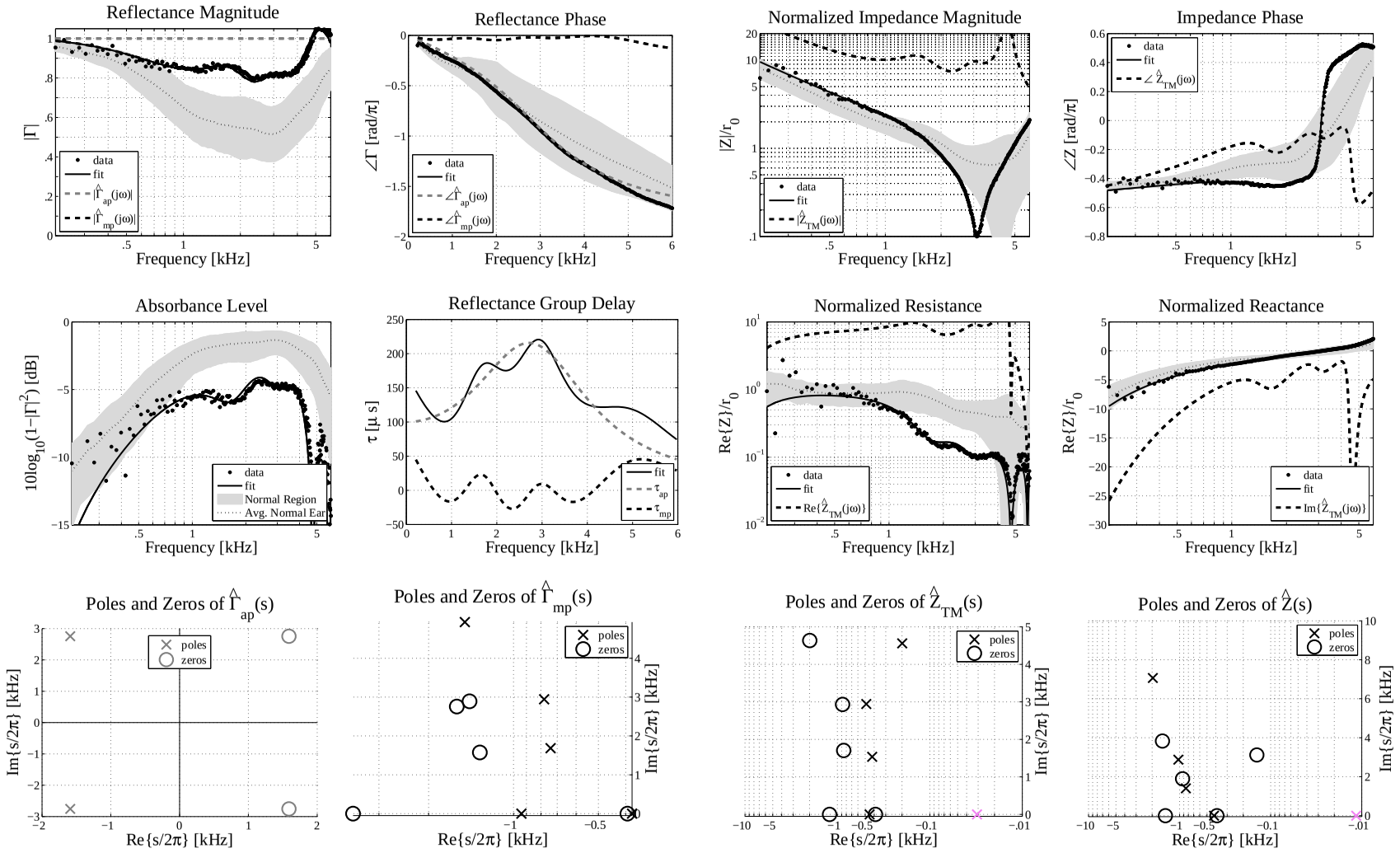

Figure B.31: Acoustic summary and pole-zero fit of an ear with OCT-confirmed *bacterial biofilm* (B3) from Nguyen et al. [2013]. The thin dotted black lines and gray regions show the average normal ear ±1 standard deviation from Rosowski et al. [2012]. Factored fit quantities are described in Section 3.4.

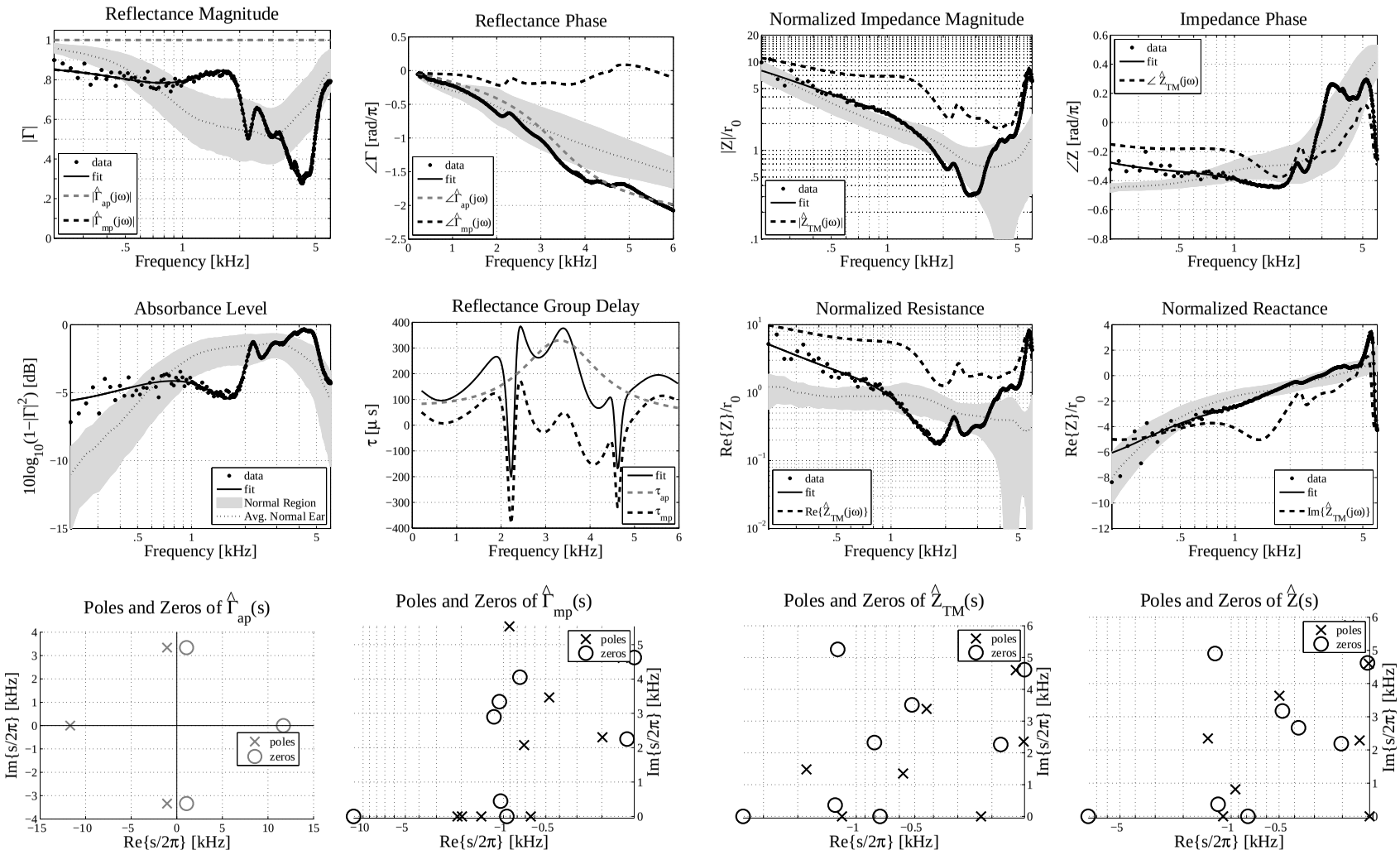

Figure B.32: Acoustic summary and pole-zero fit of an ear with OCT-confirmed *bacterial biofilm* (B4) from Nguyen et al. [2013]. The thin dotted black lines and gray regions show the average normal ear ±1 standard deviation from Rosowski et al. [2012]. Factored fit quantities are described in Section 3.4.

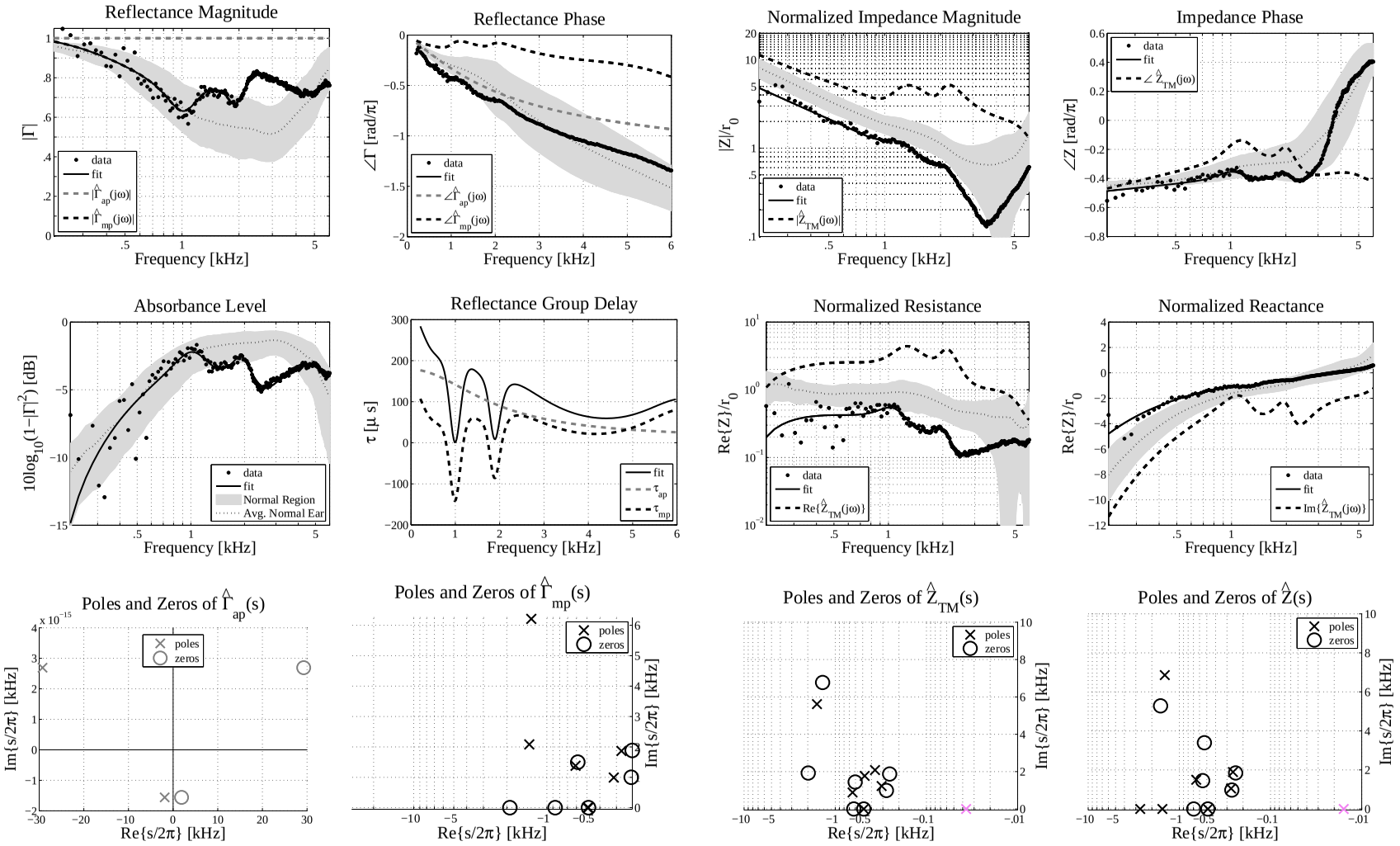

Figure B.33: Acoustic summary and pole-zero fit of an ear with OCT-confirmed *bacterial biofilm* (B5) from Nguyen et al. [2013]. The thin dotted black lines and gray regions show the average normal ear ±1 standard deviation from Rosowski et al. [2012]. Factored fit quantities are described in Section 3.4.

REFERENCES

R. Aibara, J. T. Welsh, S. Puria, and R. L. Goode. Human middle-ear sound transfer function and cochlear input impedance. *Hearing Research*, 152 (1-2):100–109, 2001.

J. B. Allen. Measurement of eardrum acoustic impedance. *Peripheral Auditory Mechanisms*, pages 44–51, 1986.

J. B. Allen, P. S. Jeng, and H. Levitt. Evaluation of human middle ear function via an acoustic power assessment. *Journal of Rehabilitation Research & Development*, 42:63–78, 2005.

M. S. Aparna and S. Yadav. Biofilms: microbes and disease. *Brazilian Journal of Infectious Diseases*, 12(6):526–530, 2008.

A. N. Beers, N. Shahnaz, B. D. Westerberg, and F. K. Kozak. Wideband reflectance in normal caucasian and chinese school-aged children and in children with otitis media with effusion. *Ear and Hearing*, 31(2):221–233, 2010.

C. D. Bluestone and J. O. Klein. *Otitis media in infants and children*. PMPH-USA, 2007.

O. Brune. Synthesis of a finite two-terminal network whose driving-point impedance is a prescribed function of frequency. *J. of Math. Phys.*, 10: 191–236, 1931.

G. A. Campbell. Physical theory of the electric wave filter. *Bell System Technical Journal*, 1(2):1–32, 1922.

J. F. Claerbout. Fundamentals of geophysical data processing. 1985.

J. W. Costerton, P. S. Stewart, and E. P. Greenberg. Bacterial biofilms: a common cause of persistent infections. *Science*, 284(5418):1318–1322, 1999.

J. E. Dohar, P. A. Hebda, R. Veeh, M. Awad, J. W. Costerton, J. Hayes, and G. D. Ehrlich. Mucosal biofilm formation on middle-ear mucosa in a nonhuman primate model of chronic suppurative otitis media. *The Laryngoscope*, 115(8):1469–1472, 2009.

J. C. Ellison, M. Gorga, E. Cohn, D. Fitzpatrick, C. A. Sanford, and D. H. Keefe. Wideband acoustic transfer functions predict middle-ear effusion. *The Laryngoscope*, 122:887–894, 2012.

B. L. Farmer-Fedor and R. D. Rabbitt. Acoustic intensity, impedance and reflection coefficient in the human ear canal. *The Journal of the Acoustical Society of America*, 112:600–620, 2002.

M. P. Feeney, I. L. Grant, and L. P. Marryott. Wideband energy reflectance measurements in adults with middle-ear disorders. *Journal of Speech, Language, and Hearing Research*, 46(4):901–911, 2003.

H. Fletcher. Useful numerical constants of speech and hearing. *Bell System Tech. J*, 1925.

B. Gustavsen and A. Semlyen. Rational approximation of frequency domain responses by vector fitting. *Power Delivery, IEEE Transactions on*, 14(3): 1052–1061, 1999.

H. Hudde. Measurement of the eardrum impedance of human ears. *The Journal of the Acoustical Society of America*, 73:242–247, 1983.

L. L. Hunter, M. P. Feeney, J. A. Lapsley Miller, P. S. Jeng, and S. Bohning. Wideband reflectance in newborns: Normative regions and relationship to hearing-screening results. *Ear and Hearing*, 31(5):599–610, 2010.

W. Jung, J. Kim, M. Jeon, E. J. Chaney, C. N. Stewart, and S. A. Boppart. Handheld optical coherence tomography scanner for primary care diagnostics. *IEEE Transactions on Biomedical Engineering*, 58(3):741–744, 2011.

D. H. Keefe. Acoustical wave propagation in cylindrical ducts: Transmission line parameter approximations for isothermal and nonisothermal boundary conditions. *The Journal of the Acoustical Society of America*, 75(1):58–62, 1984.

D. H. Keefe and J. L. Simmons. Energy transmittance predicts conductive hearing loss in older children and adults. *The Journal of the Acoustical Society of America*, 114:3217–3238, 2003.

D. H. Keefe, R. Ling, and J. C. Bulen. Method to measure acoustic impedance and reflection coefficient. *The Journal of the Acoustical Society of America*, 91:470–485, 1992.

D. H. Keefe, J. C. Bulen, K. H. Arehart, and E. M. Burns. Ear-canal impedance and reflection coefficient in human infants and adults. *The Journal of the Acoustical Society of America*, 94:2617–2638, 1993.

L. E. Kinsler, A. R. Frey, A. B. Coppens, and J. V. Sanders. Fundamentals of acoustics, 2000.

M. Kringlebotn. Network model for the human middle ear. *Scandinavian Audiology*, 17(2):75–85, 1988.

D. J. Lim. Structure and function of the tympanic membrane: a review. *Acta oto-rhino-laryngologica belgica*, 49(2):101–115, 1995.

K. H. Lundberg, H. R. Miller, and R. L. Trumper. Initial conditions, generalized functions, and the laplace transform: Troubles at the origin. *IEEE Control Systems Magazine*, 27(1):22–35, 2007.

E. Macassey and P. Dawes. Biofilms and their role in otorhinolaryngological disease. *Journal of Laryngology and Otology*, 122(12):1273–1278, 2008.

H. H. Nakajima, D. V. Pisano, C. Roosli, M. A. Hamade, G. R. Merchant, L. Mahfoud, C. F. Halpin, J. J. Rosowski, and S. N. Merchant. Comparison of ear-canal reflectance and umbo velocity in patients with conductive hearing loss: A preliminary study. *Ear and Hearing*, 33(1):35–43, 2012.

C. T. Nguyen, H. Tu, E. J. Chaney, C. N. Stewart, and S. A. Boppart. Noninvasive optical interferometry for the assessment of biofilm growth in the middle ear. *Biomedical Optics Express*, 1(4):1104–1116, 2010.

C. T. Nguyen, W. Jung, J. Kim, E. J. Chaney, M. Novak, C. N. Stewart, and S. A. Boppart. Noninvasive in vivo optical detection of biofilm in the human middle ear. *Proceedings of the National Academy of Sciences*, 109 (24):9529–9534, 2012.

C. T. Nguyen, S. R. Robinson, J. Woonggyu, M. A. Novak, Stephen A. Boppart, and Jont B. Allen. Invesigation of bacterial biofilm in the human middle ear using optical coherence tomography and acoustic measurements. *Hearing Research*, 2013. http://dx.doi.org/10.1016/j.heares.2013.04.001.

P. Parent and J. B. Allen. Time-domain "wave" model of the human tympanic membrane. *Hearing Research*, 263(1-2):152–167, 2010.

M. R. Parsek and P. K. Singh. Bacterial biofilms: an emerging link to disease pathogenesis. *Annual Reviews in Microbiology*, 57(1):677–701, 2003.

P. Piskorski, D. H. Keefe, J. L. Simmons, and M. P. Gorga. Prediction of conductive hearing loss based on acoustic ear-canal response using a multivariate clinical decision theory. *The Journal of the Acoustical Society of America*, 105:1749–1764, 1999.

S. Puria and J. B. Allen. Measurements and model of the cat middle ear: evidence of tympanic membrane acoustic delay. *The Journal of the Acoustical Society of America*, 104:3463–3481, 1998.

D. M. Rasetshwane, S. T. Neely, J. B. Allen, and C. A. Shera. Reflectance of acoustic horns and solution of the inverse problem. *The Journal of the Acoustical Society of America*, 131(3):1863–1873, 2012.

A. Recio-Spinoso, Y. Fan, and A. Ruggero. Basilar-membrane responses to broadband noise modeled using linear filters with rational transfer functions. *Biomedical Engineering, IEEE Transactions on*, (99):1456–1465, 2011.

S. R. Robinson, C. T. Nguyen, and J. B. Allen. Characterizing the ear canal acoustic impedance and reflectance by pole-zero fitting. *Hearing Research*, 2013. http://dx.doi.org/10.1016/j.heares.2013.03.004.

J. J. Rosowski, R. P. Mehta, and S. N. Merchant. Diagnostic utility of laser-doppler vibrometry in conductive hearing loss with normal tympanic membrane. *Otology & Neurotology*, 24(2):165–175, 2003.

J. J. Rosowski, H. H. Nakajima, and S. N. Merchant. Clinical utility of laser-doppler vibrometer measurements in live normal and pathologic human ears. *Ear and Hearing*, 29(1):3–19, 2008.

J. J. Rosowski, H. H. Nakajima, M. A. Hamade, L. Mahfoud, G. R. Merchant, C. F. Halpin, and S. N. Merchant. Ear-canal reflectance, umbo velocity, and tympanometry in normal-hearing adults. *Ear and Hearing*, 33(1): 19–34, 2012.

R. A. Scheperle, S. T. Neely, J. G. Kopun, and M. P. Gorga. Influence of in situ, sound-level calibration on distortion-product otoacoustic emission variability. *The Journal of the Acoustical Society of America*, 124:288–300, 2008.

R. D. Serwy. The limits of brunes impedance. 2012. MS Thesis, University of Illinois at Urbana-Champaign, Urbana, IL.

N. Shahnaz, K. Bork, L. Polka, N. Longridge, D. Bell, and B. D. Westerberg. Energy reflectance and tympanometry in normal and otosclerotic ears. *Ear and Hearing*, 30(2):219–233, 2009.

D. H. Staelin, A. W. Morgenthaler, and J. A. Kong. *Electromagnetic waves*. Prentice-Hall, Inc., Upper Saddle River, NJ, 1998.

M. R. Stinson, E. A. G. Shaw, and B. W. Lawton. Estimation of acoustical energy reflectance at the eardrum from measurements of pressure distribution in the human ear canal. *The Journal of the Acoustical Society of America*, 72:766, 1982.

M. E. Van Valkenburg. *Modern Network Synthesis*. John Weily & Sons, Inc., New York, NY, 1964.

S. E. Voss and J. B. Allen. Measurement of acoustic impedance and reflectance in the human ear canal. *The Journal of the Acoustical Society of America*, 95:372–384, 1994.

S. E. Voss, J. J. Rosowski, S. N. Merchant, and W. T. Peake. Acoustic responses of the human middle ear. *Hearing Research*, 150(1-2):43–69, 2000.

S. E. Voss, J. J. Rosowski, S. N. Merchant, and W. T. Peake. Middle-ear function with tympanic-membrane perforations. ii. a simple model. *The Journal of the Acoustical Society of America*, 110:1445–1452, 2001.

S. E. Voss, N. J. Horton, R. R. Woodbury, and K. N. Sheffield. Sources of variability in reflectance measurements on normal cadaver ears. *Ear and Hearing*, 29(4):651–665, 2008.

S. E. Voss, G. R. Merchant, and N. J. Horton. Effects of middle-ear disorders on power reflectance measured in cadaveric ear canals. *Ear and Hearing*, 33(2):195–208, 2012.

R. H. Withnell, P. S. Jeng, K. Waldvogel, K. Morgenstein, and J. B. Allen. An in situ calibration for hearing thresholds. *The Journal of the Acoustical Society of America*, 125:1605–1611, 2009.

C. Xi, D. Marks, S. Schlachter, W. Luo, and S. A. Boppart. High-resolution three-dimensional imaging of biofilm development using optical coherence tomography. *Journal of Biomedical Optics*, 11(3):034001, 2006.

J. Zwislocki. Analysis of the middle-ear function. part i: Input impedance. *The journal of the Acoustical Society of America*, 34:1514–1523, 1962.